



**FUNDAMENTAL STUDIES OF STRUCTURE AND
CRYSTALLINITY OF LOW & HIGH MOLECULAR
WEIGHT POLY(3-HEXYLTHIOPHENE) P3HT BY
MEANS OF SYNCHROTRON X-RAY DIFFRACTION**

DISSERTATION

zur Erlangung des Grades eines Doktors
der Naturwissenschaften

vorgelegt von

M.Sc.

Siddharth Joshi

geb. am 02.07.1976 in Lucknow (Indien)

eingereicht beim Fachbereich -7, Physik
der Universität Siegen

Siegen, 2008

Gutachter:

Prof. Dr. Ullrich Pietsch

Tag der mündlichen Prüfung:

8th Dec. 2008

Prüfer:

Prof. Dr. Dieter Neher

Prof. Dr. Thomas Mannel

Dedication

To the loving memory of my Parents

Table of Contents

Abstract	viii
Introduction to the Problem – Scope and Outline of this Thesis	1
• Scope and Out-Line of Thesis	2
• References	4
Chapter 1	5
Polymer: An Introduction	5
1.1. Conjugated Polymer.....	5
1.2. Conjugated Polymers: Electronic Conductors.....	8
1.3. Polymer Field-Effect Transistor	10
1.4. Polythiophenes and Family.....	11
1.4.1. Regioregularity.....	13
1.4.2. Dielectric Treatment.....	14
1.4.3. Annealing Treatment.....	15
1.4.4. Molecular Weight.....	15
1.5. Charge Transport from Organic Materials	17
1.5.1. Charge Carrier Mobility	19
1.5.2. Intrachain Transport	21
1.5.3. Interchain Transport	22
1.6. Phase Behavior and Polymer-Polymer Interface.....	22
1.6.1. Landau-de Gennes Free Energy Functional	23
1.7. References.....	26
Chapter 2	31
X-ray Scattering Techniques	31
2.1. Introduction.....	31
2.2. Index of Refraction	31
2.3. X-ray Interaction with Matter	32
2.4. The Evanescent X-ray Wave	34
2.5. X-ray Reflectivity	36
2.5.1. Basic Principle.....	36
2.5.2. Critical Angle	37
2.5.3. A Quick Estimation of Thickness	38
2.6. X-ray Powder Diffraction	38
2.7. Diffractometer Recording of Powder Samples.....	39
2.8. Debye Scherrer Formula.....	41

2.9.	Grazing Incidence Geometries	44
2.10.	Grazing incidence Out-of-Plane Diffraction (GOD) Scans.....	45
2.11.	Grazing Incidence Diffraction (GID) Scans	47
2.12.	Distorted Wave Born Approximation for Grazing Incidence Scattering	49
2.13.	Background Subtraction and Diffuse Scattering	50
2.14.	Coherence Effects.....	51
2.15.	Synchrotron Radiation Sources – Fundamental Operation	52
2.16.	Advantage of Synchrotron Source.....	56
2.17.	References.....	57
Chapter 3	59
Methods and Experimental Details	59
3.1.	ID 10B Beamline at ESRF.....	59
3.2.	Experimental Set-up for X-ray Scattering Techniques.....	63
3.3.	Sample Preparation.....	65
3.3.1.	Material	65
3.3.2.	Solution Processable – Spin Coating Technique.....	65
3.3.3.	Modification of the Substrate via Dielectric Layers	66
3.3.4.	Optimizing the Gate-Insulator Surface	67
3.4.	References.....	69
Chapter 4	70
Room Temperature based X-ray Structure and Crystallinity studies of LMW Poly (3-hexylthiophene) Fraction	70
4.1.	Sample Preparation.....	70
4.2.	Atomic Force Microscopy (AFM) Studies	71
4.3.	Transmission Electron Microscopy (TEM) Studies	72
4.4.	Determination of Layer Thickness	73
4.5.	X-ray Grazing-Incidence Diffraction Studies.....	75
4.6.	GID and GOD Studies at Room Temperature.....	76
4.6.1.	Image Plate Measurements.....	78
4.6.2.	Grazing Incidence Diffraction (GID).....	79
4.6.3.	Presence of Polymorphism.....	80
4.6.4.	Grazing Incidence Out-of-Plane Diffraction (GOD)	80
4.7.	Structure Model	82
4.8.	Interface Induced Ordering.....	83
4.9.	Discussion.....	84
4.10.	References.....	87

Chapter 5	88
Temperature Dependent Structural and Crystallinity Studies of LMW Poly(3-hexylthiophene) by X-ray Diffraction Methods	88
5.1. Sample Preparation and Measurements Details	89
5.2. Temperature Dependent Reflectivity Measurements	90
5.3. Structure Investigation as a Function of Temperature.....	92
5.4. Influence of Film - Substrate Interaction & Thermal Expansion	93
5.4.1 For Out-of-Plane – (100) Peak / Thermal Expansion	93
5.4.2. For In-Plane – (020) Peak / Thermal Contraction.....	95
5.5. Mobility Measurements.....	96
5.6. Discussion.....	97
5.7. References.....	101
Chapter 6	102
Room Temperature Based X-ray Structure and Crystallinity Studies of HMW Poly(3-hexylthiophene)	102
6.1. Sample Preparation.....	102
6.2. Atomic Force Microscopy (AFM) Studies	103
6.3. Transmission Electron Microscopy Study.....	104
6.4. Determination of Layer Thickness	105
6.5. Differential Scanning Calorimetry	107
6.6. X-ray Grazing Incidence Diffraction Studies	108
6.6.1. Image Plate Measurements.....	108
6.6.2. Grazing Incidence Out-of-Plane Diffraction.....	110
6.6.3. Grazing Incidence Diffraction (GID).....	112
6.7. Discussion.....	113
6.8. References.....	115
Chapter 7	116
Temperature Dependent Structural and Crystallinity Studies of HMW Poly(3-hexylthiophene) by X-ray Diffraction Methods	116
7.1. Sample Preparation.....	117
7.2. X-ray Grazing Incidence Diffraction Studies	117
7.3. Structure Investigation as a Function of Temperature.....	117
7.3.1. Grazing Incidence Out-of-Plane Diffraction.....	118
A. Annealing Effect.....	118
B. Number of Heating Cycles Vs Structure Equilibrium.....	121
C. Temperature Induced Physical Properties Variation.....	121
7.3.2. Grazing Incidence Diffraction (GID).....	123
7.4. Depth Dependence Morphological Changes and Ordering	124

7.5.	Depth Dependence Lamella Ordering for Thick and Thin Films.....	126
7.6.	Mobility Measurements	127
7.7.	Discussion.....	129
7.8.	References.....	133
Summary and Outlook.....		134
S.1.	Summary.....	134
S.2.	Future Work.....	138
Appendix		140
A.	OFET Preparation.....	140
B.	Experimental Methods.....	141
B.1.	Differential Scanning Calorimetry.....	141
B.2.	Atomic Force Microscopy (AFM)	143
B.3.	Transmission Electron Microscopy	146
C.	References.....	147
Acknowledgement		148
Curriculum Vitae		150
Talks, List of Publications, Conferences		150
Eidesstattliche Erklärung.....		153

Abstract

Conjugated polymers are the one of the most promising candidates for the active layer of low-cost Organic-field-effect transistors (OFETs). The charge carrier mobility of these conjugated polymers is the key material property, limiting the performance of the devices. The structural ordering along the whole thickness of film, especially near to interface region play an important role of controlling such electrical properties which ultimately gives high device performance. In the present work using complementary techniques I have studied structural properties of P3HT films as a function of molecular weight and film thickness. Detailed structural studies have been done to understand this polythiophene families internal structural ordering and consequently its correlation with charge carrier mobility. This work focussed on the dependence of the charge transport on morphology of the best known polythiophene group member i.e. regioregular poly(3-hexylthiophene). P3HT films (thin as well as bulk) with different molecular weights provided an ideal system for correlating morphological changes in conjugated polymers to resulting changes in charge transport seeing that the charge carrier mobility in OFETs was found to increase up to four orders-of-magnitude as the molecular weight (M_w) of P3HT is increased from 2500 g/mol to 30,000 g/mol.

Grazing incidence X-ray scattering (GIXS) with combination of its complementary techniques like Atomic Force Microscopy (AFM) and Transmission Electron Microscopy (TEM) were used to measure changes in the crystallinity and crystal orientation associated with varying the annealing conditions, substrate surface treatment at a constant M_w .

In particular, X-ray grazing-incidence diffraction (GID) used for depth-resolved structural analysis. We have noticed the several diffraction peaks which are associated with crystalline ordering within the films for low as well as HMW fractions (LMW, HMW) of P3HT besides the amorphous scattering from disordered part of the polymer sample. Both molecular weight fractions display a well pronounced periodicity normal to the surface due to stacking of main chains. The inter-planar distances for such stacked sheets were found to be 1.5 and 1.6 nm for low and high molecular weight fractions, respectively. In the case of a high molecular weight fraction of P3HT surface and bulk molecular ordering is nearly the same. These films are formally amorphous having the crystalline domains dispersed in amorphous matrix. Here, a textured and strong orientation effects are observed. On the other hand, for the low molecular weight fraction, the X-ray diffraction data are different at the surface and for

the bulk samples, where the CCD images show a randomly orientated powder without any preferential orientation of nanocrystallites.

Our results for LMW P3HT indicate the overall higher crystallinity, better in-plane π - π -stacking, and the concentration of highly oriented crystals, but the mobility is more than a factor of 100 lower than HMW P3HT. These counterintuitive results indicate the charge carrier mobility of conjugated polymers is coupled to several different aspects of the morphology. In the case of the LMW films, the ordered regions are embedded in amorphous matrix which isolates the crystallites from their next neighbours. Whereas in HMW films, the long chains connect the small ordered regions and provide a smooth pathway for charges to move through the film. These results were used to develop a model for relating charge transport and thickness dependent structure variation that can be used as a guide for the characterization of such conjugated polymer structures. The molecular structure and morphology of an organic semiconductor are important key factors which control the properties of the interface between the organic film and the insulator, thus a part of research has also focused on interface engineering. We have modified the interface layer interaction by varying the dielectric layers (HMDS, OTS). Our GIXS results on samples with a chemically modified surface showed highly oriented crystals that were nucleated from the substrate and correlate with variations in charge transport for the first 5-10 layers. Correlation between the structural, thermal properties with the OFET performance gives strong evidence that the transport properties of layers prepared from both fractions of poly(3-hexylthiophene) is largely determined by the crystallinity of the samples and in part, responsible for the strong dependence of the OFET mobilities for polymer OFETs on the preparation conditions.

Regarding the comparison of electronic and structural properties for HMW fraction, we have found that the mobility remains constant over a wide range of film thicknesses. Based on our thin and bulk films structural and electrical properties results we presume the existence of an interface-near ultrathin crystalline layer, stabilized by the strong interaction between the polymer chains and the gate insulator, with the main chains oriented almost exclusively parallel to the substrate. A clear interface region found for thick HMW P3HT films and it is responsible for charge transport in the OFET measurements. The existence of amorphous regions in between highly-crystalline lamellae (or nanofibrils) for both short and long chain P3HT samples, controls the charge carrier mobility of such semi-crystalline system.

Therefore control of this amorphous region could hold the answer for high charge carrier mobility of any semicrystalline π conjugated polymers.

Abstrakt

Konjugierte Polymere gehören zu den vielversprechendsten Kandidaten für die aktive Schicht von preiswerten organischen Feld-Effekt Transistoren (OFETs). Für die Leistungsfähigkeit dieser OFETs ist die Ladungsmobilität der konjugierten Polymere die wichtigste Eigenschaft. In dieser Arbeit befindet sich eine rigorose fundamentale Strukturanalyse von regioregularen poly(3-hexylthiophene) (P3HT) und seine Korrelation mit dem Ladungstransport, sowie die Kontrolle dieser Strukturen basierend auf Schichtdicken mit erhöhtem molekularem Gewicht. Sowohl die Grenzschichten zwischen dielektrischem Material und organischen Halbleiter als auch zwischen Luft und organischen Halbleiter wurden untersucht. Die Verbesserung der Aktivschichtmorphologie und –komposition werden diskutiert basierend auf Röntgenstreuungsmethoden und AFM- sowie TEM-Techniken.

Aus den Ergebnissen wird ein Grundverständnis für solche Polymere abgeleitet, die die Strukturdisparität als Funktion von molekularem Gewicht und seiner Korrelation mit den Transporteigenschaften erstellt. Dies kann eine Anleitung für die Entwicklung von neuen chemischen Strukturen sein und das Verständnis der Variation dieser Struktureigenschaften fördern. Gleichzeitig ist dies ein Modell, in dem die Verbesserung der Mobilität in diesen konjugierten Polymeren durch eine bessere Strukturordnung erreicht werden kann.

Introduction to the Problem – Scope and Outline of this Thesis

The roadmap of developing microelectronics has a new branch: organic electronics. Organic electronics, which utilizes the electrical properties of organic materials in the active or passive layers, is an emerging technology that has received much attention. In conjunction with today's demands for new materials and devices, many technologies have emerged for developing organic electronics and consolidating applications and markets. An organic thin-film transistor is the essential device in this paradigm in addition to organic photodiodes and organic light emitting diodes.

For low-cost plastic electronics, soluble conjugated polymers are very attractive because they may allow large area electronic applications to be manufactured in high volumes on arbitrary substrates by printing or other low-cost fabrication techniques.

Most solution-processed organic thin film transistors (OTFTs) have used polymeric organic semiconductors such as alkyl-substituted polythiophenes. Polymeric semiconductor OTFTs typically have field-effect mobility $< 0.1 \text{ cm}^2/\text{V-s}$, compared to $> 1 \text{ cm}^2/\text{V-s}$ often reported for vapour-deposited small molecule organic semiconductors [1-5]. In spite of the lower mobility in polymeric organic semiconductors, a high temperature annealing is usually required to regain molecular ordering for electronic transport [6-7]. Additionally, solution precursor routes to oligomers especially Pentacene OTFTs also have been demonstrated with mobility near $0.9 \text{ cm}^2/\text{V-s}$ [8]; however, this approach requires a high temperature conversion step ($\sim 200 \text{ }^\circ\text{C}$), which precludes the use of low-temperature plastic substrates.

Charge transport in conjugated polymers is regarded as a hopping process between localized states, which are thought to consist of individual conjugated segments. Due to different orientations of the conjugated segments with respect to each other and to their different lengths, a distribution of localized energy states will be present in the polymer. In this way the charge carrier transport through the semiconductor bulk material is related to the presence of order and disorder in the system.

The amount of disorder has its own significance. Among various types of polymeric semiconductors, regioregular poly(3-hexylthiophene) P3HT is most explored due to its wide commercial availability and high carrier mobility.[3, 7] The structure of the such material in solid state is governed by Van der Waals and dipole-dipole forces, which give them the properties of semiconductors and insulators. Despite of considerable improvements in device

properties, for the better understanding of these materials and charge transport, there are still some fundamental questions need to be answered - such as

1. Structural dependent nature of charge transport in these devices
2. Interface engineering
3. Temperature induce re-crystallization phenomena and morphological changes
4. Depth dependence crystallites orientation
5. Thermal persuade enhancement of degree of crystallinity
6. Role of amorphous part in semi-crystalline material
7. Study of all these properties as a bulk Vs thin film
8. Correlation of thickness and temperature induced structural improvement with corresponding mobility values.

All these stated properties are crucial to further development of optoelectronic organic devices. Consequently their further understanding can help to improve the charge carrier mobility, which is fundamental key factor of all these organic devices.

Therefore, all these vital key points are systematically scrutinised in this thesis using conventional X-ray diffraction methods and supporting AFM; TEM modern surface science techniques, as well as its correlation with device performance using bottom gate top contact transistor geometry.

• **Scope and Out-Line of Thesis**

The present work focuses on the development and application of a combination of X-ray scattering methods, namely grazing-incidence X-ray diffraction (GID), grazing incidence out-of-plane X-ray diffraction (GOD) and X-ray specular reflectivity able to investigate the structure of such π -conjugated polymeric material.

This thesis outlines a fundamental structural investigation of regioregular poly(3-hexylthiophene) (P3HT) and its correlation with charge transport and controlling such structure based on region of thickness interest with increasing molecular weight. The interfaces between dielectric material and semiconductor as well as between air and semiconductor have been examined. The improvement of the active layer morphology and composition are discussed based on X-ray scattering methods and supporting techniques as AFM, TEM. The results are used to develop a basic understanding for such conjugated polymers structure disparity depending on molecular weight and its correlation with the transport properties. This can ultimately guide for the development of new, improved chemical structures or understanding the variation of structural properties with increasing molecular weight. At the same time it

will give a model for improvement of mobility by development or control of better structural order inside such conjugated polymer system.

Chapter 1 reviews a brief history of conjugated polymers, organic thin film transistor, reviews the progress of organic thin film transistors, and summarizes the previous work on Poly(3-hexylthiophene) organic thin film transistors. It then covers the modification of gate dielectrics with silane coupling agents deposited from solution and charge transport process in OFETs, finally comments on phase transition and interface alignment at the polymer/dielectric level.

Chapter 2 will introduce the scientific background of various X-ray surface techniques and their application for structural analysis of polymer material used in this work followed by a brief overview of synchrotron source.

Chapter 3 describes the experimental details and methods for sample preparation with different interfacial layers.

Chapter 4 describes the detailed X-ray structural and crystallinity studies of low molecular weight poly(3-hexylthiophene) at room temperature.

Chapter 5 describes the detailed temperature dependent X-ray structural and crystallinity studies of low molecular weight poly(3-hexylthiophene) with varying thickness.

Chapter 6 describes the detailed X-ray structural and crystallinity studies of high molecular weight poly(3-hexylthiophene) at room temperature.

Chapter 7 describes the temperature dependent X-ray structural and crystallinity studies of high molecular weight poly(3-hexylthiophene) with varying thickness and presence of dual phase behavior. As we know a major part of the charge carriers is located close to the interface and they have the highest mobility, to relate the transport characteristics to the morphological changes due to step heating and energetic disorder present in the polymer film. Surface treatments by silane coupling agents were used to manipulate the surface energy of the gate dielectric and consequently the film formation.

Further there is summary and outlook. The appendix contains OFET preparation as well as organic field-effect transistor measurements, some of experimental methods in short as Differential Scanning Calorimeter, Atomic Force Microscopy and Transmission Electron Microscopy.

Also lists of publications and participant at the conferences by the author are presented. Finally, the acknowledgments and curriculum vitae from the author are presented in the end of this thesis.

• References

- [1]. C.D. Dimitrakopoulos, D.J. Mascaró, *IBM J. Res. & Dev.*, 45(1), pp.11-27, 2001.
- [2]. A. Salleo, M.L. Chabinyc, M.S. Yang, and R.A. Street, *Appl. Phys. Lett.*, 81, pp.4383-4385, 2002.
- [3]. R.J. Kline, M.D. McGehee, E.N. Kadnikova, J. Liu, and J.M. Frechet, *Advanced Materials*, **15**, pp.1519-1522, 2003.
- [4]. K.E. Paul, W.S. Wong, S.E. Ready, and R.A. Street, *Appl. Phys. Lett.*, 83, pp.2070-2072, 2003.
- [5]. G.H. Gelinch, H.E. Huitema, E.V. Veenedaal, E. Cantatore, L. Schrijnemakers, J.B.d. Putten, et al., *Nature Materials*, 3, pp.106-110, 2004.
- [6]. M. Stolka and M.A. Abkowitz, *Synthetic Metals*, 54(1), p.417, 1993.
- [7]. H. Sirringhaus, N. Tessler, and R.H. Friend, *Science*, 280, p.1741, 1998.
- [8]. A. Afzali, C.D. Dimitrakopoulos, and T.L. Breen, *J. Am. Chem. Soc.*, 124, pp.8812-8813, 2002.

Chapter 1

Polymer: An Introduction

A polymer (poly = many in Greek) is a material that consists of many repeated units, called monomers (mono = one). Natural polymers are for instance DNA, proteins, cellulose etc., but polymeric materials can also be synthetically synthesized. Since the number of possible polymer designs is close to infinite, the chemical and physical properties can more or less be tailor-made for various applications. Most polymers or their monomers are soluble in organic solvents. This means that the material can be handled and processed as a liquid and therefore simple manufacturing techniques such as moulding, casting, spin coating, screen printing etc. can be used to create heterostructure and shapes before or after polymerization.

Among the organic-electronic field, conjugated polymers emerging as most favourable electronic applications based material.

1.1. Conjugated Polymer

The class of polymers that can conduct electricity is called conducting polymers. Conjugated polymers differ from their inorganic counterparts that the charge is more localised and the lattice is not as rigid like inorganic semiconductors. The structure of polymeric material is rather complex. The combination of the various structural elements that make up the morphology of the bulk material depends on chemical composition, thermal and mechanical history, and the “length scale” being considered.

Conjugated materials are the most important class of organic semiconductors [1, 2] and can be categorized into two main groups [A] of conjugated polymers and [B] conjugated oligomers. The charge transfer from such conjugated polymers and oligomers can possible through holes or electrons. In general Polymer contains many identical units bonded together in a long chain, having macromolecular properties, opposite to it; oligomers like Pentacene, Rubrene consist of only a few units. These macromolecules show alternating single and double bonds having SP_2 hybridization. Where the carbon p_z orbitals overlap and the π electrons become delocalized and so called forming the π -conjugated system. Whereas Pentacene, Tetracene, Fullerenes etc are the example of conjugated oligomers based Organic semiconductors (OSCs). Figure 1.1 shows some of the important organic semiconductors.

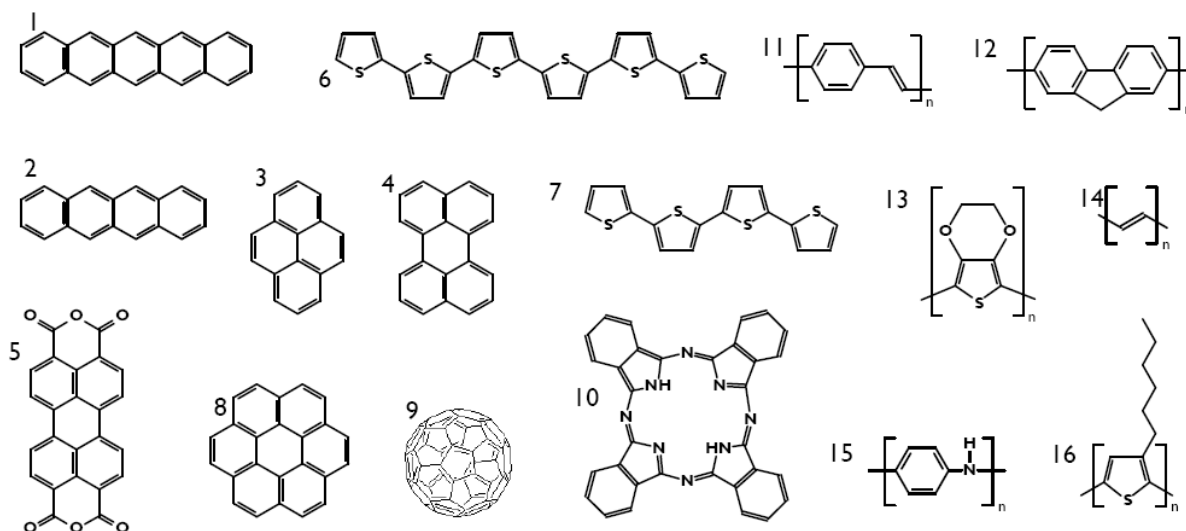


Figure 1.1 Chemical structure of some of the more common organic (semi)conductors: ¹ Pentacene, ² Tetracene, ³ Pyrene, ⁴ Perylene, ⁵ Perylenetetracarboxylic acid (PTCDA), ⁶ a-sexithiophene, ⁷ Quaterthiophene, ⁸ Coronene, ⁹ C60, ¹⁰ Phthalocyanine, ¹¹ Poly-para-phenylenevinylene (PPV), ¹² Polyfluorene, ¹³ PEDOT, ¹⁴ Polyacetylene, ¹⁵ Polyaniline, ¹⁶ Poly(3-hexylthiophene) (P3HT).

Due to the ability of such conjugated polymers to conduct electricity through them, π -conjugated polymers have become the focus of extensive research [3] in many field of application especially on electronic devices, with specialized conductivity properties such as low band gap and intrinsically conducting polymers. Indeed, many successful commercial applications of these polymers have been available for more than ten years, including electrolytic capacitors, magnetic storage media, e-papers, RFID tags. Few of them have shown in Fig. 1.2. Clearly these materials have considerable commercial potential both from the continued development of well established technologies and from the generation of new concepts for their structure analysis. Some of advantages in using organic materials over their inorganic counterparts are

1. Solution processability, which comes by adding the alkyl side chain on it.
2. The primarily used techniques for these polymers are spin coating, drop casting or dip coating; this provides the possibility for large-area electronic applications.
3. At the same time these molecules are flexible and rigid enough for flexible electronic device application.
4. The other advantage is their low cost of production. Now a day's many such products are in market, and due to their low production cost, the electronic devices based on organic semiconductors are getting cheaper.

Concerning the deposition methods, variety of techniques have been employed to deposit organic polymers or Oligomers type semiconducting materials onto the active area of

the device. One approach is by vacuum-deposition method, where by thermal evaporation onto the substrate one can deposit any organic material; primarily this technique is suitable for small oligomer type molecules (Pentacene, Tetracene) rather than long polymers. Pentacene is a prime example of a small-molecule OSC, shows high mobility having poly or mono-crystalline structure depending upon proper deposition conditions [2]. Another approach is solution based processing; here the polymer can deposit onto different substrates from solution processing, utilizing the various available techniques such as printing, spin-coating, drop casting techniques. P3HT is an example of a polymer that is dissolved in a various solvents like chloroform, ethyl-acetate and spin coated from solution used to form microcrystalline lamellar structure of 2D conjugated layers allowing for effective charge transport parallel to the plane and resulting high mobility [4].

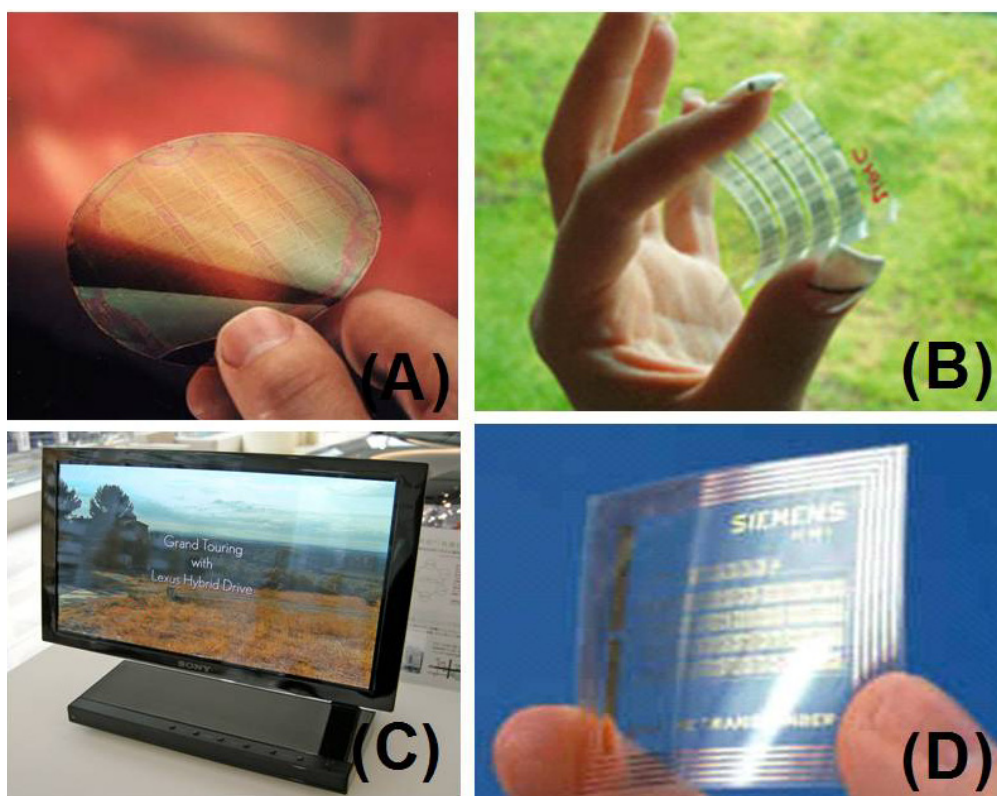


Figure 1.2 Some of the potential applications of organic materials in day-to-day life, (a) Flexible plastic circuit containing 326 OFETs based on polyimide substrate (Philips Research Laboratories, Eindhoven) (b) Plastic electronic circuit, (C) OLED screen from Sony, (D) Electronic news paper from Siemens (Curtsey, Philips Research lab, Eindhoven, Netherland).

Regioregular poly(3-hexylthiophene) (P3HT), utilized in our studies for all the experiments and analysis presented in this thesis has shown in Fig. 1.3. Regioregular means that each 3-hexylthiophene units in the chain is oriented so that the residue group C_6H_{13} is either

head to head or head to tail. This property gives the polymer, upon deposition, better self-organization and order, therefore, increasing substantially the device mobility [4].

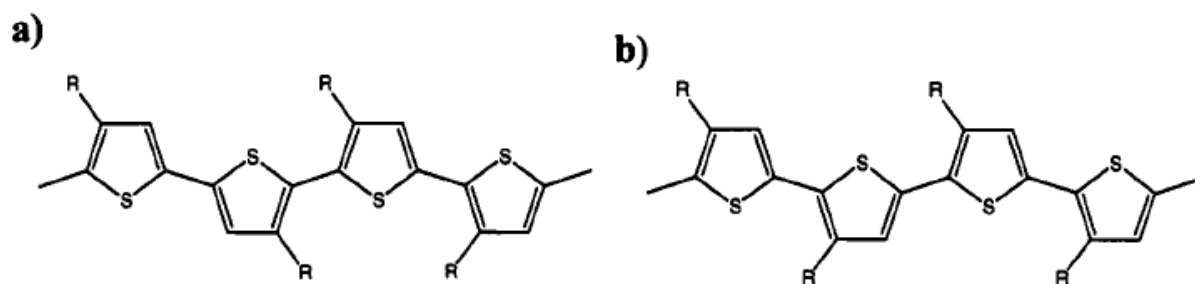


Figure 1.3 Different combinations of P3HTs (a) regiorandom P3HT, (b) Regioregular P3HT.

The charge carrier mobility, μ ($\text{cm}^2/\text{V}\cdot\text{s}$), is the inherent property of such semicrystalline material and is an indicator of how readily charge is transported within the semiconductor polymer upon the applied electric field. For regioregular P3HT, commonly observed mobilities are in the range of $0.1\text{--}1.0 \text{ cm}^2/\text{V}\cdot\text{s}$ for field-effect transistors. This value is 5 orders of magnitude higher than the reported values by other groups [5] for early polythiophene material and is an evidence of the improved structural properties of organic semiconducting materials.

1.2. Conjugated Polymers: Electronic Conductors

Around mid 1970s the first polymer capable of conducting electricity – polyacetylene (PA) - was reportedly prepared by Shirakawa [6]. The subsequent discovery led by Heeger and MacDiarmid [7] shown that the polymer would undergo an increase in conductivity of 12 orders of magnitude by oxidative doping. This discovery opens the door of new world of polymer electronics and followed by an intensive search for other conducting polymers. The target was (and continues to be) a material which could combine the processability, environmental stability, and weight advantages of a fully organic polymer with the useful electrical properties of a metal.

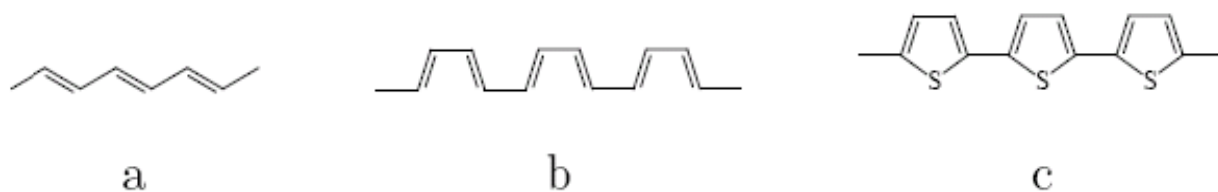


Figure 1.4 Type of conjugated polymer structure: (a) trans- and (b) cis-polyacetylene, and (c) polythiophene.

One of the essential structural characteristic of all conjugated polymers are their quasi in-finite π system extending over a large number of recurring monomer units. This feature results in materials with directional conductivity, strongest along the axis of the chain [8]. The simplest possible form is the archetype polyacetylene $(CH)_x$ shown in Figure 1.4. While polyacetylene itself is too unstable to be of any practical value, its structure constitutes the core of all conjugated polymers. Owing to its structural and electronic simplicity, it is well suited to ab initio and semi-empirical calculations and therefore it has played a critical role in the elucidation of the theoretical aspects of conducting polymers. It is also believed that they possess a spatially delocalized band-like electronic structure [9]. These bands stem from the splitting of interacting molecular orbitals of the constituent monomer units in a manner reminiscent of the band structure of solid-state semiconductors (Figure 1.5).

The mechanism of conductivity within such polymers is based on the motion of charged defects present within the conjugated framework [3, 10]. The present of charge carriers, either positive p-type or negative n-type, are due to the oxidizing or reducing the polymer and are more localized which causes a lattice distortion The subsequent overview given below describes these processes in the framework of p-type carriers.

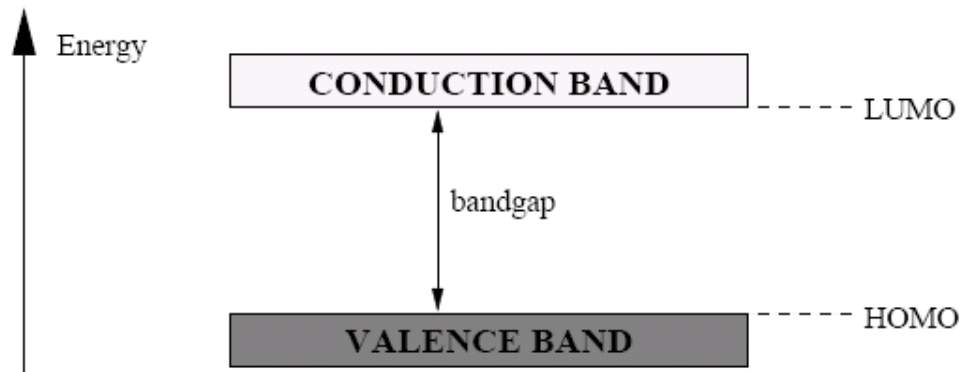


Figure 1.5 Band structure in an electronically conducting polymer.

Oxidation of the polymer initially generates a radical cation with both spin and charge. This coupled electron-phonon entity is referred to as a polaron. A hole polaron comprises both the hole and the free radical. The cation and radical form a bound species, since the increase in the distance between them would necessitate the creation of additional higher energy quinoid units. Due to the bound nature of these polarons, mostly conjugated polymers have low charge carrier mobility. Theoretically [11, 12] it has shown that two nearby polarons combine to form the lower energy bipolaron. One bipolaron is more stable than two polarons despite the coulombic repulsion of the two ions. As the charge carriers (hole/electron pola-

rons) use up their time trapped on a molecule and occasionally obtain enough thermal energy to hop to a next vacant position provided that there is no significant energy barrier to the process.

1.3. Polymer Field-Effect Transistor

Lilienfield has first proposed the idea of polymer field transistor [27], it further studied by Shockley and Pearson in 1948 [28], its first practical application only starts in 1960 [29]. The most popular FET is the metal-oxide-semiconductor FET (MOSFET), also known as the metal-insulator-semiconductor FET (MISFET), where the gate electrode is electrically insulated from the conducting channel by an insulating oxide layer (Figure 1.6). The basic idea of a field-effect transistor is to modulate the electric current that flows between two ohmic contacts, the source and the drain electrodes, by applying a voltage to a third contact, the gate electrode so that charge carriers can be accumulated or depleted in the semiconductor close to the semiconductor/insulator interface. This device can be considered as a capacitor, where one plate is the conductive channel in the semiconducting layer and the other is the gate electrode.

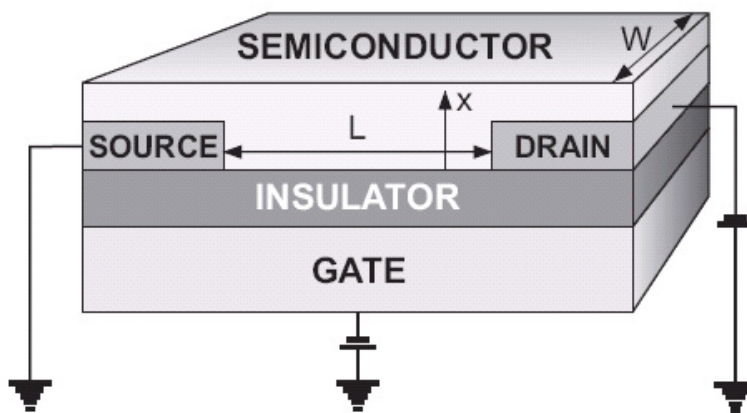


Figure 1.6 Schematic view of a polymer Field-Effect-Transistor (polymer - FET).

The operation of a p-type MISFET can be understood by analyzing the energy band diagram which is schematically shown in Figure 1.7 [30]. In equilibrium the Fermi levels of the gate metal and the semiconductor align due to the charge carriers, which move to or from the semiconductor/insulator interface. When a voltage, called flat-band voltage, V_{fb} , equal to the difference between the Fermi levels of the materials is applied no band bending will be present in the semi-conductor at the semiconductor/insulator interface (Figure 1.7a). The present charges inside the device under biasing conditions are those in the semiconductor and those with equal and opposite sign on the gate. By applying positive or negative gate voltages,

induced charge carriers electrostatically accumulate or deplete in the semi-conductor close to the semiconductor/insulator that gives rise to band bending in the semiconductor.

If a negative bias is applied to the gate (g), the voltage drops across the insulator will accumulate holes at the semiconductor/insulator interface and the energy bands are bent upward (Figure 1.7b). The additional positive charges accumulated in this region are supplied by the drain- and source-ohmic contacts. These charges are mobile and under a small drain bias will give rise to the field-effect current. If a positive voltage is now applied to the gate, the positive charges are depleted from the semiconductor/insulator interface and the energy bands bend downwards. In this case the transistor is biased in the depletion mode (Figure 1.7c). In this way the field-effect current is varied in the source-drain channel.

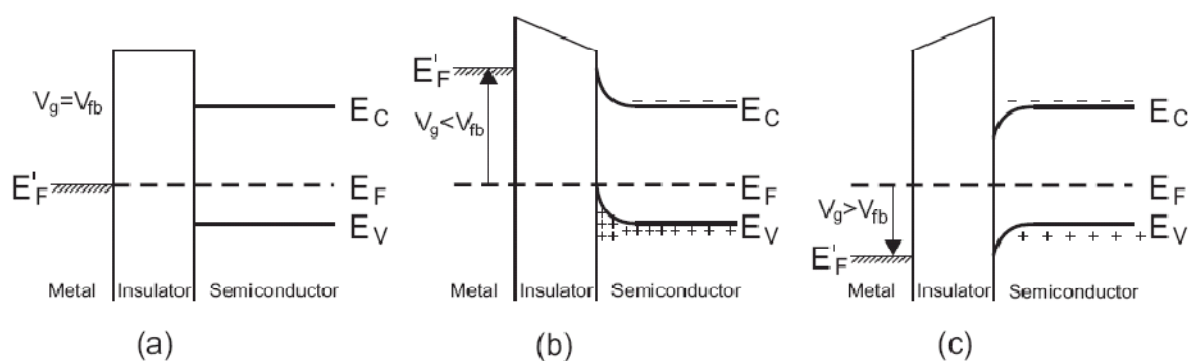


Figure 1.7 Energy-band diagram of a p-type MIS FET working in: a) flat-band ($V_g = V_{fb}$); b) accumulation ($V_g < V_{fb}$); c) depletion ($V_g > V_{fb}$).

1.4. Polythiophenes and Family

Polythiophenes are an important representative class of conjugated polymers having wide variety of molecules for solution processable thin film growth methods, thin films produced by such polythiophene family are environmentally stable that can be used as transistors, sensors, OLEDs, solar cells [31-34] etc. By the chemical modification of its inherent structure, there is always a room to modified or synthesized the new molecules of better molecular properties. It ultimately provides better charge carrier output response. Due to vast possibility of molecular engineering, it led scientists to develop new combination of polythiophene family molecules in search of new materials for enhancing the performance of electronic devices. Pure polythiophene without side chains is neither soluble nor fusible. Once the polymer is prepared, it's not possible to further process the obtained film or powder. However, side chains, which give solubility and fusibility to the polymer, can be attached to the thiophene ring. The most widely used polymer is the poly(3-hexylthiophene) (P3HT).

Since 3-alkylthiophene is not a symmetrical molecule, the band gap and conductivity of poly(3-alkylthiophene)s are strongly dependent on regioregularity of these polymers. As seen in Fig. 1.3, one can see the two kinds of combinations; regioregular and regiorandom. There are three relative orientations available when two thiophene rings are coupled between the 2- and 5- positions. The first of these is head-to-tail (HT) coupling also known as regioregular, the other head-to-head (HH) and tail-to-tail (TT) coupling are known as regiorandom. Regioregular polymer has lower band gap and higher conductivity compared to regiorandom one.

Regioregular Poly(3-hexylthiophene) (six carbons in the alkyl side chain) has proven of material having good solubility in organic solvents and nice film-forming properties. Today, pure and highly regio-regular head-to-tail poly(3-alkylthiophenes) (Figure 1.3b) are commercially available and can be used to create conjugated and well ordered semiconducting thin layers. Some of the thiophene based semiconducting materials chemical structures have shown in Fig. 1.8.

It is found that the length and bulkiness of the side chains strongly influence the charge carrier mobility in poly(3-alkylthiophene)-based transistors [35-37], bulky side chains led to low crystallinity of the solid layers and poor transport properties. For linear alkyl chains, the mobility decreased with increasing chain length. This is attributed to the isolating-nature of the substituent. For linear alkyl chains, the mobility decreased with increasing chain length. This was attributed to the isolating nature of the substituent.

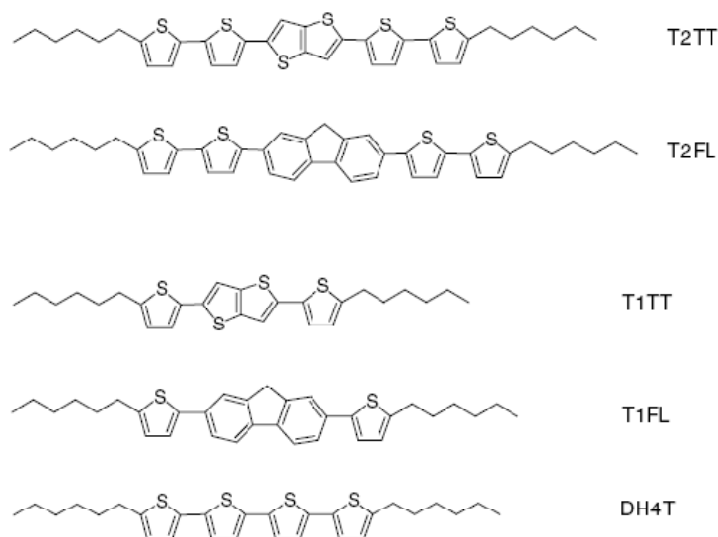


Figure 1.8 Chemical structures of the thiophene-based semiconducting materials.

There are several known parameters which can affect the packing structure in the P3HT thin films, are mainly as

- a). Regioregularity,
- b). Processing methods and conditions
- c). Treatment to the gate-dielectric/gate-insulator,
- d). Solvents used for film deposition,
- e). Annealing,
- f). Molecular weights.

Some of the important parameter concerning about relationship between morphology and the charge transport as per our studies are discussed below

1.4.1. Regioregularity

Differences in regioregularity (regioregular/regiorandom) in P3HT (Fig. 1.3) thin film samples used to produce exclusively different orientations (edge-on, flat-on) relative to the substrate [24]. Therefore the synthesis is very crucial step to produce regioregular P3HT material. A well know method for producing such highly regioregular material is polycondensation method [39-41]. The edge on and flat-on films have shown schematically in Fig. 1.9.

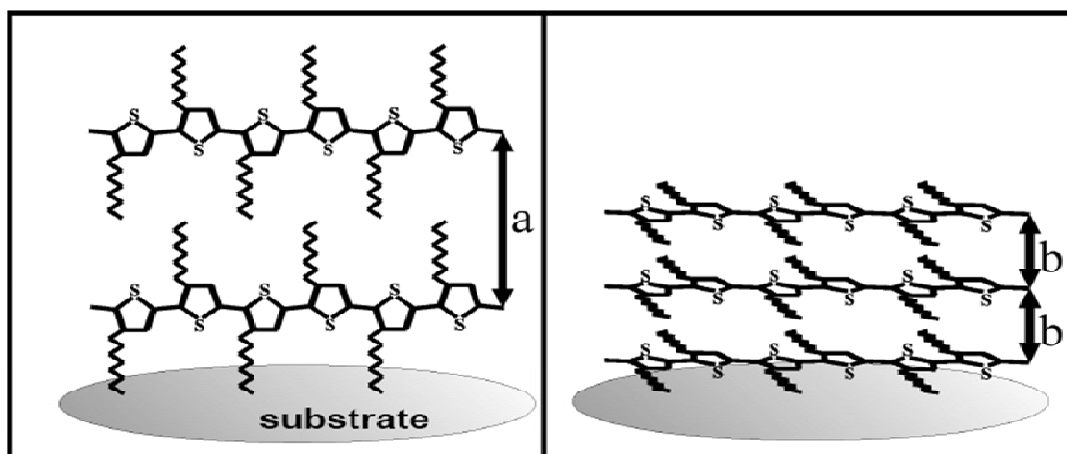


Figure 1.9 Packing orientation of P3HT films relative to substrate with (a) regioregular orientation, where the π - π stacking direction is parallel to substrate, (b) regiorandom orientation, the π - π stacking direction is normal to substrate. The films differ in mobility (parallel to substrate) by a factor >100 , illustrating the effect of morphology on performance [24].

The edge-on orientation gives the higher mobility that differs by two orders of magnitude [24]. Therefore careful substituent selection has been used for tuning the organic semiconductors properties. For our studies we have consider the poly(3-hexylthiophene) having the regioregularity > 99%.

The edge on orientation generally shows the P3HT films having the layers of conjugated backbones separated by layers of isolating alkyl chains [42]. The ability of P3HT to form highly ordered lamellar structure, however, depends on the degree of regioregularity of the P3HT backbones [43]. The significance improved mobility due to the change in regioregularity also reported by Bao et al. [44]. Regioregular P3HT has been shown to have very different properties from their corresponding regiorandom counterpart, such as better ordering and crystallinity in their solid states, and substantially improved electro-conductivities.

Whereas X-ray rocking curve measurements presented by Kline et al. [45] proposed that the increase of charge carrier mobility is actually due to the improved grain boundaries of the highly oriented crystals, which frequently correlate with increase of in-plane π - π stacking is only indirectly related to the in-plane π -stacking. With the improvement of such thiophene based polymers properties, it is possible now to obtain the field- effect mobility in between $0.1 \text{ cm}^2 \text{ V}^{-1} \text{ s}^{-1}$ to $0.5 \text{ cm}^2 \text{ V}^{-1} \text{ s}^{-1}$ [46-48].

P3HT thin films with high regioregularity (> 90%) prepared by drop casting also show higher mobility compared to spin coated thin films [24]. This was usually attributed to better ordering of polymer chains, due to very slow evaporation of the solvent during the process. Our recent image-plate measurements have also confirmed that such film contain better structural orientation compared to spin-coated samples as well as bigger crystallites size [49]. In general, drop casting thin films are often inhomogeneous or curved surfaces as well as controlling the thickness is still a major concern.

1.4.2. Dielectric Treatment

It is well established that the charges in OFETs are mainly accumulated in a very thin layer adjacent to the gate insulator layer [50]. Therefore one should have aim to enhance the mobility at this region (first 5-7 monolayers from the substrate) by enhancing the surface-interface mediated molecular ordering with these couple of layers. By doing this one can control the intermolecular interaction at the interface between P3HT and the insulator substrate by using the hydrophobic SAMs of HMDS or OTS (describe in detail under chapter 3).

Typically, charges are mainly transported and measured at the semiconductor/insulator

interface. Therefore, the quality of the dielectric at the semiconductor/insulator interface plays a crucial role in determining the charge carrier mobility. Under our studies we have considered the three different dielectric layers (SiO_2 , HMDS, OTS) in order to modify this substrate induced interaction via surface-interface engineering [51, 52, 53]. Further of this, the effect of oxygen plasma treatment has shown the further improvement of charge carrier mobility [54].

1.4.3. Annealing Treatment

As we know spin coating technique produces the as-grown P3HT thin films [56] within short time, where molecules do not get proper time to reorganise themselves, therefore produce more disordered film, where the morphologies are not in equilibrium or not optimised due to less time of film formation. Subsequently annealing is a necessary technological step in order to enhance the built-in performance of any polymer devices. For P3HTs thin film OFET devices, annealing importance firstly shown by Abdou et al. [55]. They have shown the significant improvement in the OFET characteristics after annealing P3HT thin films at 180 °C under the inert atmosphere. This improvement was attributed to a reduction of the free volume and trapped solvent, thus leading to more compact and ordered films. Currently, we have investigated the effect of annealing on the morphology of different molecular weights of P3HT under the number of heating cycles (chapter 5 and 7). We have found that annealing of P3HT also increases the crystallinity of the thin films as confirmed by the X-ray diffraction measurements. In this thesis instead of direct annealing up to some elevated temperature, we have heated up samples up to their melting point, in order to understand their thermodynamically properties, re-crystallization behaviour as well as their re-organising behaviour after cooling back to RT under chapters 5 and 7 for both fractions of P3HTs.

1.4.4. Molecular Weight

It is found that the charge carrier mobility in Poly(3-hexylthiophene) strongly affected by its molecular weight (M_w) [45, 56, 57]. Our earlier studies (Zen et al.) as well as Kline et al. have found independently that the charge carrier mobility in P3HT is strongly affected by its molecular weight (M_w) [45, 56, 57]. We have noticed that by varying the M_w one order of magnitude results in a four orders of magnitude change in the charge carrier mobilities in OFETs. To explain this behavior, there are two different models - Firstly, the grain boundaries model, proposed by Kline et al., It explains that the low molecular weight of P3HT consists of small crystallites separated by disordered region and in between two nearest crystal-

line domains, there is a grain boundary act as a huge barrier for charge carrier transport across the domains, in between that charge can trap. This ultimately reduces the overall mobility. Whereas, due to long molecular length, the high molecular weights fraction adopts the “spaghetti-like” molecules, where due to long chains molecules are interconnected with each other’s and bridging the gap, this ultimately facilitate the charge carriers smoothly from source to drain through both intra and inter chain transports. Instead, we have proposed (Zen et al.) that the crystallinity of P3HT is the crucial factor to determine the charge carrier mobility for different molecular weight fraction of P3HT.

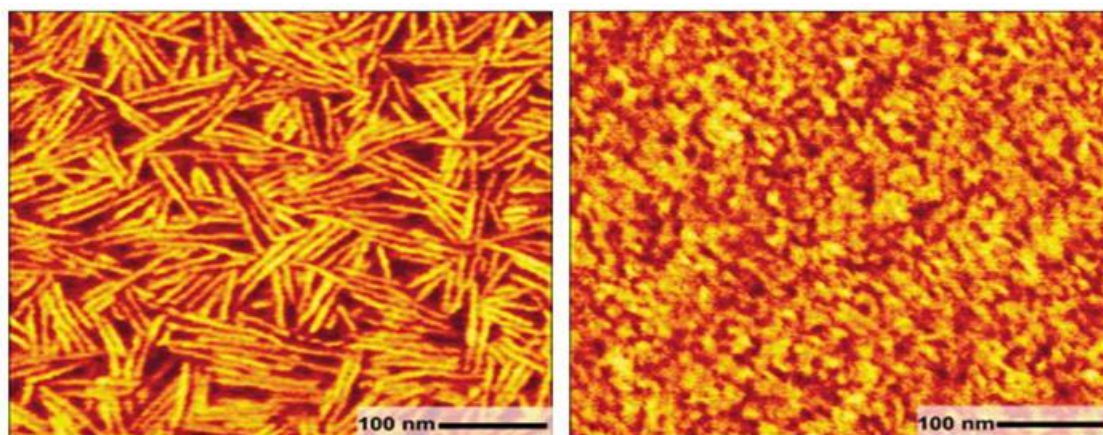


Figure 1.10 Atomic force microscopy images of regioregular P3HT films with M_w of (a) 3.2 kD and (b) 31.1 kD³⁴. The large molecular weight polymer forms a more ordered, crystalline film, yet has a mobility that is two orders of magnitude lower than the 3.2 kD films [49].

Kline et al. [49] have also shown the dramatic difference of morphology of different molecular weight (3.2 kD and 31.1 kD) with the help of AFM study of regioregular P3HT polymer films (Fig. 1.10), where the mobilities differ by more than two orders of magnitude [49].

Again depending upon the molecular weight, the crystallinity (the degree of structural order in any solid) of LMW of P3HT is significantly smaller (only 4.5%) than in the HMW of P3HT (18%) as measured by using differential scanning calorimeter as in powder form [57]. Further, for LMW the charge carrier transport probably is limited by the transport through quasi disordered region. Under our work, we have consider these two hypothesis and tried to understand low as well as high molecular weight P3HT crystallinity behavior utilizing these two models.

1.5. Charge Transport from Organic Materials

In recent years, a lot of research has been done on organic semiconductors. Small molecules based organic semiconductors being investigated over five decades [13], however, the discovery of conducting polymers and the work done to improve their conductivity [14] offered to revolutionize low cost electronic devices, as these materials could be processed in solution form and be a potential alternative of present electronic device materials.

Organic materials conducting property has been reported earliest around sixty years before, when photoconductivity and electroluminescence were detected in organic crystals, such as naphthalene and Anthracene [15–19]. Although, the crystals showed high charge carrier mobility, their processability was very poor with little potential for applications. In the 1980's electroluminescence was reported from double layer vacuum-sublimed molecular thin film devices [20], and from conjugated polymers such as poly(p-phenylene vinylene) (PPV) [21]. Since then, a new perspective has been opened on the applicability of organic molecules and semiconducting polymers into (opto) electronic devices. Beside the research in the field of polymer light-emitting diodes (LEDs), several other research fields based on polymer semiconductors have been developed in the past decade, such as field-effect transistors (FETs) [22–24] and photovoltaics [25–26]. The polymers used in these applications are processed from solution based techniques.

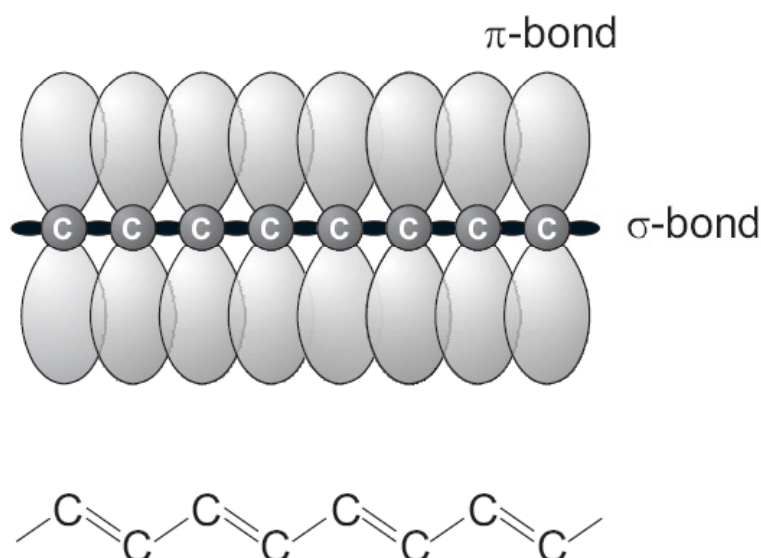


Figure 1.11 Schematic representations of the electronic bonds between carbon atoms (above) in polyacetylene molecule (below).

Their low cost production, resulting mainly from the easy processing methods, makes them interesting for the electronic industry as well as among the scientific community, but in order to be competitive with their inorganic counterparts; organic devices must provide comparable device performance with the already existing ones.

For electric conduction, they have a framework of alternating single and double carbon-carbon bonds. Single bonds are referred as σ bonds and are associated with a highly localized electron density in the plane of the molecule, and double bonds contain an σ -bond and a π -bond, where the π -bond is the overlap between p_z orbitals of neighboring atoms along the conjugation path. The conjugation of single and double bonds establishes a delocalization of the electrons [10] situated above and below the plane of molecules. π -bands are either empty (called the Lowest Unoccupied Molecular Orbital - LUMO) or filled with electrons (called the Highest Occupied Molecular Orbital - HOMO). The band gap of these materials determined from optical measurements and typically within the semiconductor range of 1–4 eV, which covers the whole range from infrared to ultraviolet region. A well known example of a conjugated polymer is polyacetylene, which consist of a single chain of alternating single- and double-bonds (Figure 1.11).

Going in more details, the charge transport in crystalline semiconductors and metals [58] has been well understood for many decades. In general, the transport is described by a band model where the electrons exist in well-defined energy bands. Charges typically have a mean free path of 10^{-1} nm and are scattered by phonons or impurities. Mobilities typically range from 10 - 10^4 cm^2/Vs . This regime is referred to as band transport. Adding disorder to the system substantially complicates the model and invalidates the periodic boundary conditions. Amorphous silicon is a classical example that took many decades to understand. The properties of amorphous silicon differ substantially from crystalline silicon. The mobility is more than two orders of magnitude lower in amorphous silicon.

However, the charge carrier mobilities in organic semiconducting films are lower than those in the case of inorganic semiconductors. Single crystal OFETs, however, are quicker, smaller and offer higher mobilities than thin film OFETs. Mobilities in Rubrene single crystal transistors have been reported to be as high as 15.4 cm^2/Vs [59]. These are higher than the mobilities found in amorphous silicon thin film transistors. Impurities in the chemical structure or defects in the semiconducting film [60], contact effects, and general artefacts from processing can seriously affect the output characteristics of these devices. Mobility measurements via single crystal OFETs are thought to give more accurate information on charge carrier mobilities and transport characteristics. However, the point should be made that some-

times the general transport conditions in the film are the focus of interest. Changes in the charge carrier field effect mobility can indicate changes in the quality of the film. This is a potential method to screen processing conditions of films, such as the solvent used, the concentration of the solution, parameters for tempering, etc. Mobility measurements can be made on blends of semiconducting materials in the OFET structure, and the mobilities of both charge carrier types can be determined from the same device.

1.5.1. Charge Carrier Mobility

Despite impressive progress of charge carrier mobility values for organic thin-film transistors during past two decades, charge transport in organic materials still remains a controversial. The earliest work only focused on the increase of such material conductivity σ to inorganic counterparts [61]. Basically, for the disordered materials or polymer materials the charge can mainly transport through hopping process via interchain transport.

The charge carrier mobility (μ), which is the charge motion along a particular direction i.e. from source to drain after applying the external electrical field in such semicrystalline materials rapidly accelerate up to a steady state velocity v under the influence of an electric field E , given by

$$v = \mu \times E \quad (1.1)$$

The charge carrier mobilities in such organic semiconductors are measured using several techniques namely- organic field-effect transistors (OFET), pulse-radiolysis microwave conductivity (PR-TRMC), space charge limited current (SCLC), and time of flight measurement (TOF). The mobilities in conjugated polymers are usually too low to be measured by the Hall effect. All the mobility measurements shown in this thesis have been done by utilizing the first two methods by our collaborators (Neher et al., Potsdam, Germany). At the same time each technique measured only a specific mobility. In fact, each measurement will give different values of mobility even if we use the same polymer/oligomer.

Vissenberg et al. [62], assumes the variable range hopping in an exponential distribution of traps. The model predicts a thermally activated mobility. At the same time it predicts that the mobility also depends on the gate voltage according to the power law, shown by the typical devices. This model becomes very fruitful in the analysis of current-voltage curves of OFET devices. Briefly, as the gate voltage increases, injected charge carriers tend to fill the traps, so trapping becomes less efficient and charge transport improves. In contrast, when the

semiconductors become partially ordered, this variable range hopping will not be valid. Whereas Salleo et al. [63] have utilized the mobility edge model to describe the charge transport through such organic films. This model is similar to the multiple trap and release model, used to describe the typical amorphous silicon material as well as applicable for small molecular organic material [64]. The obvious dependence of the mobility of OFETs on number of carriers is due to the small portion of the carriers induced by the gate become mobile and move towards drain. Whereas the maximum number of carriers get trapped in the localized states and screen the gate field. Therefore, increasing the gate voltage increases the portion of carriers to move above the required mobility edge, resultant the increase of the number of mobile carriers and thus the effective mobility.

At the same time, Anderson et al. have also shown that appearance of disorder in any solid state may cause a localization of the states and resultant the charge transport will occur via tunnelling (hopping) between two localized states [65]. Considering the organic materials, the states between HOMO and LUMO are localized states. In this case, hopping of carriers from one state to the next is supervised by phonons.

The well known Holstein model [66] known for the thermally induces process of carriers movement, Holstein predicts a linear relationship of the mobility with changing temperature ($\ln \mu$ Vs $1/T$). He considered that transport of charge carriers in organic materials is due to the polarons. The mobility of the charge carriers is described by the Arrhenius equation given below

$$\mu = \mu_0 \exp\left(-\frac{E_b}{2KT}\right) \quad (1.2)$$

Where T is the temperature, k is the Boltzmann constant, μ_0 is the mobility for $T \rightarrow \infty$ and $E_a = E_b/2$ is the activation energy, with E_b the polaron binding energy. Whereas the Bässler's model [67, 68], assumed that both HOMO (LUMO) having the Gaussian distribution as well as their energy levels are not in same energy. Applying the external field E can vary the mobility and this particular dominates more when the high fields exceeding 1 MV/m.

$$\mu(E) = \mu_0 \exp(\beta\sqrt{E}) \quad (1.3)$$

Summarizing, at present the quality of devices has improved a lot, both of these features (thermally activated mobility as well as gate bias dependent) now encountered less significant than before. This might be the hint that all these appeared due to the present of defects inside crystals.

1.5.2. Intrachain Transport

Generally, the charge transport properties are dependent on the charge carrier density [69]. Charge carrier transport of π type semiconductor polymer in solid state (bulk or film) is classified mainly into two different categories- intrachain, interchain [70]. In crystals with ordered backbone chains, charge carrier can in theory transport along the polymer up to its contour length [71] as well as transported between π -conjugated planes in the crystals. Finally the charge carriers can transfer across crystalline grain boundaries through hopping. For spin cast RR-P3HT films, Kline et al. proposed that the HMW molecules form small ordered areas separated by disordered region [72]. In this case the long chains can interconnect ordered areas to prevent the charge carriers from being trapped by the disordered grain boundaries.

Single molecule based electronic devices comes under vast field of molecular electronics. Where the charge transferred only possible through along the long molecular length without or merely have to hop. Therefore the response (on-off ratio) as well as overall mobility should be high at the drain end. The main concerns for single molecular device are the technical realization and contacts of single molecule from both ends with the source and drain as well as contact resistance at the metal-molecular junction. At the same time short, parallel backbone molecules are better than twisted and long chain length molecules. The example of intrachain transport is shown under Fig. 1.12.

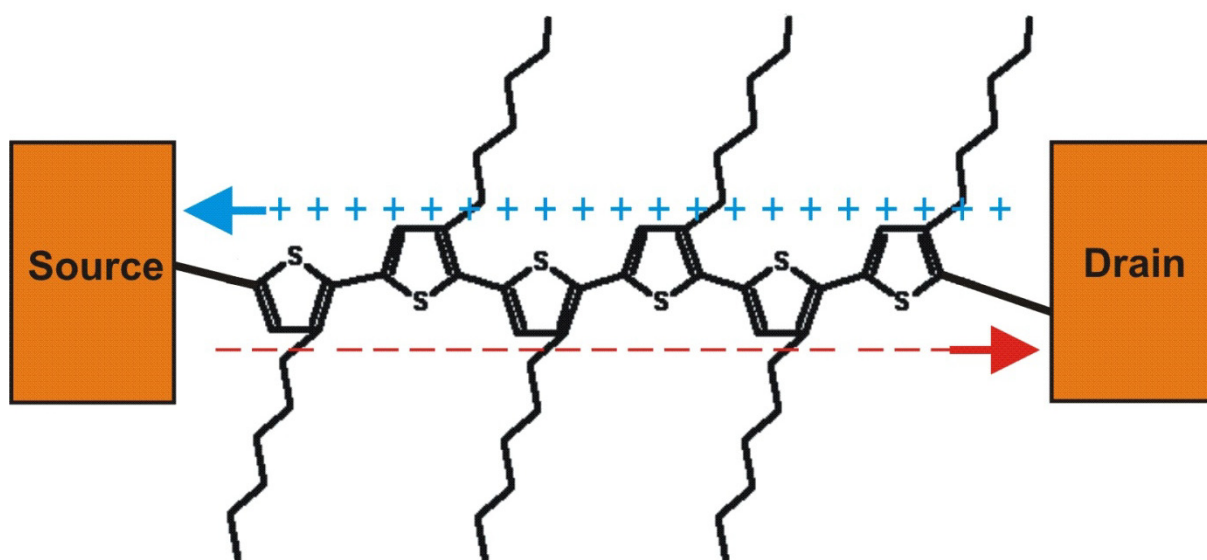


Figure 1.12 Representation of an intrachain transport using Poly(3-hexylthiophene) single molecule.

Based on high frequency time-resolved microwave (30 GHz) conductivity measurements, Prins et al. have found the intrachain mobility in the solid samples of ladder-type

poly(p-phenylenes) (LPPP) of $30 \text{ cm}^2/\text{Vs}$ [17]. The value was determined by considering one-dimensional diffusive motion along the polymer backbone.

At the same time Chang et al. have established a correlation between the mobility and the interchain/intrachain disorder as accessed by optical and electro-optical spectroscopy, which suggests that, in the high mobility regime $\mu = 10^{-1} \text{ cm}^2/\text{Vs}$; the mobility is limited by the crystalline quality of the P3HT crystals, opposite to grain boundaries between the crystals [73].

1.5.3. Interchain Transport

The ability to induce different orientations (edge-on/flat-on) allows one to establish a direct correlation between the direction of π - π stacking and the in-plane OFET mobility [24]. At room temperature, the highest mobility of 0.05 - $0.1 \text{ cm}^2/\text{Vs}$ are observed for the sample having the highest regioregularity 96% and the largest size of crystallites with in-plane orientation of the (020) [74]. For spin-coated sample with 81% regioregularity, π - π planes oriented normal to substrate [24]. The mobility is only 2×10^{-4} in spite of pronounced in-plane crystallinity along the (100) axis with a grain size of 13 nm.

This is consistent with the FET mobility being limited by π - π interchain, rather than intrachain transport. Therefore the carriers transport between next neighboring molecules, also called the interchain transport is quite slower compared to intrachain transport because the hopping process takes place between orbitals of next neighboring chains. In order to increase this hopping process one needs the smallest distance between next neighboring chains, for P3HT case it is 0.38 nm. This ultimately demands the closed molecular packing while the film under preparation using the various solutions cast methods.

1.6. Phase Behavior and Polymer-Polymer Interface

The analytical techniques are widely used to study the polymer interfaces. Where the Landau theories of phase transitions [75] basically work well with polymeric liquid crystals, where the phenomena of interest occur at length scales that greatly exceed the fundamental molecular dimensions (e.g. monomer size), where it is often possible to explicitly “coarse-grain” a microscopic description into a phenomenological one, thus providing microscopic expressions for the phenomenological coefficients.

The complicated polymeric systems partly simplify the physics. For example, the very fruitful approach to study the systems near to its critical point is based on the de Gennes ran-

dom phase approximation (RPA) [76] for the scattering intensity. de Gennes showed that the mean-field theory is rather good for high molecular mass mixtures, in contrast to the low molecular mass mixtures, for which the mean-field theory breaks down close to the critical point.

1.6.1. Landau-de Gennes Free Energy Functional

The effect of interface alignment is known from liquid crystals [77] and decays exponentially from the interface towards the bulk. It could also be useful for studying the polymer-substrate interfaces as well. The particular control of the interface potential could help for a better understanding of thickness dependence of mobility along the interface region of the thin films.

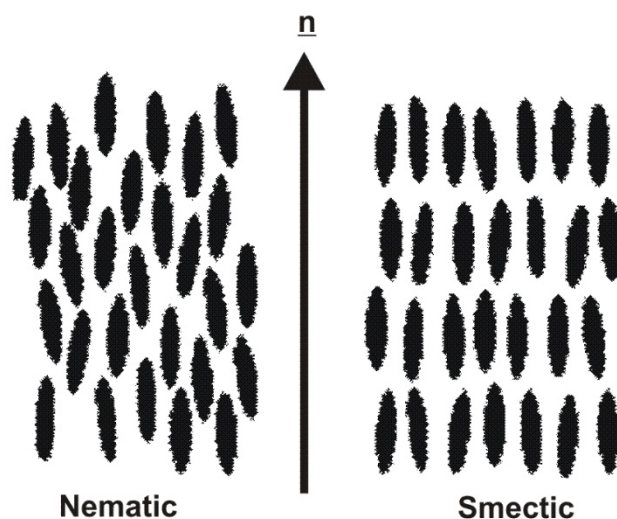


Figure 1.13 Nematic and Smectic phases of the liquid crystals.

Surface effects in liquid crystals (Fig. 1.13) have mainly been studied in nematic liquid crystals. The first reason for this is the simplicity of their structure-the local order aligning molecules parallel to each other can extend to a macroscopic scale. As revealed by the studies of free surfaces by X-ray reflectivity measurements, the molecular structure and the local ordering of liquid crystals play an important role in the determination of interface structures. Liu and Fredrickson [78] have calculated a free energy functional that depends on two order parameters, namely the concentration and orientational density of polymer segments. The phase behaviour of flexible polymers is described in terms of a single order parameter, which is a composition of one type of polymers.

However, due to the fact that individual monomers may have a rigid, anisotropic character, a description of stiff polymers must include the orientational density as a second order

parameter. To describe both the isotropic-nematic transition and ordinary phase separation, they have expanded to arbitrary order in concentration and up to fourth order in orientation density, by combining the density functional theory with the Landau-de Gennes theory for the orientational order parameter. They have used a microscopic model of wormlike chains rather than Gaussian chains to calculate the expansion coefficients. They have explicitly computed the coefficients of the terms in the free energy expansion, so that they are not unknown parameters. The nonlocal terms in both the concentration and the orientational density are included. The expression for the free energy functional obtained by Liu and Fredrickson is shown below

$$F = F_{FH} + F_{LDG} \quad (1.4)$$

Where F_{FH} is the usual Flory-Huggins free energy density and

$$F_{LDG} = \frac{1}{2}(B - \omega) \mathbf{S}^2 - \frac{C}{3} \mathbf{S}^3 + \frac{D}{4} \mathbf{S}^4 \quad (1.5)$$

Where \mathbf{S} is the orientational order parameter, ω is the Maier-Saupe parameter and the coefficients B , C , D represent the entropic cost of orienting chains and depend up on the flexibility parameter, κ (the ratio of elastic bending constant to the thermal energy), and φ , composition of polymers. κ defines the flexibility of the polymers and it gives the persistence length in units of bond length.

Using above free energy function one can study phase behaviours of flexible and semi-flexible polymers. Lee et al. [79] have studied the phase behaviour of the liquid crystalline polymer/model compound mixtures using this free energy function. Their experimental data agree very well with that obtained from the eq. (1.4).

The average orientation of the molecules in a fixed volume and the order parameter Q , characterizes the distribution of the orientations of the molecules. It is defined as the average over all the molecules of the volume, describe the bulk state of these two phases.

When the molecules are perpendicular or tilted with respect to the layer plane, the existing order at the interface found in the smectic phases; this order is characterized by the superposition of a nematic-like orientational order and a positional order in which the molecules form successive layers.

When the substrate is covered with a film of surfactant or silane forming a layer of aliphatic chains protruding from the surface, a possible alignment mechanism is that the nematic molecules penetrate the layer of aliphatic chains. They then adopt the orientation of these

chains, which leads to a homeotropic or conical anchoring depending on the chains orientation [80, 81, 82].

The behavior at interfaces for liquid crystals approaching a phase transition is analogous to the behavior of other fluid systems. One can distinguish three types of phenomena.

Let us first consider the case of a second-order transition between an ordered and a disordered phase. When such transition is approached from the disordered phase in which the order parameter of the transition is zero, fluctuations of this order parameter appear in the bulk with a correlation length ε which diverges at the transition. If the system is in contact with an interface favoring the ordered phase, the correlation length at the surface will become infinite in a direction parallel to the surface plane. This creates an ordered layer at the surface in which the order parameter decreases exponentially from a non-zero value at the surface to zero in the bulk over a penetration length ε_s ; ε_s is equal to the correlation length ε and thus it diverges at the transition. This phenomenon is called critical adsorption [83].

When the transition is first order, the situation is more complex. I will just briefly describe the main features and further details can be found elsewhere [84, 85, 86]. When the transition between two phases I and II is approached, say from phase I, a layer of phase II can form at the surface: phase II is said to wet the surface. If the thickness of the phase II layer becomes infinite at coexistence, wetting is complete; if the thickness remains finite at coexistence wetting is partial [87]. When one explores the coexistence curve between phases I and II, one can go from a partial wetting regime to a complete wetting regime via a wetting transition [88, 89, 90]. This wetting transition can be first- or second-order [91, 92, 93]. If it is first order, there is a line of first-order surface transition extending off coexistence, where the wetting film exhibits a jump in thickness (thin-thick film transition); this line is called the pre-wetting line and ends at a pre-wetting critical point [90]. The relevant parameter of the wetting transition is in fact the adsorption: $\zeta = \int_0^\infty [\eta(z) - \eta_{\text{bulk}}] dz$, where $\eta(z)$ is the order-parameter profile and $\eta_{\text{bulk}} = \eta(z = \infty)$ is the order parameter in the bulk.

1.7. References

- [1]. F. Garnier, “Scope and limits of organic-based thin-film transistors,” *Phil. Trans.*, Vol. 355, pp. 815–827, 1997.
- [2]. C. D. Dimitrakopoulos and D. J. Mascaro, “Organic thin-film transistors, a review of recent advances,” *IBM J. Res. Dev.*, vol. 45, pp. 11–27, 2001.
- [3]. J. M. Shaw and P. F. Seidler, “Organic electronics: Introduction,” *IBM J. Res. Dev.*, Vol. 45, pp. 3–9, 2001.
- [4]. H. Sirringhaus, “Device physics of solution processed organic field-effect transistors, *Adv. Mat.*, vol. 17, pp. 2411–2425, 2005.
- [5]. Frommer, J. E.; Chance, R. R. In *Encyclopedia of Polymer Science and Engineering*, Vol. 5; Wiley: New York, 1986.
- [6]. Ito, T.; Shirakawa, H.; Ikeda, S. *J. Polym. Sci. Chem. Ed.*, 12, 11, 1974.
- [7]. Chiang, C. K.; Park, Y. W.; Heeger, A. J.; Shirakawa, H.; Louis, E. J.; MacDiarmid, A. G. *Phys. Rev. Lett.*, 39, 1098, 1977.
- [8]. Roncali, J. *Chem. Rev.*, 92, 711, 1992.
- [9]. Wilbourn, K.; Murray, R. W. *J. Phys. Chem.*, 92, 3642, 1988.
- [10]. Heinze, J. *Electronically Conducting Polymers*. In *Topics in Current chemistry*, Vol. 152; Springer-Verlag: Berlin, 1990.
- [11]. Chung, T. C.; Kaufman, J. H.; Heeger, A. J.; Wudl, F. *Phys. Rev. B*, 30, 702, 1984.
- [12]. Bredas, J.; Chance, R.; Silbey, R. *Phys. Rev. B*, 26, 5843, 1982.
- [13]. M. Pope and C. E. Swenberg, *Electronic Processes in Organic Crystals and Polymers*, University Press, Oxford, second edition, 1999.
- [14]. H. Shirakawa, E. J. Louis, A. G. MacDiarmid, C. K. Chiang, and A. J. Heeger, *J. Chem. Soc. Chem. Comm.*, 579, 1977.
- [15]. H. Mette, *Z. Physik* 134, 566, 1953.
- [16]. R. G. Kepler, *Phys. Rev.* 119, 1226, 1960.
- [17]. O. H. Le Blanc, *J. Chem. Phys.* 33, 626, 1960.
- [18]. M. Pope, H. P. Kallmann, P. Magnante, *J. Chem. Phys.* 38, 2042, 1963.
- [19]. H. Hoegl, *J. Phys. Chem.* 69, 755, 1965.

- [20]. C. W. Tang, S. A. Van Sylke, *Appl. Phys. Lett.* 51, 913, 1987.
- [21]. J. H. Burroughes, D. D. C. Bradley, A. R. Brown, R. N. Marks, K. Mackay, R. H. Friend, P. L. Burns, A. B. Holmes, *Nature* 347, 539, 1990.
- [22]. H. Koezuka, A. Tsumura, Y. Ando, *Synth. Met.* 18, 699, 1987.
- [23]. A. R. Brown, A. Pomp, C. M. Hart, D. M. de Leeuw, *Science* 270, 972, 1995.
- [24]. H. Sirringhaus, P. J. Brown, R. H. Friend, M. M. Nielsen, K. Bechgaard, B. M. W. Langeveld-Voss, A. J. H. Spiering, R. A. J. Janssen, E. W. Meijer, P. Herwig, D. M. de Leeuw, *Nature* 401, 685, 1999.
- [25]. G. Yu, K. Pakbaz, A. J. Heeger, *Appl. Phys. Lett.* 64, 3422, 1994.
- [26]. P. Schilinsky, C. Waldauf, C. J. Brabec, *Appl. Phys. Lett.* 81, 3885, 2002.
- [27]. J. E. Lilienfeld, U. S. Patent 1745175, 1930.
- [28]. W. Shockley, G. L. Pearson, *Phys. Rev.* 74, 232, 1948.
- [29]. D. Kahn, M. M. Atalla, IRE Solid-State Device Research Conference, Carnegie Institute of Technology, Pittsburgh, 1960.
- [30]. S. M. Sze, *Physics of semiconductor devices*, 2nd Ed., John Wiley & Sons, New York, 1981.
- [31]. Kawai, T.; Kuwabara, T.; Wang, S.; Yoshino, K. *Jpn. J. Appl. Phys.*, 29, 602, 1990.
- [32]. Kim, S. R.; Choi, S. A.; Kim, J. D.; Kim, K. J.; Lee, C.; Rhee, S. B. *Synth. Met.*, 71, 2027, 1995.
- [33]. Dekker, Marcel *Handbook of Conducting Polymers* New York, 2nd ed. and New York 1986, 1st ed., 1998.
- [34]. Chen, L.; Godovski, D.; Inganaes, O.; Hummelen, J. C.; Janssens, R. A. J.; Svensson, M.; Andersson, M. R. *Adv. Mater.*, 12(18), 1367, 2000.
- [35]. Paloheimo, J.; Stubb, H.; Lahti, Y. P.; Kuivalainen, P. *Synth. Met.*, 41-43, 563, 1991.
- [36]. Lim, W. Y.; Nagamatsu, S.; Takashima, W.; Endo, T.; Rikukawa, M.; Kaneto, K. *IEICE Trans. Electron.*, E83-C, 1071, 2000.
- [37]. Bao, Z.; Rogers, J. A.; Katz, H. E. *J. Mater. Chem.*, 9, 1895, 1999.
- [38]. Zen., A.; PhD thesis, Potsdam, Germany, 2006.
- [39]. McCullough, R. D. *Adv. Mater.*, 10, 93, 1998.
- [40]. Loewe, R. S.; Khersonsky, S. M.; McCullough, R. D. *Adv. Mater.*, 11, 250, 1999.

- [41]. Chen, T. A.; Wu, X. M.; Rieke, R. D. *J. Am. Chem. Soc.*, 117, 233, 1995.
- [42]. Prosa, T. J.; Winokur, M. J.; Moulton, J.; Smith, P.; Heeger, A. J. *Macromolecules*, 25, 4364, 1992.
- [43]. Yang, C.; Orfino, F. P.; Holdcroft, S. *Macromolecules*, 29, 6510, 1996.
- [44]. Bao, Z.; Dodabalapur, A.; Lovinger, A. J. *Appl. Phys. Lett.*, 69, 4108, 1996.
- [45]. Kline, R. J.; McGehee, M. D.; Toney, M. F. *Nature Mater.*, 5, 222, 2006.
- [46]. Sirringhaus H, Brown P J, Friend R H, Nielsen, M M, Bechgaard K, Langeveld-Voss B M W, Spiering A J H, Janssen R A J, Meijer E W, Herwig P and de Leeuw D M, *Nature*, 401 685-688, 1999.
- [47]. Ong, B. S.; Wu, Y.; Liu, P.; Gardner, S. J. *Am. Chem. Soc.*, 126, 3378-3379, 2004.
- [48]. McCulloch, I.; Heeney, M.; Bailey, C.; Genevicius, K.; Macdonald, I.; Shkunov, M.; Sparrowe, D.; Tierney, S. Wagner, R.; Zhang, W.; Chabinyc, M. L.; Kline, R. J.; McGehee, M. D.; Toney, M. F. *Nat. Mater.*, 5, 328-333, 2006.
- [49]. Kline, R. J.; McGehee, M. D.; Kdnikova, E. N.; Liu, J.; Frechet, J. M. J. *Adv. Mater.*, 15, 1519, 2003.
- [50]. Tanase, C.; Meijer, E. J.; Blom, P. W. M.; de Leeuw, D. M., *Org. Electronics*, 4, 33, 2003.
- [51]. Merlo, J. A.; Frisbie, C. D. *J. Polym. Sci. Polym. Phys.*, 41, 2674, 2003.
- [52]. Gorjanc, T. C.; Levesque, I.; Dlorio, M. *Appl. Phys. Lett.*, 84, 930, 2004.
- [53]. Park, S. K.; Kim, Y. H.; Han, J. I.; Moon, D. G.; Kim, W. K.; Kwak, M. G. *Synth. Met.*, 139, 377, 2003.
- [54]. Yang, Y. S.; Kim, S. H.; Lim, S. C.; Lee, J.; Lee, J. H.; Do, L.; Zyung, T. *Appl. Phys. Lett.*, 83, 3939, 2003.
- [55]. Abdou, M. S. A.; Lu, X.; Xie, Z. W.; Orfino, F. P.; Deen, M. J.; Holdcroft, S. *Chem. Mater.*, 7, 631, 1995.
- [56]. Zen, A.; Pflaum, J.; Hirschmann, S.; Zhuang, W.; Jaiser, F.; Asawapirom, U.; Rabe, J. P.; Scherf, U.; Neher, D. *Adv. Funct. Mater.*, 14, 757, 2004.
- [57]. Zen, A.; Saphiannikova, M.; Neher, D.; Asawapirom, U.; Scherf, U. *Chem. Mater.*, 17, 781, 2005.
- [58]. C. Kittel, *Introduction to solid state physics*, 7th Ed., John Wiley and Son, Inc., 1996.
- [59]. V. C. Sundar, J. Zaumseil, V. Podzorov, E. Menard, R. L. Willett, T. Someya, M. E. Gershenson, and J. A. Rogers, *Science* 303, 1644, 2004.

- [60]. G. Horowitz, *Adv. Mater.* 13, 53, 2003.
- [61]. Pasveer, W. F.; Cottaar, J.; Tanase, C.; Coehoorn, R.; Bobbert, P. A.; Blom, P. W. M.; de Leeuw, D. M.; Michels, M. A. J. *Phys. Rev. Lett.*, 94, 206601, 2005.
- [62]. M. C. J. M. Vissenberg, *M. Matters*, *Phys. Rev. B.* 57, 12964-12967, 1998.
- [63]. Salleo, T. W. Chen, A. R. Volkell, *Phys. Rev. B.*, 70, 115-311, 2004.
- [64]. G. Horowitz, M. Hajlaoui, R. Hajlaoui, *J. Appl. Phys.* 87, 4456-4463, 2000.
- [65]. Anderson, P. W. *Phys. Rev.*, 109, 1492, 1958.
- [66]. Holstein, T. *Ann. Phys.*, 8, 343, 1959.
- [67]. Pautmeier, L.; Richert, R.; Bäessler, H. *Synth. Met.*, 37, 271, 1990.
- [68]. de Boer, R. W. I.; Gershenson, M. E.; Morpurgo, A. F.; Podzorov, V. *Phys. Stat. Sol. A*, 201, 1302, 2004.
- [69]. Roichman, Y., Tessler, N., *Appl. Phys. Lett.* 80, 1948-1950, 2002
- [70]. Shimomura, T.; Sato, H.; Furusawa, H.; Kimura Y.; Okumoto, H.; Ito, K.; Hayakawa, R.; *Phy. Rev Lett.*, 72, 2073-2076, 1994.
- [71]. H. Yang, T. J. Shin, Z. Bao, Chang Y. Ryu., *J. Polym. Sci.: Part B: Polymer Phys.*, 45, 1303-1312, 2007.
- [72]. Kline, R. J.; McGehee, M. D.; Kadnikova, E. N.; Liu, J.; Frechet, J. M. J.; Toney, M. F. *Macromolecules*, 38, 3312, 2005.
- [73]. Jui-Fen Chang, Jenny Clark, Ni Zhao, Henning Sirringhaus, Dag W. Breiby, Jens W. Andreasen, Martin M. Nielsen, Mark Giles, Martin Heeney, and Iain McCulloch
- [74]. B. E. Warren, *X-ray diffraction*, Addison-Wesley, Reading, MA, 1969, 41-50.
- [75]. L. D. Landau and E. M. Lifschitz. *Statistical Physics*. Pergamon Press, Oxford, 1958.
- [76]. P. G. de Gennes. *Scaling Concepts in Polymer Physics*. Cornell University Press, Ithaca and London, 1979.
- [77]. F. S. Bates and G. H. Fredrickson. *Macromolecules*, 27:1065, 1994.
- [78]. Gennes, P. G.; Prost, J.; *The physics of liquid crystals*, 2nd ed.; Birman, S.; Edwards, S. F.; Llewellyn, C. H.; Rees, S. M.; Oxford University press: New York, Vol. 10, p 507, 1993.
- [79]. S. Lee, A. G. Oertli, M. A. Ganno, A. J. Liu, D. S. Pearson, H. W. Schmidt, and G. H. Fredrickson. *Macromolecules*, 27:3955, 1994.

- [80]. Porte, J. *Physique* 37 1245-52, 1976.
- [81]. Hiltrop K and Stegemeyer H., *Ber. Bunsenges. Phys. Chem.* 85 582-8, 1981.
- [82]. Hiltrop K and Stegemeyer H., *Liquid Crystals and Ordered Fluids Vol 4* Ed. A. C. Griffin and J. F. Johnson (New York: Plenum) pps15-30, 1984.
- [83]. Fisher M E and de Gennes P C., *C.R. Acad. Sci. Paris, B* 287 207-9, 1978.
- [84]. Sullivan D E and Telo da Gama M. M., *Fluid Interfacial Phenomena* Ed C A Croton (New York: Wiley), Ch 2, pp45-134, 1986.
- [85]. Dietrich S., *Phase Transitions and Critical Phenomena, Vol 12*, Ed C Domb and J. Lebowitz (London: Academic), 1988.
- [86]. Schick M., *Liquids at Interfaces Les Houches Summer School Lectures, Session XL VIII* Ed. J Charvolin, J F Joanny and I Zinn-Justin (Amsterdam: North-Holland) pp 475-97, 1988.
- [87]. Dash J G, *Phys. Rev. B* 15, 3136-46, 1977.
- [88]. Cahn J W, *J. Chem. Phys.* 66 3667-72, 1977.
- [89]. Ebner C and Saam W F, *Phys. Rev. Lett.* 38 1486-9, 1977.
- [90]. Pandit R, Schick M and Wonis M, *Phys. Rev. B* 26 5112-40, 1982.
- [91]. Sullivan D E, *Phys. Rev. B* 20 3991-4000, 1979.
- [92]. Sullivan D E, *J. Chem. Phys.* 74 2604-15, 1981.
- [93]. Pandit R and Wortis M, *Phys. Rev. B* 25 3226-41, 1982.

Chapter 2

X-ray Scattering Techniques

2.1. Introduction

X-ray has become an invaluable tool to probe the structure of matter. It has revolutionized our life by helping scientists to unravel such mysteries as the structure of DNA and in more recent times, the structure of proteins. The main reason for this unprecedented success is that the X-ray wavelength, which determines the smallest distance one can study with such a probe, is comparable to the inter-atomic dimension. For research in the fields of physics, chemistry, biology and materials science, photons ranging from radio frequencies to hard γ -rays provide some of the most important tools for scientists. Since X-rays discovered by W.C. Roentgen [1845-1923] in 1895 [1], Subsequent experiments, conducted by Max von Laue and his students, showed that X-rays are of the same nature as visible light but with shorter wavelength.

In this work, X-rays are used to investigate the structural properties of π conjugated polymer (P3HT). As all measurements were done using different synchrotron sources with varying energy from 8 keV to 16 keV having wavelength from 0.154 nm to 0.08 nm, therefore only the interactions of photons have been considered and inelastic scattering has not been taken into account.

2.2. Index of Refraction

When Roentgen discovered X-rays in 1895, he immediately searched for a means to focus them [1, 2]. On the basis of slight refraction in prisms he stated that the index of refraction of X-rays in materials cannot be much more than $n = 1.05$ if it differed at all from unity. Twenty years later, Einstein proposed [3] that the refractive index for X-rays was $n = 1 - \delta$, where $\delta = 10^{-6}$, allowing for total external reflection at grazing incidence angles. A simple classical model in which an electron of the material is considered to be accelerated by the electromagnetic field generated by X-rays shows that the complex dielectric constant ε can be described as

$$\varepsilon = 1 - \frac{4\pi\rho Ze^2}{m\omega} \left(1 + \frac{i}{\mu\omega}\right) \quad (2.1)$$

where ρ is the electron density of the material, ω is the frequency of the electro-magnetic field, μ is the absorption length, e is the charge of electron, m is the mass of electron and Z is the atomic number of the element. The results of a more accurate quantum mechanical treatment are qualitatively similar

$$n = \sqrt{\epsilon} = 1 - \delta(r) + i\beta(r) \quad (2.2)$$

where the real and imaginary parts of the index of refraction, δ and β , account for the scattering and absorption of material, respectively. They are defined as

$$\delta(r) = \frac{r_e}{2\pi} \lambda^2 \rho_{el} \quad (2.3)$$

$$\beta(r) = \frac{r_e}{2\pi} \lambda^2 \sum_k \frac{f_k''}{V_m} = \frac{\lambda}{4\pi} \mu(r) \quad (2.4)$$

where $r_e = 2.813 \times 10^{-5} \text{ \AA}$ is the classical radius of the electron, V_m is the volume of the unit cell, Z_k is the number of electrons of atom k in the unit cell, f' and f'' are the anomalous scattering coefficients, and λ is the X-ray wavelength. If the X-ray wavelength λ is different from comparison with the principal absorption energies, $\beta \approx 10^{-7} \dots 10^{-8}$ and $\delta \approx r_e \lambda^2 \rho / (2\pi)$. $\rho_{el}(r)$ is the electron density and $\mu(r)$, the linear absorption coefficient of the material. The magnitudes of δ and β are simply related to the electron density of the material and of the order of 10^{-5} to 10^{-7} [4]. The real part, $n = 1 - \delta$, is connected to the phase-lag of the propagating wave, the imaginary part, β corresponds to the decrease of the wave amplitude [4].

2.3. X-ray Interaction with Matter

The X-rays are electromagnetic waves; therefore, they undergo refraction phenomena at interfaces between different media. To describe such refractive phenomena, matter is taken to be homogeneous with sharp boundaries between the media. Each medium is characterised by an index of refraction n . By definition the refractive index for vacuum is one. As a result, in the X-ray region, for condensed matter n turns out to be less than unity. The refractive index $n(r)$ can be expressed as eq. (2.2) followed by their real and imaginary parts as in eqs. (2.3) and (2.4). As $\delta(r)$ is proportional to the product of the r_e with electron density $\rho_{el}(r)$, the deviation of n from unity is related to the scattering properties of the medium. The relation of the atomic scattering form factor with the index of refraction will be made explicit hereafter.

The atomic form factor is defined in eq. (2.5), as a function of X-ray wavelength λ and of the scattering vector Q [4, 5].

$$f(Q, \lambda) = f^0(Q) + f'(\lambda) + if''(\lambda) \quad (2.5)$$

Where f' and f'' are the real and the imaginary part of the dispersion correction, respectively. The energy dependence of the dispersion corrections presents discontinuities at the absorption edges and is dominated by the binding energy of the inner-shell electrons of the atom. In the limit for $Q \rightarrow 0$, $f_0(Q) = Z$, the number of electrons Z in the atom, whereas, for $Q \rightarrow \infty$, $f_0(Q) = 0$. Based on eq. (2.5), the index of refraction can be rewritten as

$$n = 1 - \frac{2\pi\rho_{el}r_e}{k^2} \{f^0(0) + f' + f''\} \quad (2.6)$$

With $\beta = -\left(\frac{2\pi\rho_{el}r_e}{k^2}\right)f''$. The properties of the dispersion corrections of the atomic form factors f' and f'' can be exploited to perform anomalous scattering experiments. The Snell's law relates the incident grazing angle α_i to the refracted angle α_i' in the matter, as shown in eq. (2.7).

$$\cos \alpha_i = n \cos \alpha_i' \quad (2.7)$$

As the index of refraction is smaller than 1 for X-rays, the phenomenon of the total external reflection occurs for incident angles α_i smaller than the critical angle, α_c . Starting from eqs. (2.5) and (2.7) and setting $\alpha_i' = 0$, the critical angle for total external reflection is obtained as

$$\alpha_c = \sqrt{2\delta} = \lambda \sqrt{r_e \rho_{el}} \quad (2.8)$$

Being $\delta \approx 10^{-5}$, α_c is in the order of the tenth of a degree (e.g. $\alpha_c = 0.22^\circ$, for Si at 8 keV). For α_i smaller than α_c , an evanescent wave is created, which travels parallel to the surface with an amplitude decaying rapidly in the material on the nm-scale. The phenomenon of the total external reflection is shown schematically in Fig. 2.1.

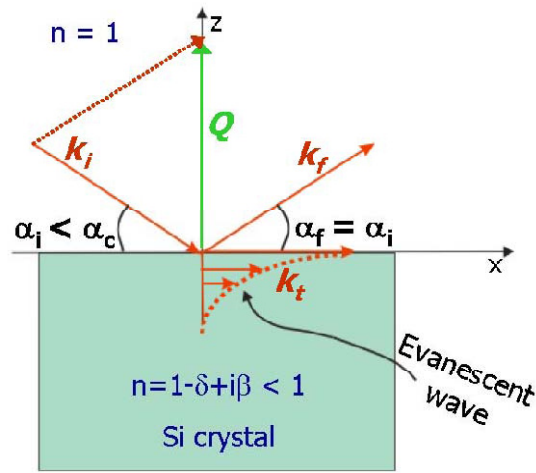


Figure 2.1 An X-ray wave with wave vector k_i hits a surface under a grazing angle α_i smaller than α_c . The wave splits into a reflected wave of wave vector k_f at $\alpha_f = \alpha_i$ and a transmitted (or refracted) wave with wave vector k_t travelling parallel to the surface. $Q = k_i - k_f$ represents the total momentum transfer of the scattering process.

2.4. The Evanescent X-ray Wave

The amplitude of the transmitted and reflected waves are calculated, based on the continuity of the electric and magnetic fields at the interface ($z = 0$). The z component of the incoming and transmitted waves are $k_{i,z}$ and $k_{t,z}$, respectively. The well known Fresnel's coefficients r_F , for the reflected wave, and T_F , for transmitted one are thereby obtained.

$$r_F = \frac{k_{i,z} - k_{t,z}}{k_{i,z} + k_{t,z}} = \frac{\alpha_i - \alpha'_i}{\alpha_i + \alpha'_i}; \quad R_F = |r_F|^2 \text{ for } \alpha_i \square 1 \quad (2.9)$$

$$t_F = \frac{2k_{i,z}}{k_{i,z} + k_{t,z}} = \frac{2\alpha_i}{\alpha_i + \alpha'_i}; \quad T_F = |t_F|^2 \text{ for } \alpha_i \square 1 \quad (2.10)$$

Where α'_i is the refracted beam angle that is defined by

$$\alpha'_i = \sqrt{\alpha_i^2 - \alpha_c^2} \quad (2.11)$$

For the incidence angles smaller than the critical angle, $\alpha_i < \alpha_c$, $k_{t,z}$ becomes imaginary and the transmitted electrical field is described by

$$E_t \sim e^{ik_{t,z}z} \sim e^{-k_z \sqrt{\alpha_i^2 - \alpha_c^2} z} = e^{-z/L_i} \quad (2.12)$$

The amplitude of the transmitted wave is exponentially dumped in the less dense medium and

its penetration depth L_i is defined when its amplitude reaches $1/e$ in eq. (2.13) [6].

$$L_i = \lambda/2\pi l_i \quad (2.13)$$

Where $l_i = 2^{-1/2} \left\{ (2\delta - \sin^2 \alpha_i) + [(\sin^2 \alpha_i - 2\delta)^2 + 4\beta^2]^{1/2} \right\}^{1/2}$, which has the asymptotic for $\alpha_i \rightarrow 0$ of $L_{i0} = \lambda/2\pi\alpha_c \approx 50 \text{ \AA}$ for Si at 8 keV.

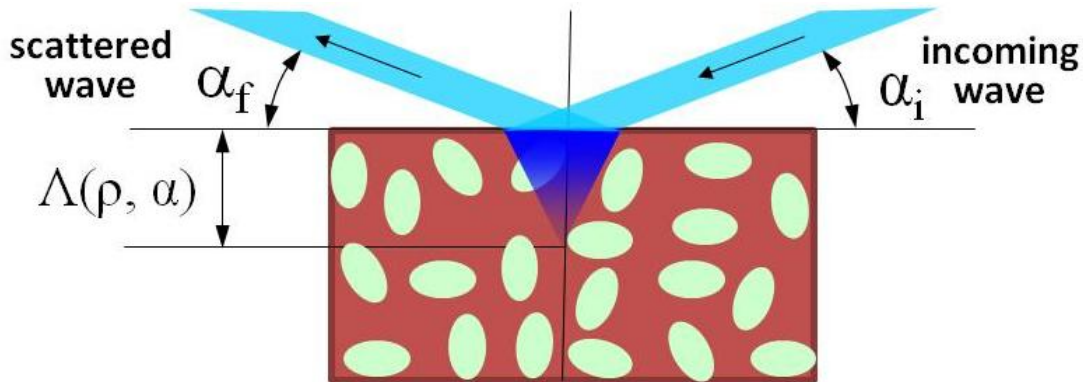


Figure 2.2 Tuning of penetration depth by tuning of angle of incidence, ultimately provides the excess to the different film thickness region under the condition $\alpha_{cf} \leq \alpha_i \leq \alpha_{cs}$.

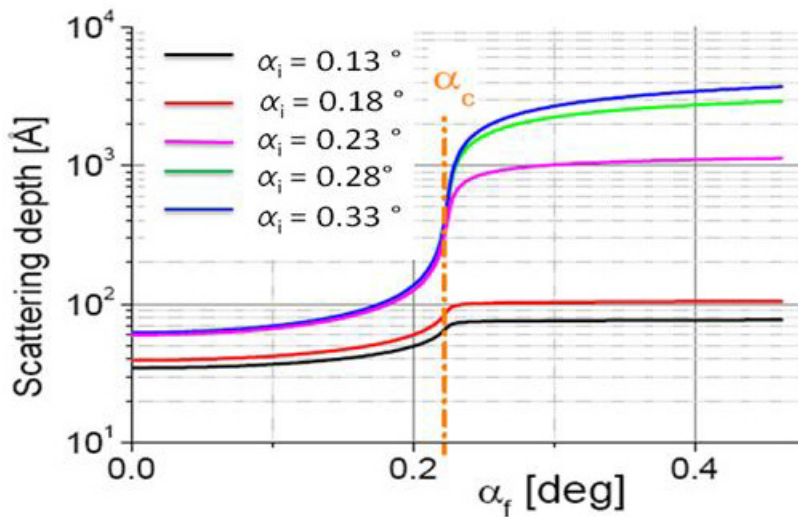


Figure 2.3 Calculated scattering depth Λ from eq. (2.13) for Si at 8 keV as a function of the incidence, α_i , and exit angles, α_f . The location of the critical angle is indicated at $\alpha_c = 0.22^\circ$.

Fig. 2.2 shows the tuning of depth at any particular length scale by changing the angle of incidence under any fixed geometry (GOD or GID) having $\alpha_{cf} \leq \alpha_i \leq \alpha_{cs}$. By keeping α_i under this condition the main advantage of the use of grazing incidence scattering method

is the enhancement of the experimental signal from the scatterers located in the near –surface layer. The scattering signal arising from the substrate is suppressed. The evanescent scattering enables to study the structural properties from layers of nanometric thickness, provided that a brilliant enough X-ray beam is available. This condition dictates the preferential application of the grazing-incidence scattering methods using synchrotron radiation. The penetration depth can be calculated utilizing eq. (2.13), for both indices i and f . As an example, Fig. 2.3 shows the results from the calculation of the scattering depth Λ for Si at 8 keV. A wide range of Λ from 45 to 4000 Å is accessible with an appropriate setting of α_i and α_f .

2.5. X-ray Reflectivity

X-ray reflectivity (XRR) technique is a powerful method for investigating monolithic film structures. XRR studies are highly sensitive to electron density gradients irrespective of the crystalline nature of the system investigated [4, 5]. It is also one of the few methods that, with great accuracy, allow one to not only extract information on the free surface and the interface(s), but also determine the mass density and the thickness of thin layers along the direction normal to the specimen surface. A typical XRR profile is shown in Fig. 2.4. This profile contains (i) a critical angle α_c whose position gives the average electron density, and (ii) interference fringes whose period gives the total thickness. The roughness values of the air/film and the film/substrate interfaces can be extracted from fitting analysis of the profile. However, if the interferences from several layers be at together, the situation is much more complicated.

2.5.1. Basic Principle

Both reflection and refraction are well known optical phenomena. For a condensed matter irradiated by X-rays of a given wavelength, its refractive index depends on the electron density of the volume irradiated. Hence, X-rays are reflected from and refracted at, interfaces between materials of differing electron density. X-ray reflectivity relies on the interference of X-rays reflected at different interfaces (Fig. 2.5), while X-ray diffraction results from the interference of X-rays diffracted from periodic lattice points. Determination of the mass density of the irradiated volume depends on the total external reflection phenomenon, which results from the fact that the refractive index of a condensed matter is less than unity.

2.5.2. Critical Angle

Since the refractive index, $n < 1$ (see eq. 2.8), the X-rays are refracted away from the normal to the surface when they enter the matter (the Snell's law). Consequently, there exists a critical angle of the incidence, α_c , below which total reflection of X-rays occurs. The critical angle of reflection is not well defined for the heavily absorbing materials, as it varies with β/δ ratio. If the absorption can be neglected; the critical angle α_c can be related to the dispersion term δ by $\alpha_c = \sqrt{2\delta}$ or $\alpha_c = (\lambda^2 r_e N / \pi)^{1/2}$, where r_e is classical electron radius and N is electron density per unit volume of material.

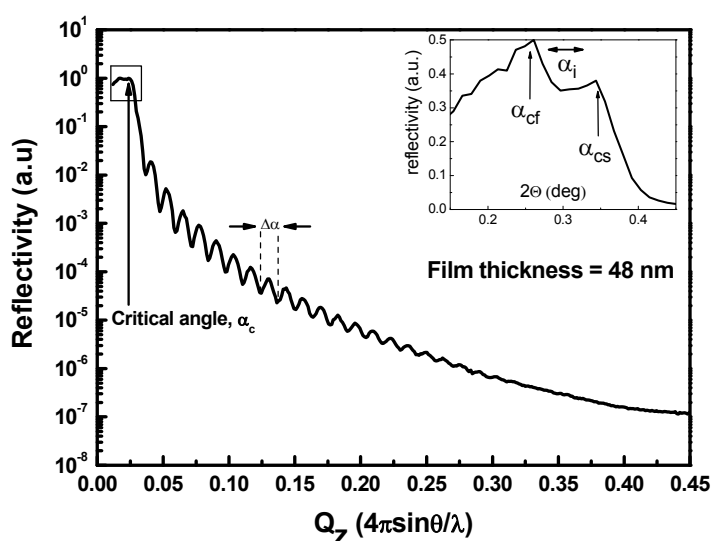


Figure 2.4 X-ray reflectivity curve of Poly(3-hexylthiophene) on HMDS/SiO₂ substrate.

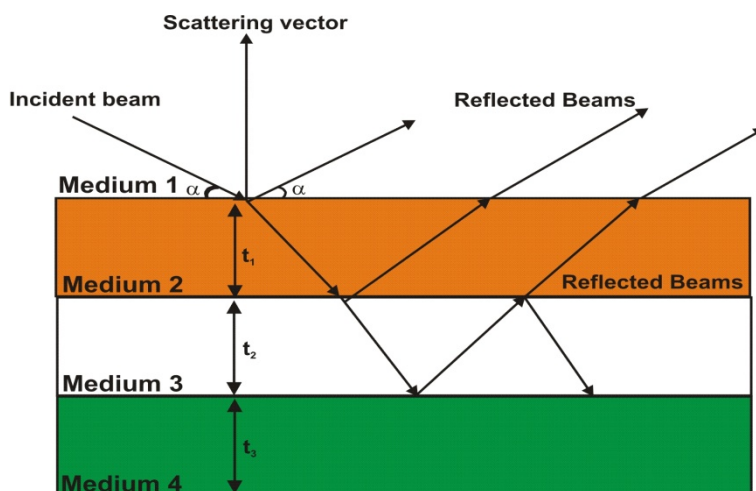


Figure 2.5 Refraction and reflection of a plane wave with amplitude E , incident upon the interface between vacuum and a material.

Here, the angle of incidence α , is defined as the angle between the incident ray and the surface. From the inset of Fig. 2.4, one can see clearly two critical angles, α_{cf} and α_{cs} . Where, the critical angle, α_{cf} corresponding to the air-film interfaces, whereas, the critical angle α_{cs} corresponding to film-substrate interface. In any case to penetrate the beam at any length scale of sample, the incidence angle must be under the condition where $-\alpha_{cf} < \alpha_i < \alpha_{cs}$. Depending on incidence energy of photons the values of all these critical angles mentioned here can vary from particular X-ray source to another source. Therefore it is necessary to convert all the data into common scale (Q space), independent from X-ray wavelength chosen.

2.5.3. A Quick Estimation of Thickness

For clearly identified Kiessig fringes, the film thickness t can be estimated quickly yet rather accurately from the fringe spacing $\Delta\alpha$ at high angles ($\geq 4\alpha_c$) by

$$t = \frac{\lambda}{2\Delta\alpha} = \frac{2\pi}{\Delta q} \quad (2.14)$$

Where $q_z = 4\pi\sin\theta/\lambda$. The advantage of eq. (2.14) lies in its simplicity as in many cases it is enough to estimate the film thickness.

2.6. X-ray Powder Diffraction

The powder method derives its name from the fact that the specimen is typically in the form of a microcrystalline powder (Fig. 2.6) but this is not always correct, even thin films can also behave like powder sample due to the presence of randomly orientated small crystallites. This is more favourable for organic materials where the structure is not as uniquely ordered like inorganic materials. Semi-crystalline polymers fall in this category, having amorphous as well as crystalline phases. Here, the small crystallites are embedded in the amorphous matrix. For a powder sample it is assumed that all grain orientations take place with the same probability, i.e. that the distribution function of grain orientation is isotropic. When a certain crystallographic lattice planes occur with a greater probability than others, this phenomenon is termed as preferred orientation or texture and it is a characteristic feature of thin polycrystalline films. A beam of X-rays passing through a sample of randomly-oriented micro crystals produces a pattern of rings on a distant screen (Fig. 2.6). Powder X-ray diffraction provides less information than single-crystal diffraction but it is useful for confirming the identity of a

solid material and determining the crystallinity. In the first case 2D detector can show concentric rings called as Debye-Scherrer rings, while for polycrystalline sample having preferred texture shows non-continuous rings, where the preferred direction is indicated by the presence of higher contrast in the ring.

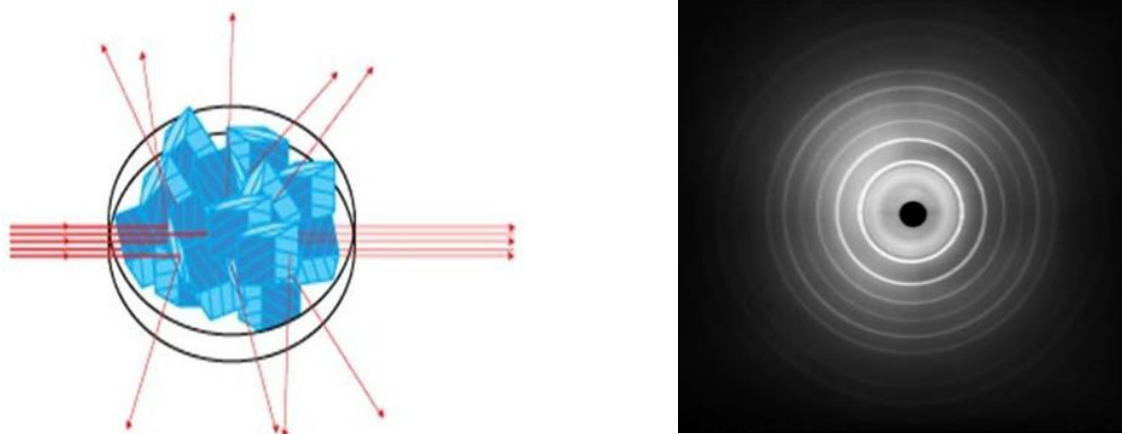


Figure 2.6 A typical NaCl powder sample (random orientation) and its corresponding X-ray diffraction pattern, concentric Debye-Scherrer rings. No intensity modulation around the rings.

For any set of planes with spacing $d(hkl)$, there are many crystals oriented so that their hkl -planes make the correct Bragg law angle α with the primary beam. Since the corrected oriented crystals have all orientations about the primary beam, the diffracted beams form a cone of half apex angle 2α or each planar spacing $d(hkl)$. Powder patterns are usually registered by film recording or by counter diffractometer.

2.7. Diffractometer Recording of Powder Samples

The typical powder geometry setup except of powder patterns by film recording has shown in Figure 2.7, which is also known as out-of-plane diffraction. Where the sample is a flat-faced briquet of powder. A monochromatic radiation diverges from the entrance slit, which in some cases is the line focus on the target. The diffracted radiation is selected by a narrow receiving slit before the detector. The appropriate filter is usually placed in the diffracted beam at the receiving slit. Since the sample face is maintained symmetrical with respect to the primary and diffracted beams, there is an approximate focussing condition. The radiation passed by the receiving slits is detected by the some type of counter, such as Geiger counter, gas-proportional counter or scintillation counter. During the measurements the counter turns at an angular velocity α and the sample turns at a velocity of $\alpha/2$ to maintain

focussing conditions and sample absorption geometry. A typical diffractogram recording of powder sample pattern of P3HT is shown by Figure 2.8. The receiving slit is usually very narrow compared to the width of an hkl-reflection, and the total peak contribution is recorded as the receiving slit scans across the diffracted beam. We are now interested in obtaining the full width at half maximum (FWHM) of diffracted peak, which is the essential tool for further powder data analysis such as those of Fig. 2.8.

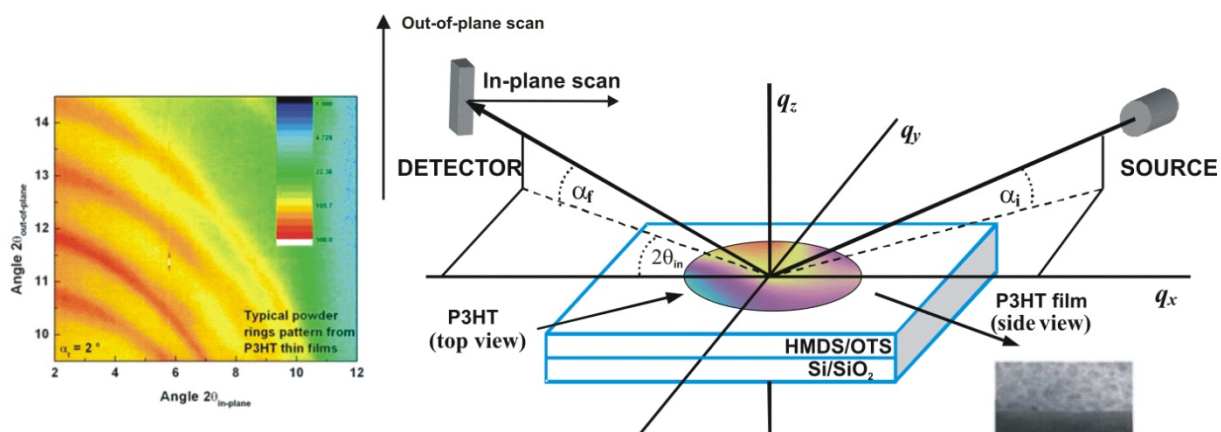


Figure 2.7 Sketch of the geometry of a typical GID setup for thin films with a PSD detector, on the left corresponding 2D powder pattern. Where α_i is the angle of incidence and α_f is the exit angle or the detector angle along the normal direction.

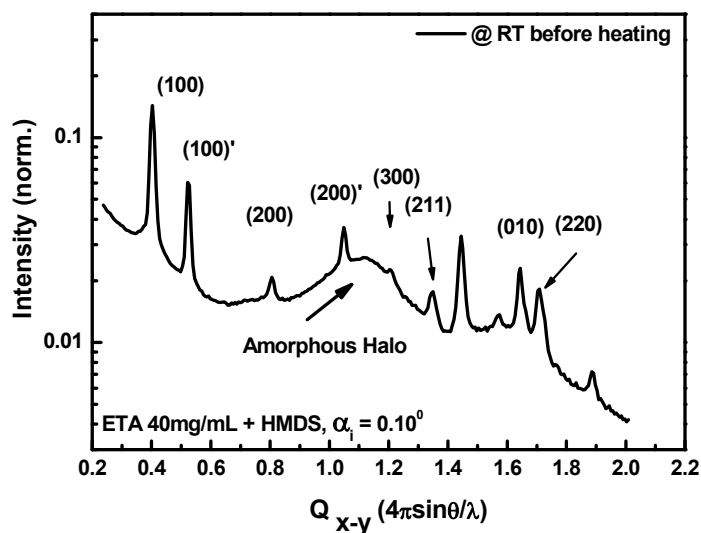


Figure 2.8 Out-of-plane (GIWAXS) diffraction pattern of thin polymer films of Poly(3-hexylthiophene). After taking line scan from corresponding 2D image, Figure 2.7.

For powder patterns recorded by a counter diffractometer, the handling of the systematic errors is not simple as it is for the powder camera. Even with a well built diffractometer having very accurately graduated scale, there are systematic errors such as

- a. Displacement of the sample surface from the centre of the instrument.
- b. Imperfect focusing resulting from a flat-faced sample.
- c. Penetration of the beam, so that diffraction takes place below the sample surface.
- d. A zero error in the setting of the 2θ scale.
- e. With chart recording, the peak displacement which results from use of too long a time constant.
- f. The axial divergence error.

2.8. Debye Scherrer Formula

The effect of various crystals imperfection on the diffraction pattern such as small crystallite size, strains, and faulting, since it is simplest kind of imperfection; we can start with consideration of the effect of small crystallites size. The intensity from a single small crystal can be written as

$$I = I_e F^2 \frac{\sin^2\left(\frac{\pi}{\lambda}\right)(\mathbf{k}-\mathbf{k}_0) \cdot N_1 \mathbf{a}_1}{\sin^2\left(\frac{\pi}{\lambda}\right)(\mathbf{k}-\mathbf{k}_0) \cdot \mathbf{a}_1} \times \frac{\sin^2\left(\frac{\pi}{\lambda}\right)(\mathbf{k}-\mathbf{k}_0) \cdot N_2 \mathbf{a}_2}{\sin^2\left(\frac{\pi}{\lambda}\right)(\mathbf{k}-\mathbf{k}_0) \cdot \mathbf{a}_2} \times \frac{\sin^2\left(\frac{\pi}{\lambda}\right)(\mathbf{k}-\mathbf{k}_0) \cdot N_3 \mathbf{a}_3}{\sin^2\left(\frac{\pi}{\lambda}\right)(\mathbf{k}-\mathbf{k}_0) \cdot \mathbf{a}_3} \quad (2.15)$$

Where N_1, N_2, N_3 are the numbers of unit cells along the $\mathbf{a}_1, \mathbf{a}_2, \mathbf{a}_3$ directions. In general the N_1, N_2, N_3 are such large numbers, that each of three quotients differs from zero only if the three Laue equations are closely satisfied, and hence the powder pattern reflections are sharp. For very small crystals where N_1, N_2, N_3 are small, the three quotients broaden, and the smaller the crystals the broader the powder pattern reflections. The peak breadth can be expressed in terms of the crystallites size, and hence a measurement of the peak breadth gives a simple method to determine crystallite sizes in the size range up to about 100 nm.

The first treatment of particle size broadening was due to Scherrer [14]. Although the derivation is of restricted generality, the Scherrer equation has considerable application, and it is of interest to reproduce the derivation. We assume the powder sample of small cubic crystals, all of the same size with $N_1 = N_2 = N_3 = N$. The crystals are assumed to be free from strains and faulting, so that the peak broadening is due to only to the small crystallites size. For convenience we now replace the powder sample by a single crystal which takes all orien-

tations. Let the unit vectors \mathbf{s} and \mathbf{s}_0 represent the exact Bragg law directions for the reflections hkl , so that

$$\mathbf{k} - \mathbf{k}_0 = \lambda(h\mathbf{b}_1 + kb_2 + l\mathbf{b}_3) \quad (2.16)$$

Now considering slightly different directions \mathbf{k}' and \mathbf{k}'_0 for the diffracted and primary beams, and relate them to $\mathbf{k} - \mathbf{k}_0$ by the small difference vector $\Delta\mathbf{k}$.

$$\mathbf{k}' - \mathbf{k}'_0 = \mathbf{k} - \mathbf{k}_0 + \Delta\mathbf{k} \quad (2.17)$$

Expressing eq. (2.15) in terms of the general directions $(\mathbf{k}' - \mathbf{k}'_0)$, we obtain

$$I = I_e F^2 \frac{\text{Sin}^2\left(\frac{\pi}{\lambda}\right) \Delta\mathbf{k} \cdot \mathbf{N}_1 \mathbf{a}_1}{\text{Sin}^2\left(\frac{\pi}{\lambda}\right) \Delta\mathbf{k} \cdot \mathbf{a}_1} \times \frac{\text{Sin}^2\left(\frac{\pi}{\lambda}\right) \Delta\mathbf{k} \cdot \mathbf{N}_2 \mathbf{a}_2}{\text{Sin}^2\left(\frac{\pi}{\lambda}\right) \Delta\mathbf{k} \cdot \mathbf{a}_2} \times \frac{\text{Sin}^2\left(\frac{\pi}{\lambda}\right) \Delta\mathbf{k} \cdot \mathbf{N}_3 \mathbf{a}_3}{\text{Sin}^2\left(\frac{\pi}{\lambda}\right) \Delta\mathbf{k} \cdot \mathbf{a}_3} \quad (2.18)$$

We now approximate each of the three quotients by a Gaussian function which has the same maximum ordinate and the same area

$$\frac{\text{Sin}^2 Nx}{\text{Sin}^2 x} \rightarrow N^2 e^{-\frac{(Nx)^2}{\pi}} \quad (2.19)$$

With this approximation, the intensity expression becomes

$$I = I_e F^2 N^6 e^{-\left(\frac{\pi}{\lambda^2}\right) N^2 \{(\Delta\mathbf{k} \cdot \mathbf{a}_1)^2 + (\Delta\mathbf{k} \cdot \mathbf{a}_2)^2 + (\Delta\mathbf{k} \cdot \mathbf{a}_3)^2\}} \quad (2.20)$$

Since the axes \mathbf{a}_1 , \mathbf{a}_2 , \mathbf{a}_3 are equal and orthogonal, the expression reduces to

$$I = I_e F^2 N^6 e^{-\left(\frac{\pi}{\lambda^2}\right) (N\mathbf{a})^2 (\Delta\mathbf{k})^2} \quad (2.21)$$

The exact Bragg law directions \mathbf{s} and \mathbf{k}_0 are shown by Figure 2.9a. We are interested in the intensity for a direction $\mathbf{k}' = \mathbf{k} + \Delta$ which makes a fixed angle with the Bragg law direction \mathbf{k} . maintaining \mathbf{k}' at a fixed angle from \mathbf{k} , we now wish to find the total contribution to the intensity when the crystal is rocked through the whole region where there is any contribution. Instead of rocking the crystal, it is simpler to hold the crystal and rock the $\mathbf{k}' - \mathbf{k}_0$ vector by adding the small vectors \mathbf{x} and \mathbf{y} which are in plane normal to $\mathbf{k} - \mathbf{k}_0$. The difference vector $\Delta\mathbf{k}$ which was introduced in eq. 2.17, becomes $\Delta\mathbf{k} = \mathbf{x} + \mathbf{y} + \Delta$, and the magnitude squared is given by

$$(\Delta\mathbf{k})^2 = (x - \Delta \sin \theta)^2 + y^2 + (\Delta \cos \theta)^2 \quad (2.22)$$

The intensity $I(\Delta)$ at a fixed departure Δ is proportional to the sum over all values of x and y , and since the contribution differs from zero only for small values of x and y , the integrals can be carried out from $-\infty$ to $+\infty$

$$I(\Delta) = KI_e F^2 N^6 e^{-\pi \left(\frac{Na}{\lambda}\right)^2 \Delta^2 \cos^2 \theta} \int_{-\infty}^{+\infty} e^{-\pi \left(\frac{Na}{\lambda}\right)^2 (x - \Delta \sin \theta)^2} dx \int_{-\infty}^{+\infty} e^{-\pi \left(\frac{Na}{\lambda}\right)^2 y^2} dy \quad (2.23)$$

By making the replacement $x' = x - \Delta \sin \theta$, $dx' = dx$, the two integrals are independent of Δ , and the values of the integrals can be combined in the new constant K'

$$I(\Delta) = K' e^{-\pi \left(\frac{Na}{\lambda}\right)^2 \Delta^2 \cos^2 \theta} \quad (2.24)$$

When $\Delta = 0$ we are at the center of the peak and $I(\Delta) = I_m$, where I_m is the peak maximum

$$I(\Delta) = I_m e^{-\pi \left(\frac{Na}{\lambda}\right)^2 \Delta^2 \cos^2 \theta} \quad (2.25)$$

Referring to Figure 2.9b, when $I(\Delta) = I_m/2$, the angle defined by Δ is half the angle $B(2\theta)$ which subtends the half maximum intensity width of the peak

$$\frac{1}{2} = e^{-\pi \left(\frac{Na}{\lambda}\right)^2 \left(\frac{B}{2}\right)^2 \cos^2 \theta} \quad (2.26)$$

The value of $B(2\theta)$ is then given by

$$B(2\theta) = \frac{2 \left[\frac{(\ln 2)}{\pi} \right]^{\frac{1}{2}} \lambda}{Na \cos \theta} \quad (2.27)$$

Letting $L = Na$ represent the cube edge dimension of the crystals, we obtain the Scherrer eq.

$$B(2\theta) = \frac{0.94 \lambda}{L \cos \theta} \quad (2.28)$$

In the Scherrer equation, $B(2\theta)$ is the full width in radians subtended by the half maximum intensity width of the powder pattern peak. In making the Gaussian approximation if we had matched the peak maximum and the half maximum peak width, the numeral constant would have been 0.89 instead of 0.94. The constant in the Scherrer equation is close to the unity, but the exact numerical value has little significance. Although the Scherrer equation was derived for a sample of cubic crystals, it is often applied to the peak breadths of noncubic materials.

For a given crystal dimension L , the peak breadth increases as $1/\cos \theta$, and hence particle size broadening becomes most pronounced at large values of θ . In general there is an additional instrumental broadening arising from effects such as slit width, wavelength, width of the $k\alpha_1$ $k\alpha_2$ lines, or the superposition of peaks due to $k\alpha_1$ and $k\alpha_2$ when the peaks are not resolved. The correction for instrumental broadening is very important, as in our case all of the measurements performed at Synchrotron radiation sources therefore due to much fine narrow parallel beam, the instrumental broadening has neglected from our calculations. At the same time as polymer material are not precisely crystalline rather than small crystallites are embedded in an amorphous matrixes, where the crystalline peaks are rather broad having average FWHM $\sim 0.5^\circ$, therefore one can also neglect the instrumental broadening from synchrotron source which is in order of 10^{-3} .

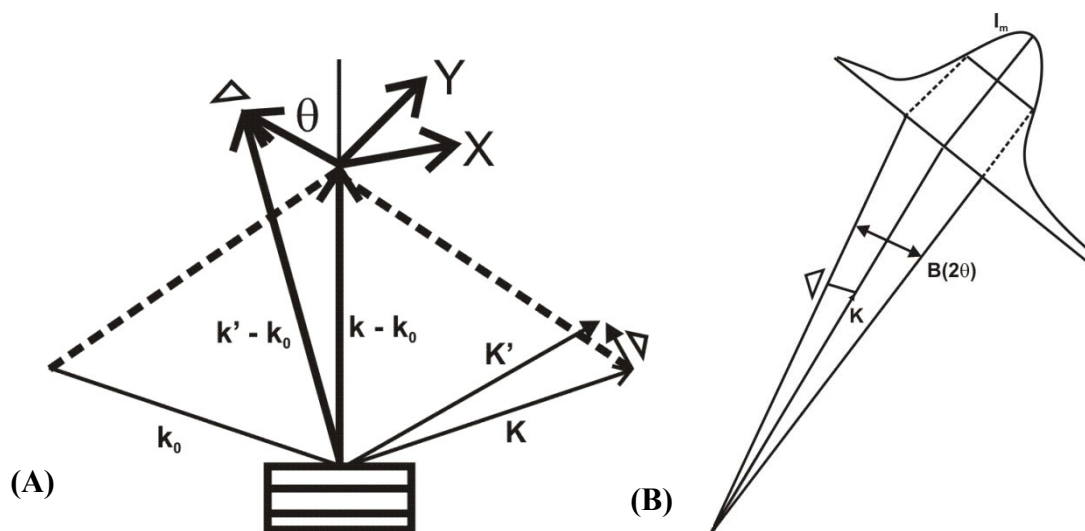


Figure 2.9 (A) Geometrical relations involved in the derivation of the Scherer equation. (B) The breadth $B(2\theta)$ representing the angle in radians on a 2θ scale which subtends the half maximum intensity breadth of a powder pattern peak [20].

2.9. Grazing Incidence Geometries

Under the grazing incidence geometry one can mostly explore the two primarily scans known as GOD (Grazing incidence out-of-plane diffraction) and GID (Grazing incidence diffraction). Both scans give the vital 2D surface structure information. The information obtained by means of GOD and GID is somehow complementary in a way that the two techniques probe different parts of the structure, according to different projections of the 2D surface structure. GID measurements probe the projection of the two-dimensional lattice onto the

xy-plane i.e. the lateral structure of the film, while the so-called 'GOD scans' provide information about the projection of the vertical structure present in the film. The complementary, reflectivity scans probe the electron density of a quasi two-dimensional system onto the z-axis, thus normal to the surface. In this case only a contrast in the electron density normal to the surface is necessary. Therefore, utilising all these 3 techniques give the complementary information rather than identical as shown in Figure 2.10.

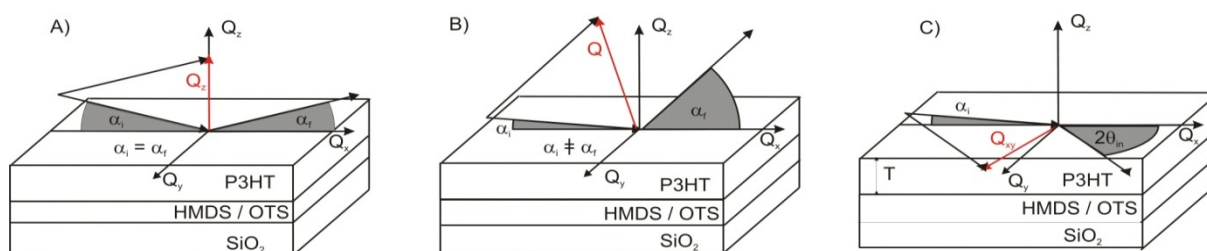


Figure 2.10 Different X-ray scattering geometries used for reflectivity, GOD and GID.

Going in further details, there are two more techniques exist, which are basically the part of GID technique, referred as GISAXS (Grazing Incidence Small Angle X-ray Scattering), it is a versatile tool for characterizing the shape of nanoscopic objects at surfaces, at buried interfaces, or in thin films. GISAXS combines features from Small-Angle X-ray Scattering (the mesoscopic length scale, incident beam definition by multiple slits, area detector) and diffuse X-ray Reflectivity (the scattering geometry and sample goniometer). Whereas, GIWAXS (Grazing Incidence Wide-Angle X-ray Scattering) or GOD technique also provides information about lateral and normal ordering at the surface or inside a thin film. In the GIWAXS regime with scattering angles larger than $\sim 5^\circ$, whereas the angle of incidence must be under grazing incidence condition.

2.10. Grazing incidence Out-of-Plane Diffraction (GOD) Scans

The basis of the surface sensitive X-ray scattering and diffraction techniques, grazing incidence out-of-plane diffraction (GOD) or GIWAXS and grazing incidence X-ray diffraction (GID), are discussed here. Grazing incidence diffraction based on the phenomenon that at incident angles below the critical angle for total external reflection an evanescent wave is established, which is travelling parallel to the surface and whose penetration into the bulk is exponentially damped. Below the critical angle the $1/e$ penetration depth is typically of the order of 50 \AA [19] so that bulk scattering is suppressed in contrast to scattering from the surface.

For the GOD scans (Fig. 2.10b), the surface of the sample is located in the horizontal xy -plane, normal to the z -direction. The incident wave with wave-vector k_i impinges on the sample surface under an angle α_i smaller than the critical angle. For the investigation of the structure of a quasi two-dimensional powder, the incident direction is fixed with respect to the sample by fixing the angle of incidence α_i . The scattered wave with a wave-vector k_f is detected under an exit angle α_f normal to the sample surface and under an in-plane scattering angle $2\theta_{in} = 0^\circ$ (this is ideal but not necessary condition). By moving the detector along the z direction α_f scan can be recorded. By changing the angle of incidence α_i one can control the penetrating depth of the sample, by doing this one can get the information about the bulk surface or the top surface within the condition $\alpha_{cf} \leq \alpha_i \leq \alpha_{cs}$. Where

- α_{cf} = Critical angle of film
 α_i = Incidence angle
 α_{cs} = Critical angle of substrate

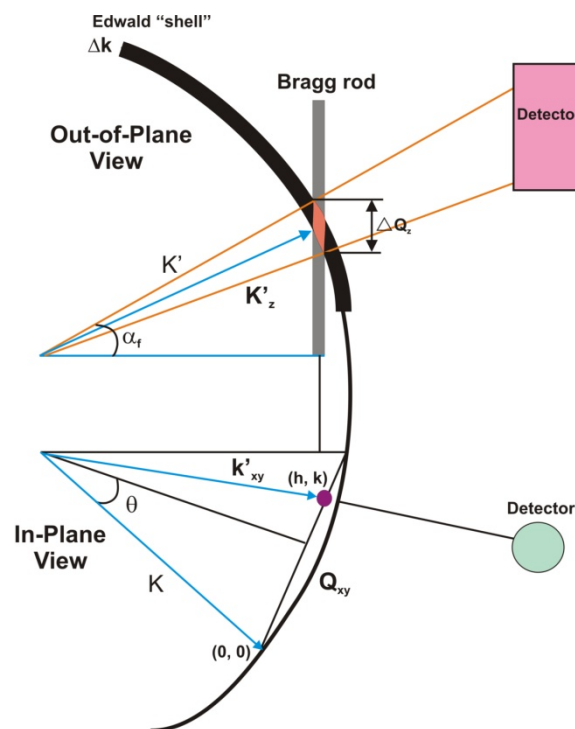


Figure 2.11 The accessible Q space area with specular, longitudinal-and rocking scans.

From the above scheme shown in Fig. 2.11, the wave vector transfer is given as

$$\mathbf{q} = q_x + q_y + q_z = \mathbf{K}_i - \mathbf{K}_f \quad (2.29)$$

With the boundary condition $k_i = k_f$ for elastic scattering. The components q_x and q_y are combined to the lateral wave-vector transfer q_{xy} . The following components of the wave-vector transfer for the given scattering geometry can be calculated as

$$Q_z = k (\sin \alpha_i - \sin \alpha_f) = 4 \times \pi \times \sin \alpha_i / \lambda \quad (2.30)$$

(For reflectivity measurements)

$$Q = k (\sin \alpha_i - \sin \alpha_f) \cong 2 \times \pi \times \sin (\alpha_f) / \lambda \quad (2.31)$$

Where $\alpha_i \neq \alpha_f$ for out-of-plane scan

$$Q_{x-y} \approx k \sqrt{1 + \cos^2 \alpha_f - 2 \cos \alpha_f \cos 2\theta} \approx 2k \sin \frac{2\theta_{in}}{2} \quad (2.32)$$

Where $\alpha_i \ll 1, f \text{ or } 1$, for in-plane scans

By utilising the following, GOD geometry and the chemical structure of the particular sample, one can able to comment about the presence of the number of lamella planes lying along the parallel to the substrate and subsequently inter-planar distances 'd'.

To comment about bulk and extreme surface properties, one has to perform the OOP scans for different set of α_i^s . By keeping the angle of incidence $\alpha_i < \alpha_c$, it is possible to limit the penetration depth of X-rays into the sample, thus reducing the background scattering from the substrate or the bulk of the polymer.

It directly gives you excess to the information about the set of bulk or top surface properties depending on the length scale of the structure of interest. One has to note here that by increasing the α_i , the exposed volume within the sample also increases which as expected should provide you higher scattering signals, the deviation from this behaviour can give you direct hint about the surface/interface level properties.

2.11. Grazing Incidence Diffraction (GID) Scans

The grazing incidence geometry (Fig 2.10c), on the other hand also surface selective as like GOD, i.e. largely avoids scattering from the substrate. If the incident angle is small enough (depending on the substrate electron density and the X-ray energy) an evanescent wave penetrates into and scatters from it. The X-ray intensity is therefore highest at the surface as desired. It is possible to increase the surface selectivity further by reducing the angle of incident and thus causing the evanescent wave to damp out faster.

For an in-plane scan (Fig. 2.10c) the angle of incidence α_i^s still keep under the conditions $\alpha_{cf} \leq \alpha_i \leq \alpha_{cs}$, and the scattering angle $2\theta_{in}$ is varied by varying the detector horizontally. The in-plane scattered intensity is then collected by detector over the particular given range. In general $\alpha_i = \alpha_f$ but by varying the α_f one can access the individual rings present in powder diffraction. Under GID geometry, one is cutting the planes lying normal to substrate i.e. can provide the lateral structure distribution of any sample. The diffracted beam has good peak-to-background ratios, which are relatively free from interference from under layer(s) and the substrate.

The scattering vector of in-plane diffraction is always parallel to the film surface, and the direction of the scattering vector moves horizontally with the scanning $\sim 2\theta_m$. This makes possible a direct measurement of lateral crystal-structure parameters including lattice constants, crystallite sizes, film orientation, long-range ordering, etc. The in-plane scattering vector can be written as eq. (2.32). By varying the angle of incidence of the X-ray beam around the critical angle for total reflection of the film, the penetration depth can be tuned to allow a direct comparison of molecular ordering in the surface and bulk of the film.

Parallel to it, this technique has some limitations. The first is that it works well only with very smooth surfaces, and not all surfaces can be made sufficiently smooth. If the critical angle is 0.1° , for example, any long-range or short-range variation in the surface normal of the order of 0.1° will move large parts of the surface out of the total reflection condition.

Second, at grazing angles, most of the incoming X-ray beam is wasted. Assuming an incident angle of 0.1° and a surface dimension $1\text{ cm} \times 1\text{ cm}$, only a $2\ \mu\text{m}$ slice of the X-ray beam will fall on the surface; the rest either hits the side or passes over the sample. Unfortunately focusing, when possible, helps but also hurts; if the incident beam is converging to a focus at the sample, it contains a range of incident directions and therefore not all the photons will land below the critical angle for total reflection. The need is therefore for a beam that is intrinsically both compact and collimated. This is provided by synchrotron sources. Even with synchrotron radiation, further focusing is useful, but since this is done with large source-to-mirror and mirror-to-focus distances (not practical in the laboratory), the beam can be focused without significantly worsening the divergence.

Therefore, the combination of the results from GOD, GID and SR provide a complete understanding of the structure. The upcoming chapters will give you more insight of these techniques and their applications based on our polymer samples.

2.12. Distorted Wave Born Approximation for Grazing Incidence Scattering

The diffraction theory for small crystals [8] is inadequate to describe the diffraction pattern produced by an X-ray beam striking the surface of a crystal with an angle of incidence in the order of the critical angle for total external reflection. The reason is that it relies on the first Born approximation, i.e. no multiple scattering phenomena considered. The demand for a theoretical simple model for the description of grazing incidence scattering phenomena was satisfied by Vineyard [9] with the Distorted Wave Born Approximation (DWBA) in 1982. Sinha et al. [10] completed the DWBA theory and its applications to near-surface structure investigation are described in Ref. [4, 6, 11-13].

The DWBA is a combination of surface scattering and kinematical treatment of the scattering process. The refraction by smooth interfaces is exactly taken into account, while the scattering at lateral inhomogeneities of the crystal is treated kinematically, i.e. without including the multiple scattering effects [14].

In the conventional theory of the diffraction, a sample containing near-surface scatterers is assumed to be illuminated by a single plane wave, $E_i = E_i e^{ik_i r}$ and interact with it in a dynamical scattering process to result in an out-going wave, $E_f = E_f e^{ik_f r}$. In the DWBA, the real scattering sample is first replaced by a simpler distribution of material, the scattering from which can be calculated exactly (e.g. a semi-infinite crystal). The electric field thereby created, namely the evanescent ('distorted') wave, $T_i = T_i e^{ik'_i r}$, is used to illuminate each element of the real scatterer. The interaction of T_i with the sample is treated in the kinematical approximation, resulting in $T_f = T_f e^{ik'_f r}$. The interaction of T_f with the model system on its outgoing path originates E_f .

In the previous section, it was explained how the incoming beam E_i experiences the transmissivity of the interface between the vacuum and the matter. The formation of an evanescent wave T_i is the first step of application of the DWBA. Following Helmholtz's reciprocity principle (6), 'if the source and the point of observation are interchanged the same amplitude would result', the same process holds for the beam exiting the sample and creating T_f . The scattered intensity, $I(Q')$, results then in eq. (2.33) [14].

$$I(Q') \propto I_0 |T_{i,z}|^2 |T_{f,z}|^2 k(Q') \quad (2.33)$$

Where the incoming transmitted amplitude is $T_{i,z} = \frac{2k_{i,z}}{k_{i,z}+k'_{i,z}}$ and the existing transmitted amplitude is $T_{f,z} = \frac{2k_{f,z}}{k_{f,z}+k'_{f,z}}$. The z-component of the wave vectors of the transmitted beams are defined as $k_{i,z} = k \sin \alpha_i$, $k_{f,z} = k \sin \alpha_f$, $k'_{i,z} = nk \sin \alpha'_i = k(n^2 - \cos^2 \alpha_i)^{1/2}$ and $k'_{f,z} = nk \sin \alpha'_f = k(n^2 - \cos^2 \alpha_f)^{1/2}$. $k(\mathbf{Q}')$ is the kinematic structure factor of the scatterer with \mathbf{Q}' denoting the complex scattering vector in the crystal, $\mathbf{Q}' = \mathbf{k}'_f - \mathbf{k}'_i$.

2.13. Background Subtraction and Diffuse Scattering

Fluctuations are the rule in soft-condensed matter systems, and they are not restricted to fluctuations in the positional order in ordered systems like mesophases: surfaces and interfaces may strongly fluctuate, and there are also large-scale density fluctuations in compressible disordered systems. Because these fluctuations are not related to any discontinuous symmetry, they do not give rise to scattering close to a singularity, and scattering is centered at the origin of reciprocal space. Some of the cases are (1) surface and interface fluctuations, a single rough surface separating two homogeneous media (the upper medium being, for example, a vacuum), (2) Density fluctuations and inhomogeneities in noncrystalline media. The common fluctuations of this kind are density fluctuations in bulk phases.

Under both GID and GOD scans often it is necessary to subtract the background due to diffuse scattering in the bulk and at the surface, in order to determine the 'true' specular signal. This diffuse scattering more dominate or play an important role especially when the material is semicrystalline, where both ordered and disordered phases dominating. Particularly in the case where one has to separately compare the crystalline scattering with amorphous scattering, in order to do this first, one needs to distinguish between the amorphous halo peaks and crystalline peaks followed by their correct angular positions, later the amorphous part can be separate after knowing the their angular positions . The ratio of crystalline to amorphous halo peaks area will ultimately give the degree of crystallinity.

Before to get the quantitative value of these two phases, it is necessary to subtract the other background signals by means of any sources, some of them are

- a. Substrate scattering
- b. Scattering of any unnecessary sources or instrumental scattering (example – scattering from slits or any beamline components)
- c. Air scattering

In order to subtract this from GID or GOD scans, one needs to have the separate GID and GOD scans of substrate as well as to substrate air and instrumental scattering one should perform the individual scans without sample under same physical conditions.

In fact, such measurements do not yield satisfactory results because bulk scattering dramatically increases when the angle of incidence becomes larger than the critical angle for total external reflection, which is unavoidable in such scans. Indeed, the penetration length becomes in the order of a μm , whereas it is of the order of a nm if either $\alpha_{\text{cf}} < \alpha_i < \alpha_{\text{cs}}$. In practice, it is therefore necessary to fix the angle of incidence below the grazing angle for total external reflection α_{cs} . Under this constraint, it is possible to measure the scattered intensity by scanning either in the plane of incidence or in the horizontal sample plane.

In the GOD case, where q_z is varied mainly, the scans are therefore sensitive to the normal structure (because of the q_z variation). This kind of measurements is considered whenever one is interested in the determination of the normal structure of thin films. It is indeed a valuable alternative to reflectivity experiments when using synchrotron radiation. Its main advantage over reflectivity is a reduced background because the grazing angle of incidence is fixed below the critical angle for total external reflection.

In the GID case, where the scattering is almost limited to horizontal sample plane, by fixing the q_z very small, will provide you the surface roughness at large wave vectors. Which directly yields a signal proportional to the roughness spectrum should be preferred.

Therefore it is equally important to consider the diffuse scattering to comment precisely. Under our measurements we have considered the diffuse scattering for GID and GOD scans and all the additional scatterings from substrate, air and beamline component, wherever it needs we have subtracted it. The diffuse scattering from the disordered part of material is present in all scans as a big halo curve. This in itself indicates that how much these semicrystalline materials are regulated by such disordered parts.

2.14. Coherence Effects

The high degree of coherence of the light produced by the brilliant third-generation synchrotron radiation sources might affect our description of the scattered intensity as the convolution of the scattering cross-section with a resolution function. The appropriate frame to discuss effects of partial coherence is the Fresnel diffraction theory, and the effects of partial coherence and of the validity of the far-field approximation (Fraunhofer diffraction) must be discussed together. A general discussion can be found in [16].

2.15. Synchrotron Radiation Sources – Fundamental Operation

Synchrotron radiation provides the user with a continuous spectrum of radiation from the infrared to the hard X-ray region, with intensity at least ten orders of magnitude higher than can be achieved with a conventional laboratory based rotating anode generator (Fig. 2.12). Other important properties that appeal to different experiments performed within the user community are its high degree of polarization, pulsed time structure and low divergence. The main part of a synchrotron is called a storage ring, in this ring electrons are kept orbiting at speeds close to the speed of light. These electrons produce extremely intense X-rays. A good overview of the properties of synchrotron radiation to X-ray diffraction can be found in [4, 15, 17].

Electromagnetic radiation is emitted when charged particles, usually electrons or positrons, moving close to the speed of light are forced to change direction under the application of a magnetic field: this is the basic operating principle of a synchrotron (Fig. 2.13). The electromagnetic radiation is emitted in a cone in the forward direction, at a tangent to the orbit of the charged particles. In 1897, Larmor obtained – starting from the Maxwell equation – the power distribution of the light emitted by a (nonrelativistic) accelerated charge. Calling the element of solid angle, it is

$$\frac{dP}{d\Omega} = \frac{e^2}{4\pi c} |n \times \{n \times \dot{\beta}\}|^2 \quad (2.34)$$

where e is the charge of the particle, n is the normal to the surface element and β is the velocity vector in unit of the speed of light [16]. The energy ε_e of an electron at speed v is

$$\varepsilon_e = mc^2 / \sqrt{1 - \left(\frac{v}{c}\right)^2} \quad (2.35)$$

It is convenient to use the electron energy γ , measured in units of its rest mass energy, $\gamma \equiv \varepsilon_e/mc^2$, and the speed β_e , measured in units of the velocity of light, $\beta_e = v/c$. The formula above then reads

$$\gamma \equiv \frac{1}{\sqrt{1 - \beta_e^2}} \quad (2.36)$$

The electron energy in a typical X-ray synchrotron storage ring is 5 GeV. The rest mass of an electron is 0.511 MeV, so γ is of order 10^4 . We can therefore expand the eq. (2.36) to obtain

$$\beta_e = \left[1 - \frac{1}{\gamma^2}\right]^{0.5} \cong 1 - \frac{1}{2\gamma^2} \quad (2.37)$$

It can be shown that the emission is confined within a cone of semi-aperture $1/\gamma$ centered around $\vec{\beta}$. For the ESRF storage ring $\gamma \sim 12000$; this means that the divergence of the single electron emission is $\sim 80 \mu\text{rad}$. For further details on the synchrotron light the reader can use [17, 18].

Synchrotron light produced in this manner possesses a number of unique properties stated as follows

- **High brightness:** synchrotron light is extremely intense; it is hundreds of thousands of times more intense than that from conventional X-ray tubes. In addition synchrotron light is highly collimated.
- **Wide energy spectrum:** synchrotron light is emitted with energies ranging from infra-red light to hard, energetic, short wavelength X-rays.
- **Tunable:** through sophisticated monochromators and insertion devices it is possible to obtain an intense beam at any desired wavelength.
- **Pulsed:** electromagnetic pulses may be generated with duration typically less than a nano-second (one billionth of a second).
- To image or detect fine structure, the wavelength of the illuminating radiation must be of the same order as the structure. Synchrotron light is able to span the electromagnetic spectrum across almost all fields of scientific interest, from life-size imaging down to nanoscale, molecular and atomic length scales.

State of the art (third generation) synchrotrons aim is to optimize the intensity of the emitted light that can be obtained from insertion devices. In particular, careful attention is given to the positioning of the straight sections that accommodate the insertion devices. In general synchrotron, it is planned to place the magnetic components of the undulators inside the vacuum of the storage ring.

This will allow very close spacing of the magnets and extremely high beam intensities. For the wiggler devices, conventional magnets may be used, but they will be wound with superconducting wire, enabling extremely high intensities to be generated with very high specificity with respect to frequency (or equivalently, wavelength). The ESRF Synchrotron will, consequently, be of an advanced third generation design comprising bending magnets, wig-

glers and undulators, enabling a wide range of experiments to be conducted in a one single facility.

Many remarkable properties characterise the synchrotron radiation, some of them are energy tuneability, high photon flux, low-X-ray beam divergence, coherence and pulsed emission [5]. In order to apply grazing incidence X-ray scattering techniques, the most important characteristic of the synchrotron radiation is its brilliance. The brilliance is defined as

$$\text{Brilliance} = \frac{\text{Photons/second}}{\text{mrad}^2(0.1\% \text{bandwidth})} \quad (2.38)$$

It depends on the number of photons emitted per second and the collimation of the beam, expressed in mrad, both for the horizontal and the vertical directions.

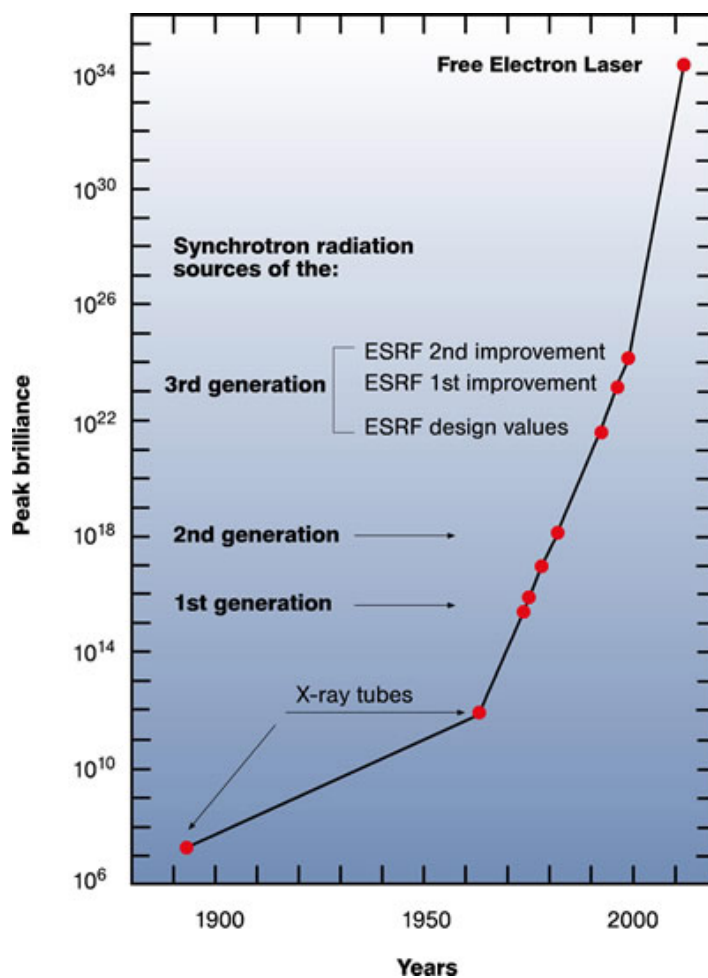


Figure 2.12 The development of X-ray radiation sources demonstrates how dramatically the brilliance has increased since the discovery that particle accelerators can produce synchrotron radiation. The development of an X-ray laser at DESY continues this upwards trend and opens up previously un-dreamed-of possibilities for research.(Source: ESRF - European Synchrotron Radiation Facility in Grenoble).

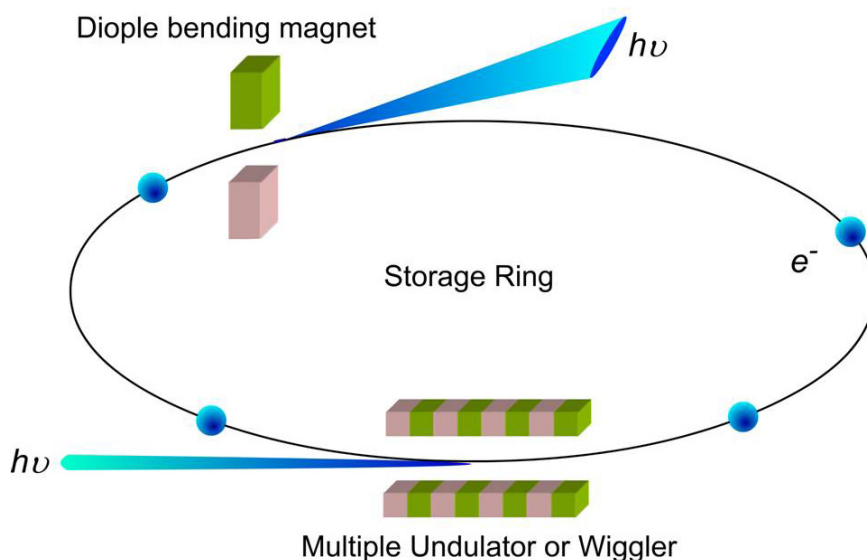


Figure 2.13 A schematic diagram of a synchrotron radiation accelerator.

Moreover, the area of the X-ray source is considered, which is expressed in mm^2 . The spectral distribution of the source is taken into account by defining the photon energy with a determined bandwidth, i.e. $\Delta E/E = 0.1\%$. The parameter of the brilliance can be used to compare the different X-ray source. The brilliance is a function of photon energy and its value, in a third generation undulator, is about 10 orders of magnitude higher than for a conventional rotating anode [5, 19]. For grazing incidence X-ray scattering experiment, the high brilliance of synchrotron radiation is needed in order to obtain sufficiently high signal-to-background ratio.

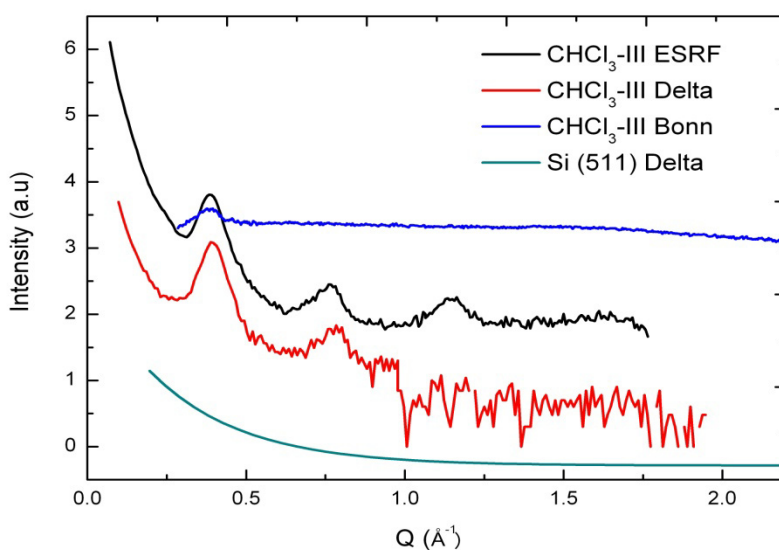


Figure 2.14 Comparison of different X-ray diffraction scans obtained from synchrotron sources (ESRF and Delta) and from rotating Cu anode tube.

2.16. Advantage of Synchrotron Source

Fig. 2.14 clearly shows the advantages of synchrotron sources compared to typical lab source. At the same time two different synchrotron source datas (ESRF and Delta) also compared. Due to poor signal to background ratio and also due to low flux (at least ten orders of magnitude), one can just feel the presence of (100) peak with coming straight line at higher angular position from the X-ray tube. While this trend is tremendously improved with ESRF third generation synchrotron source, while using Delta, where flux is at least 3 orders of magnitude lower than ESRF, after the 1st order peak, the background noise as well as diffuse scattering is dominated over crystalline peak, therefore the crystalline peak submerged and gives only noise data.

2.17. References

- [1]. W. Röntgen, "On a new kind of rays," *Nature*, vol. 53, p. 274, 1896.
- [2]. W. C. Roentgen. *Über eine neue art von strahlen. vorläufige mittheilung.* *Sber. Phys.-Med. Ges. Würzb.*, 137:132, 141, 1895.
- [3]. A. Einstein. *Lassen sich brechungsexponenten der körper für roentgenstrahlen experimentell ermitteln* *Verh. Dtsch. Phys. Ges.*, 20:86-87, 1918.
- [4]. U. Pietsch, V. Holy, and T. Baumbach, *High Resolution X-ray Scattering from thin films and multilayers*, Springer Tracts in Modern Physics, Vol. 149, Springer-Verlag, Berlin, 1999.
- [5]. J. Als-Nielsen, D. McMorrow, *Elements of X-Ray Physics*, J. Wiley & Sons, Inc., New York, 2001.
- [6]. H. Dosch, *Critical Phenomena at Surfaces and Interfaces: Evanescent X-Ray and Neutron Scattering*, Springer, Berlin, 1992.
- [7]. W. H. Zachariasen, *Theory of X-ray diffraction in Crystals*, Wiley, New York, 1945.
- [8]. B. E. Warren, *X-ray diffraction*, Dover Publ., New York, 1990.
- [9]. G. H. Vineyard, *Phys. Rev. B*, 26, 4146, 1982.
- [10]. S. K. Sinha, E. B. Sirota, S. Garoff, H. B. Stanley, *Phys. Rev. B*, 38, 2297, 1988.
- [11]. U. Pietsch, *Curr. Sci.*, 78, 1484, 2000.
- [12]. I. K. Robinson, D. J. Tweet, *Rep. Prog. Phys.*, 55, 599, 1992.
- [13]. C. Lamberti, *Surf. Sci. Rep.*, 53, 1, 2004.
- [14]. M. Tolan, *X-Ray Scattering from Soft-Matter and Thin Films-Materials Science and Basic Research*, Springer, Berlin, 1999.
- [15]. T. Tuomi, N. Naukkarinen, and P. Rabe, "Use of synchrotron radiation in X-ray diffraction topography," *Physica Status Solidi (a)*, vol. 25, pp. 93–106, 1974.
- [16]. Sinha S K, Tolan M., and Gibaud A, *Effects of partial coherence on the scattering of X-rays by matter* *Phys.Rev. B* 57, 2740–58, 1998.
- [17]. J. D. Jackson, *Classical Electrodynamics*, 3rd edition. John Wiley & Sons, New York London, 1999.
- [18]. Baruchel, J., Hodeau, J., Lehmann, M., Regnard, J. & Schlenker, C., eds., *Neutron and Synchrotron Radiation for condensed matter studies, Vol I*. Les Editions de Physique, Springer-Verlag, 1993.

- [19]. P. Dutta., Grazing incidence X-ray diffraction, Current Science, 78(12):1478-1483, 2000.
- [20]. B. E. Warren, X-ray diffraction, Dover Publications, INC., New York, 1990.

Chapter 3

Methods and Experimental Details

As all the measurements were performed under different beamlines located at various synchrotron sources, namely ID10B (ESRF, Grenoble, France), BW2 (Hasylab, Hamburg, Germany), BL9 (Delta, Dortmund, Germany), where we have setup for powder diffraction setup for polymer thin film studies. Therefore explanation of main features of all the beam lines used for this work is out of scope of this thesis. Even though, a general setup and features of ID 10B beam line at ESRF has explained in this chapter. In general, the set-up of grazing incidence experiments will be explained in details due to its importance for the use of surface sensitive X-ray scattering techniques. To achieve the meaningful results from any scan in the reciprocal space the alignment of the setup is crucial.

3.1. ID 10B Beamline at ESRF

The ESRF is a “third generation” synchrotron radiation source. Its storage ring for the electron beam has a circumference of 844 m and more than 40 beamlines. Details on the structure of the ESRF can be found in [1] Figure 3.1a shows this large-scale facility, where the main components of the ESRF have been indicated, such as linear accelerator, the booster synchrotron, the storage ring and a beamlines.

The beamline ID10B is hosted at the European Synchrotron Research Facility (ESRF) at Grenoble, France. The beamline provides synchrotron radiation by an undulator device [2]. The energy can be tuned between 8 keV to 22 keV. Different energies were used for the experiments discussed in this work were set to 13.3 keV and 15.3 keV in order to reduce absorption as well as the air-scattering. The layout of the beamline is schematically shown in Fig. 3.1b.

The beam is guided to the experimental hutch that is equipped with a Huber goniometer. The goniometer provides the possibility to mount the sample in horizontal or vertical orientation with respect to the ground. The orientation of the sample surface in respect of the ground has chosen for measurements. Therefore, the incoming beam was polarized within the plane of sample surface. Additionally, the primary beam was bended by 0.18° with respect of the rotation axis of the goniometer that gives the possibility to rotate the sample without changing the sample surface. The beam width was 300 mm in the horizontal direction and 100 mm in the vertical direction. Photographs of the goniometer are shown in Figure 3.2 and 3.3.

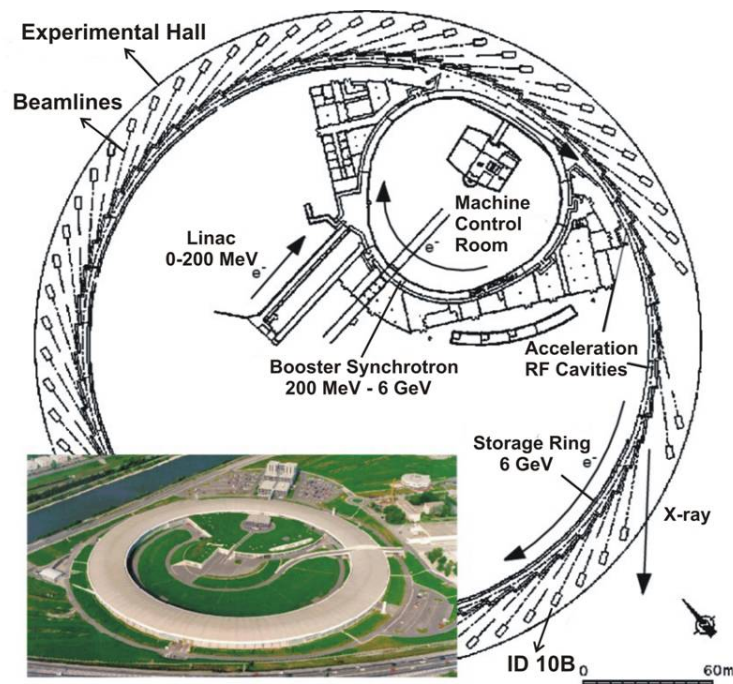


Figure 3.1a The European Synchrotron Radiation Facility, Grenoble, France. The main components of this large-scale facility have been highlighted. Linear accelerator, where the electrons are produced and first accelerated, the booster synchrotron, where the electrons are accelerated to relativistic speeds before being injected into the storage ring. Finally, the location of the beamline ID 10B. Adapted from ESRF [1].

The photograph in Fig. 3.2 shows the main components of the experimental setup. The incoming beam is indicated by the black arrow on the left hand side. The primary beam side is guided in a vacuum tube to minimize air scattering. Additionally motorized slit, automatic beam attenuator and the primary beam monitor are mounted at the primary side. With the slits the size of the beam can be adjusted to guaranty that the beam strikes the sample completely. This reduces disturbing scattering e.g. from the sample holder. The divergence of the primary beam will not be varied since the beam travel perfectly parallel. The automatic beam attenuator is made of different thick aluminium foils that fixed on circularly moving disk. The attenuator is required to prevent the detectors from damage due to the high flux of beam. The monitor is a detector that allows the correction of the intensities since the primary beam varies strongly with time.

In the middle of the goniometer the sample is mounted within a Anton Paar dome (DHS 900 Heating stage). These domes are evacuated, that reduces the sample degradation due to radicals formed in air by the intense X-ray beam. Next to the sample on the left side the detector arm is located. On the detector arm one can align the any detector depends on choice and information. Based on our need we have utilised CCD as well as positional sensitive detector (PSD). In front of the detector there are motorized slits to reduce the divergence of the

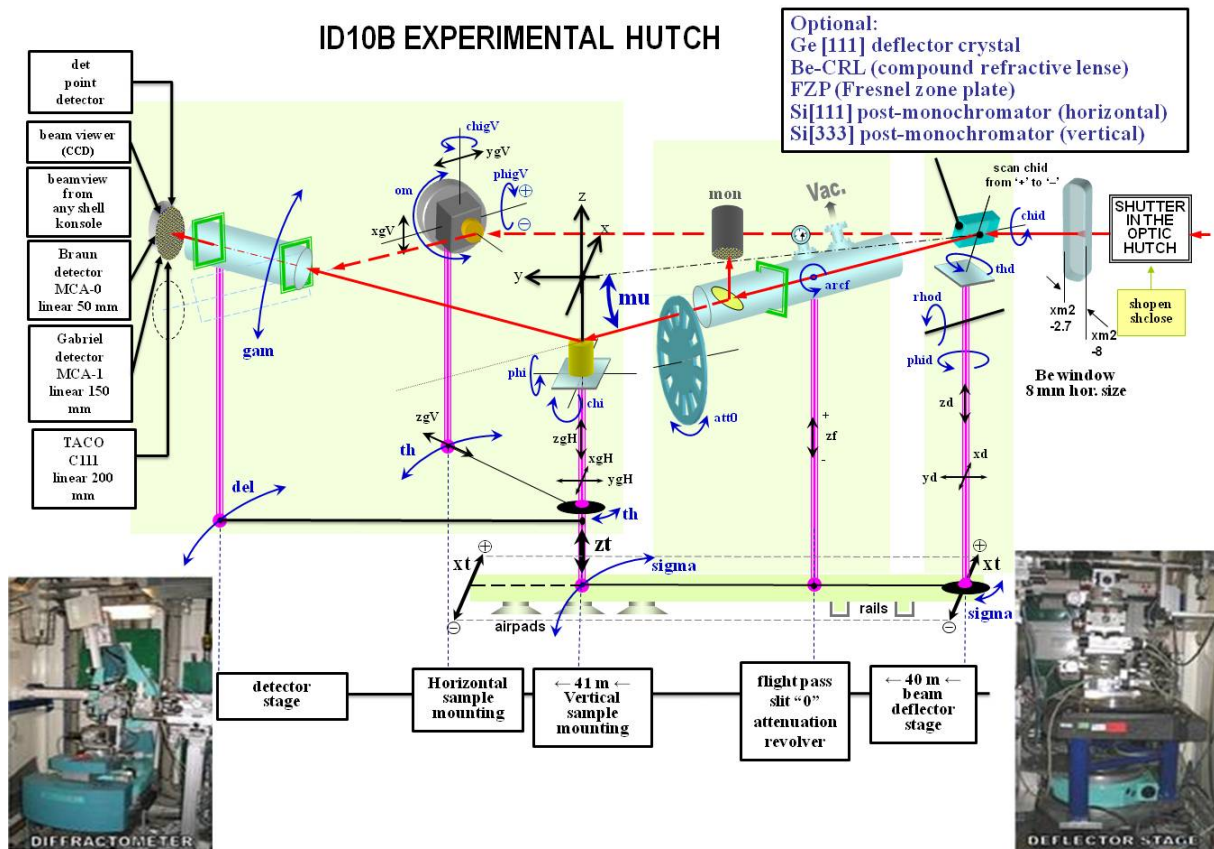


Figure 3.1b Scheme of optics elements of the beamline ID 10B from the X-ray source to the sample position. The main components of the optics hutch are the double-crystal monochromator and the two Si mirrors. The distance of the elements from the X-ray source is indicated. Courtesy – ID 10B beamline, ESRF, Grenoble.

reflected/diffracted beam. Additionally a flight tube is mounted within the beam path to reduce the air-scattering. The PSD detector is a one-dimensional positional sensitive detector (PSD) having 1024 channels. The resolution of the detector was 74.73 channels per degree, resulting in a total angular range of 13.7° . In front of the PSD soler slits are mounted to achieve high azimuthal resolution. This detector is used for gracing incident scans and detector scans. CCD detector has 2048×2048 pixels of $65 \mu\text{m}$ size set at 30 cm from the sample. Here the beam size was $0.1 \times 0.3 \text{ mm}^2$.

The goniometer allows several rotations and movements. The possible movements are illustrated in Figure 3.3. The sample can be rotated within the coplanar direction with the motor labelled with χ . The tilt out of the co-planar direction is adjusted with the ϕ drive. The theta circle is used for azimuthal adjustment of the sample with respect to the primary beam. With these three drives the alignment in the primary beam is performed and the incident beam of the experiment is set.

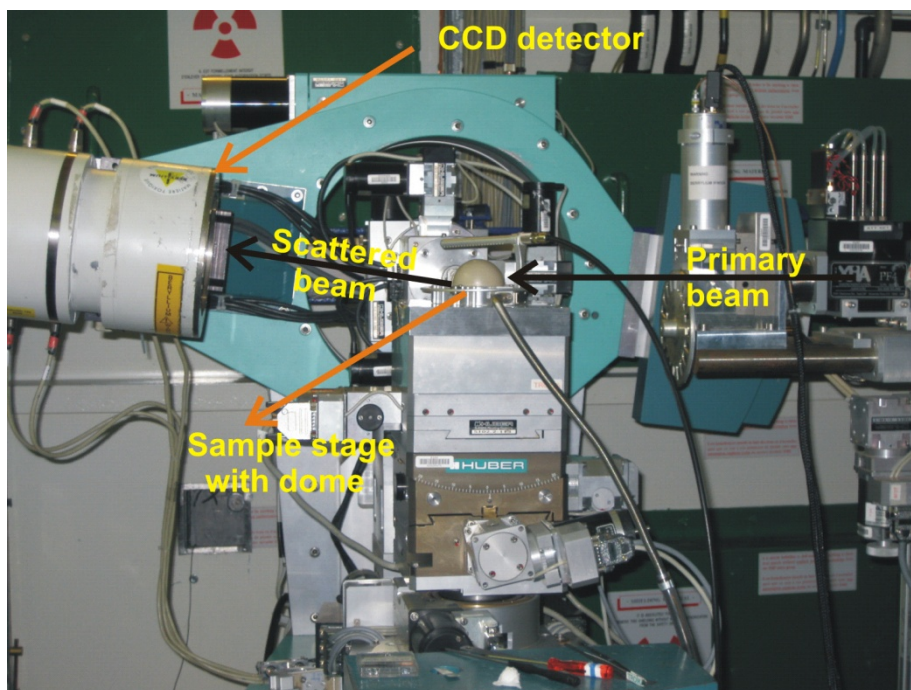


Figure 3.2 Image of the ID10B experimental setup at ESRF, Grenoble, France.

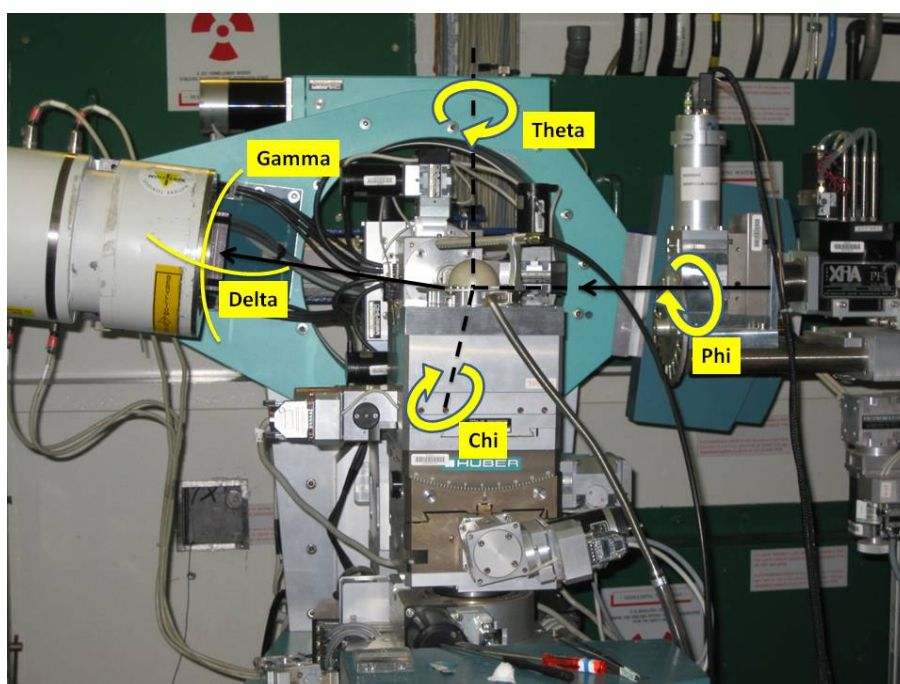


Figure 3.3 Movements of the different motors of the ID10B goniometer.

For an azimuthal rotation in the in-plane scans of the sample the phi and chi drive can only be fixed for an incident angle of 0.18° (pre-tilted beam) given that the azimuthal rotation (theta) is located below the phi and chi drives. This would cause a stagger of the sample surface in respect of the rotation axis and therefore a change of the incident angle α_i during the

rotation. The detector arm has two directions for a movement. They are labelled as gamma, the exits angle of the experiment and Delta represents the in-plane scattering angle. Type of reciprocal scan depends on the kind of information one is looking from the sample, especially for our polymer samples we have performed the following scans in q-space

Specular Scan – An equally variation of the incident and exit angle results in a scan that is strictly along the q_z direction with a variation of $|q|$.

Detector scan or Out-of-plane scan – The variation of the α_f for a constant incident angle results in a variation of q_x and q_z . The direction of q changes as well as $|q|$.

Rocking curve scan – For a fixed detector position the sample is rotated whereby the sample surface normal remains in the co-planar plane. The resulting scan is along the circle $\sqrt{q_x^2 + q_z^2} = |q|$ direction with varying incident and exit angle. At small angles of incident and exit the scan can be seen as pure q_x -scan. The direction of q changes but not the length ($q = \text{constant}$).

In-plane scan – The scan is performed for α_i and α_f close to the critical angle of the sample under investigation. The detector moves in the azimuthal direction keeping $\alpha_i = \alpha_f = \text{const}$. The resulting scan is within the XY plane with $\sqrt{q_x^2 + q_y^2} = |q_{xy}| = |q_{||}|$. The direction and length of q changes depending on kind of scan.

3.2. Experimental Set-up for X-ray Scattering Techniques

The setups for X-ray diffraction measurements are shown in Fig. 2.11. The film thickness can be measured precisely by X-ray reflectivity setup (Fig. 2.11a). whereas Specular reflectivity (SR) measurements are sensitive to the electron density distribution $\rho_{el}(z)$ perpendicular to the sample surface as well as to top surface roughness, independent of the sample being crystalline or amorphous [3, 4]. The scattering contrast is provided by the difference in the polarizability between the layers and the substrate. Experimentally, the SR is measured in the plane of incidence when the condition $\alpha_i = \alpha_f$ is satisfied. All the SR curves were measured using a different energy at different beam time. In this work, the SR technique has been used to calculate the thickness of the OFET thin films. Here, the angles of incidence, α_i , and exit angle, α_f , vary by the same amount resulting in a momentum transfer Q_z , parallel to the surface normal. The period Δq_z of the oscillation is $\Delta q_z \approx 2\pi/d$ and it is inversely proportional to the thickness Δd of the layer that induces the oscillation.

To compare all the measurements performed at different synchrotron source considering the different wavelength used, all the data converted into Q space. As mostly the experiments performed at Delta and the ESRF were done under different energy, the critical angles of the thin polymer films always follow the $\alpha_{cf} < \alpha_i < \alpha_{cs}$ conditions (the specific values of all three angles are different for different beam time, therefore the particular values are given for individual measurements under upcoming chapters). For grazing-incidence out-of-plane diffraction (GOD), the exit angle or the detector angle $\alpha_f \approx 2\Theta_{OP}$ is scanned in a wide angular range (Fig. 2.11b). In this case the scattering vector Q is not exactly directed along the surface normal. Bragg peaks appear whenever the crystallite orientation shows a wide distribution of crystal orientations.

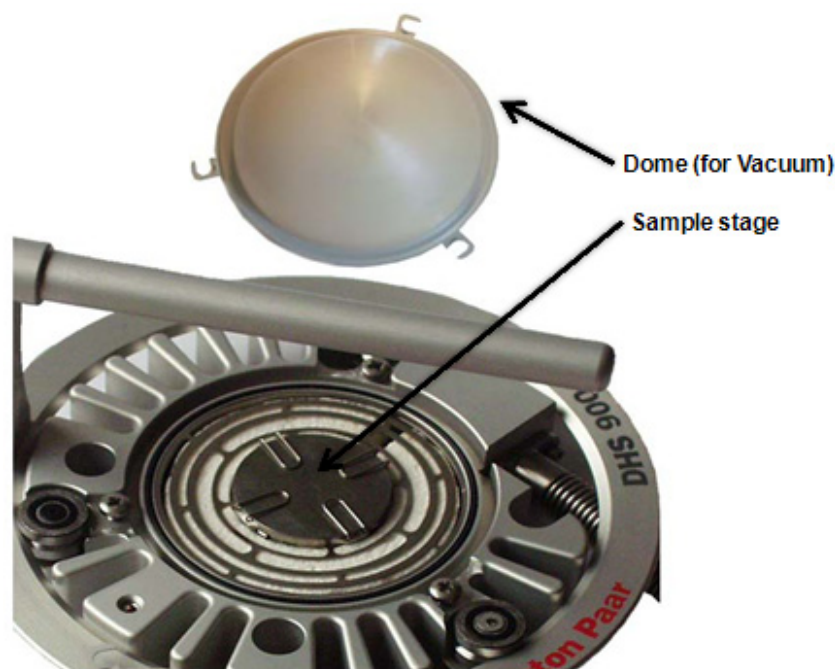


Figure 3.4 Anton Paar heating stage utilised for temperature dependent in-situ X-ray diffraction measurements.

Finally, grazing-incidence in-plane diffraction (GID) is performed under the same conditions for α_i , but the scattering signals were collected by moving the detector horizontally and collecting the signal by changing the in-plane angle, $2\theta_{in} = \theta_i + \theta_f$ angle of the detector (Fig. 2.11c). In GID all diffraction vectors are laying in the surface plane. Expressed in the reciprocal space coordinates the momentum transfers can be expressed by the eqs. 2.33 – 2.35. All X-ray measurements were performed under vacuum conditions ($\sim 10^{-3}$ mbar) using the DHS 900 domed hot stage provided by Anton Paar GmbH, Graz, Austria (Fig. 3.4). This

was essential in order to avoid substantial radiation damage at the polymer sample and to reduce background scattering.

3.3. Sample Preparation

3.3.1. Material

Poly(3-hexylthiophene) is a commonly used polymer in organic field-effect transistor (OFET) because it exhibits high charge carrier mobility and it is well processable using organic solvents [5]. P3HT can have mainly two configurations, regioregular or regiorandom polymers. The above two configuration have a huge effect on the ordering, crystallinity and the electrical properties. It is also found that their spectroscopic and spectro-electrochemical properties depend on the molecular weight and the polydispersity coefficient [6]. For this reason we investigated regioregular P3HT (>99% HT-HT couplings), which was fractionated into several fractions. The fractionation of P3HT can be briefly described as follows. P3HT obtained via polycondensation of the Grignard reagent was first precipitated with methanol, filtered, and washed with a mixture of water and methanol. This crude polymer was then dried until constant mass was reached. The crude polymer was first extracted with ethyl acetate in a Soxhlet apparatus until the filtrate was colorless. The remaining insoluble part was then extracted consecutively with hexane, dichloromethane and chloroform in the same manner as in the case of ethyl acetate [6, 7]. NMR studies on different molecular weight fractions revealed that the relative concentration of structural defects due to irregular head-to-head or tail-to-tail linkages (Figure 1.8) only very slightly increases with decreasing molecular weight. The specific information on the molecular weights and polydispersity of P3HT are presented in individual chapters as used. All the raw P3HT material of high and low molecular weight fractions are synthesized in the group of Prof. Ullrich Scherf at the University of Wuppertal, Germany.

3.3.2. Solution Processable – Spin Coating Technique

There are many solution processable thin film preparation techniques, among of them Drop casting, Dip coating and Spin coating techniques are widely in use (Fig. 3.5). Spin coating is the preferred method for application of thin, uniform films to flat substrates. This process is very simple, illustrated in Figure 3.5c. An excess amount of polymer solution is placed on the substrate. The substrate is then rotated at high speed in order to spread the fluid by cen-

trifugal force. Rotation is continued for some time, with fluid being spun off the edges of the substrate, until the desired film thickness is achieved. The solvent is usually volatile, providing for its simultaneous evaporation.

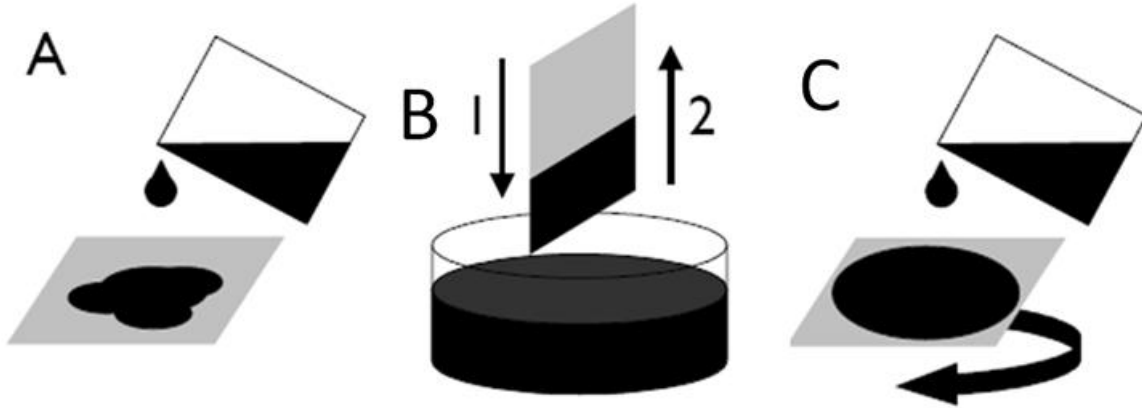


Figure 3.5 Solution processable thin film preparation techniques (a) Drop casting, (b) Dip coating, (c) Spin-coating.

This process is used extensively in microlithography for the manufacture of integrated circuits. Spin coating permits to obtain good optical quality and homogeneous films with thicknesses ranging in the micrometer size. The film thickness can be controlled, during the deposition procedure, varying the viscosity of the solution and the spinning rate. The film is deposited on the top face of the substrate at room temperature.

Dip coating (Fig. 3.5b) also yield good optical quality and homogeneous films. The cleaned substrate is slowly (few mm/s) dipped into and raised out of the precursor solution. It should be noted that both faces of the substrate result covered by the film.

Thicker films can be obtained by Drop casting technique (Fig. 3.5a). Few drops of precursor solution are deposited on the substrate and let dry under controlled conditions. Thicknesses up to hundred micrometers have been obtained. The main drawback of this technique is that the flatness of the film is not ensured.

3.3.3. Modification of the Substrate via Dielectric Layers

Highly-doped silicon with thermally grown 300 nm thick silicon dioxide layer (capacitance per unit area is 11 nF/cm², purchased from Silchem Co. Freiberg, Germany) was used as the substrate and the gate-insulator. In all cases, the substrates were cleaned with the following detergents and solvents: Helmanex (5% volume in Aquaes), Milli-Q water, acetone and isopropanol. Each cleaning step was performed for 20 minutes in an ultrasonic bath. For si-

lanisation, Hexamethyldisilazane (HMDS) and OTS (Octadecyltrichlorosilane), purchased from Merck, Darmstadt Germany, used as received). Both silanisation provide the hydrophobic surface but due to more hydrophobic nature of OTS, OTS provide much better surface interaction to the organic molecules and become a good dielectric layer for as spun samples.

Three different types of surface treatments were employed prior to the deposition of the P3HT (Fig. 3.6). The first substrate type was only wet-cleaned in an ultrasonic bath with (acetone, isopropyl alcohol), in the following termed called untreated or bare SiO_2/Si substrate. The other two were used for silanisation immediately after ultrasonic treatment. Two types of silane molecules, Hexamethyldisilazane (HMDS) and Octadecyltrichlorosilane (OTS), [8, 9] respectively, were used. The HMDS was deposited by spin coating using 10% HMDS / 90% chloroform solution at 2000 rpm for 30 seconds.

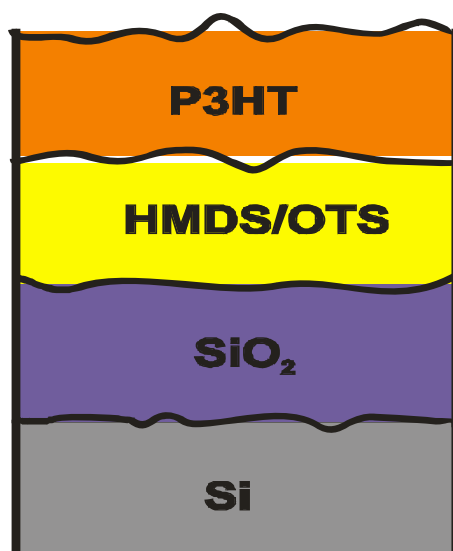


Figure 3.6 Scheme of the polymer sample on top of modified SiO_2 of thickness 300 nm.

The OTS treatment also done using spin coating a 10% OTS / 90% chloroform solution at 2000 rpm for 30 seconds. To vary the thickness of the polymer layer, the concentration of P3HT in chloroform solution was varied, keeping the other conditions, spinning speed and spinning time constant (4000 rpm, 30 sec).

3.3.4. Optimizing the Gate-Insulator Surface

As we know SiO_2 layers for inorganic devices from long time acting as a dielectric layers, parallel to it has also some concern that it exhibits high density of hydroxyl groups, which gives rise to high surface free energy and, by this, to a tendency of forming strongly

adhering layers of adsorbed contaminants from the ambient atmosphere. At the same time to increase the molecular substrate interaction one needs strong hydrophobic layers, specially for organic films where charge transport go through first ~10-20 nm thickness from the substrate.

From the literature, modification of the SiO₂ gate insulator using silanization with Hexamethyldisilazane (HMDS) [11, 12] and oxygen plasma treatment [13, 14] prior to the deposition of organic semiconductor has been found to affect the film morphology as well as reducing the number of surface trap states formed by Si–O–H. At the same time different treatments can also induces different molecular orientation as found by Kim et al. [9] that depending on the properties of particular modified substrate after the different SAMs treatment, the P3HT crystalline domains can adopt the two different orientation – edge-on (perpendicular to the substrate), flat-on (parallel to the substrate), where the edge-on has found mobility four times higher than flat-on. The increased mobility is referred to the increase of substrate mediated molecular interaction with some factors responsible are the unshared electron pairs of the SAM end groups, the p-H interactions between the thienyl –backbone bearing p system and the hydrogen atom of SAM end groups.

Under our current study we have basically used HMDS and OTS mediated substrate modifications and our results have not noticed the serious change of molecular orientations or tremendous improvements of structure properties by using any particular surface treatment. In fact our assessment is that OTS is good for as prepared sample while HMDS behaves better after annealing effect, under both treatment we have found the mixed orientation, where edge on dominates on flat on orientation.

3.4. References

- [1]. <http://www.esrf.eu>
- [2]. <http://www.esrf.eu/userdandscience/experiments/scmatter/ID10B/>
- [3]. Pietsch, U; Holy, V; Baumbach, T; High-resolution X-ray Diffraction from Thin films and Lateral Nanostructures, 2nd ed.; Springer: Berlin, Vol. 2, p 40, 2005.
- [4]. M. Tolan, X-Ray Scattering from Soft-Matter and Thin Films-Materials Science and Basic Research, Springer, Berlin, 1999.
- [5]. Gamota, D. R.; Brazis, P.; Kalyanasundaram, K.; Zhang, J. Printed Organic and Molecular Electronics; Kluwer Academic: Dordrecht, The Netherlands, 2004.
- [6]. Trznadel, M.; Pron, A.; Zagorska, M.; Chrzaszcz, R.; Pielichowski, J. *Macromolecules*, 31, 5051, 1998.
- [7]. Loewe R. S.; Khersonsky, S. M.; Mc Cullough, R. D.; *Adv. Mater.*, 11, 250-253, 1999.
- [8]. Kline, R. J.; McGehee, M. D.; Toney, M. F.; *Nature Mat.*, 5, 222-228, 2006.
- [9]. D. H. Kim, Y. Jang, Y. D. Park, K. Cho, *Macromolecules*, 39, 5843, 2006.
- [10]. Achmad Zen, PhD thesis, University Potsdam, Potsdam, Germany, 2006.
- [11]. Merlo, J. A.; Frisbie, C. D. *J. Polym. Sci. Polym. Phys.*, 41, 2674, 2003.
- [12]. Gorjanc, T. C.; Levesque, I.; Dlorio, M. *Appl. Phys. Lett.*, 84, 930, 2004.
- [13]. Yang, Y. S.; Kim, S. H.; Lim, S. C.; Lee, J.; Lee, J. H.; Do, L.; Zyung, T. *Appl. Phys. Lett.*, 83, 3939-3941, 2003.
- [14]. Park, S. K.; Kim, Y. H.; Han, J. I.; Moon, D. G.; Kim, W. K., *Thin Solid Films*, 429, 231, 2003.

Chapter 4

Room Temperature based X-ray Structure and Crystallinity studies of LMW Poly (3-hexylthiophene) Fraction

This chapter will illustrate the low molecular weight fraction of poly(3-hexylthiophene) room temperature study by means of various techniques i.e. Atomic force microscopy (AFM), TEM and X-ray scattering techniques particularly X-ray diffraction methods under grazing incidence geometry (GOD and GID scans). X-ray diffraction studies are primarily focussed and those were well supported by AFM and TEM as secondary techniques.

Here, X-ray diffraction studies were performed in order to understand the crystallinity, the molecular orientation and the nanoscale morphology of low-(LMW) fractions of Poly (3-hexylthiophene) (P3HT) thin films. The thickness of the films was found to be in the range between 10 nm and 200 nm. Further structural information was obtained using X-ray grazing incidence in-plane and out-of-plane diffraction using synchrotron radiation. The X-ray analysis reveals that the films are mainly amorphous and contain randomly oriented nanocrystallites with the best match for a monoclinic unit cell. Additionally, polymorphism was found for ~200 nm thick films of LMW fraction. Interestingly, the film morphology varies as a function of the film thickness. For LMW material the random orientation of nanocrystallites changes to preferential orientation of lamellae along the surface normal when the size of crystallites become of the order of film thickness, i.e. below 20 nm.

4.1. Sample Preparation

All the samples prepared by spin coating technique, which is described in detail under chapter 3. The molecular weight of low molecular weight fraction P3HT is $M_n = 2582$ g/mol and $M_w = 3623$ g/mol, where the polydispersity can be calculated by $PD = M_w/M_n = 1.4$. The numbers of average thiophene rings present in individual molecules were 14 and the length of each molecule is 6 nm. All these macromolecular parameters derived from Gel Permeation Chromatography (GPC) technique are summarized in table 4.1. To understand the thickness dependent structure variation we have prepared number of samples of varying thickness, by varying the concentration of P3HT and keeping rest parameters fixed. All the samples analyzed in this study are summarized in table 4.2.

Compound	M_n / g/mol	M_w / g/mol	<i>PD</i>	<i>DP</i>	<i>L</i> [nm]
P3HT ethyl acetate fraction	2582	3623	1.40	14	6

Table 4.1 All the macromolecular parameter derived for LMW Poly(3-hexylthiophene).

4.2. Atomic Force Microscopy (AFM) Studies

AFM and followed by TEM studies under the present thesis are contribution from our collaborator Prof. Neher Group, University Potsdam, Germany. The morphology of layers from the low molecular weight fraction of P3HT for as prepared samples, have been studied using Atomic Force Microscopy (AFM). The AFM images shown in Figure 4.1a-b reveal that as-prepared layers of the ethyl acetate fraction contain “ribbon-like” crystallites.

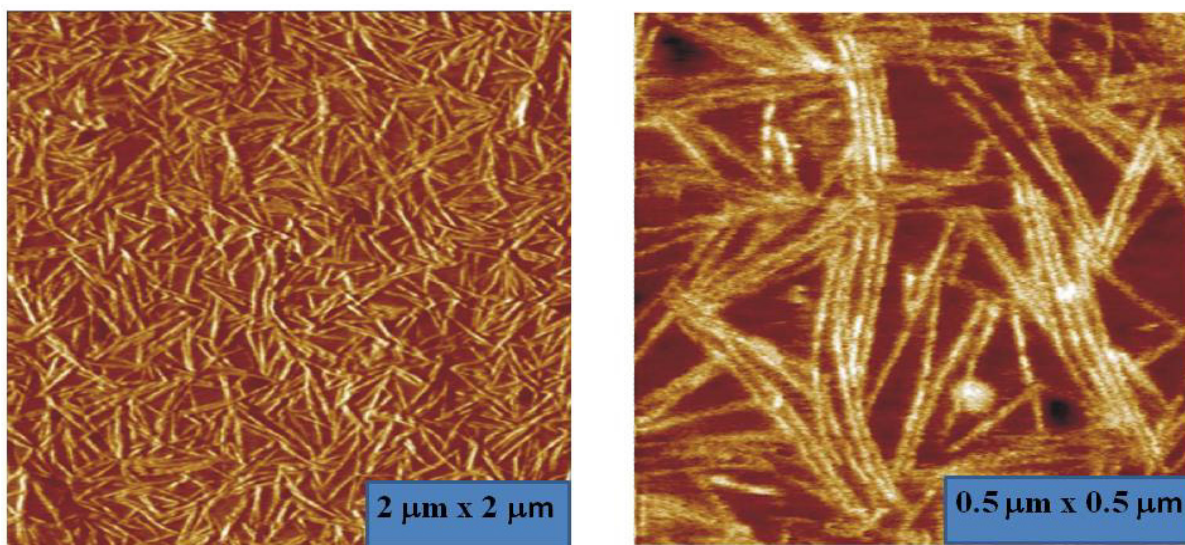


Figure 4.1 AFM phase images of low molecular weight material P3HT for as prepared samples with different length scales [7, 9].

The apparent average width of these long ribbons is 25 ± 8 nm, corresponding to a real geometrical width of approx. 11 nm [1]. Most probably, the polymer chains are oriented in the way that the conjugated backbone is parallel to the substrate and perpendicular to the long axis of the ribbons. In general the findings on as prepared layers are in agreement with the results of AFM studies published by Kline et al. [2].

4.3. Transmission Electron Microscopy (TEM) Studies

We have seen from AFM images that the low M_w -fraction layers (as-prepared) exhibits a structure formed by whiskers (or ribbons) of 100-200 nm length. These whiskers can be clearly identified in the phase AFM image shown in Figure 4.1a-b. The apparent average width of these long whiskers is approx. 11 nm. Since the length of one polymer chain in the low molecular weight fraction is ca. 6 nm on average, we concluded that the polymer backbones are oriented normal to the long axis of the whiskers. However, using AFM we can only investigated the surface of the thin films and not the whole layer. Therefore, we performed an investigation using transmission electron microscopy (TEM) in order to obtain additional structural information. In the bright field (BF) micrograph (see Figure 4.2) similar whisker-like structures can be observed.

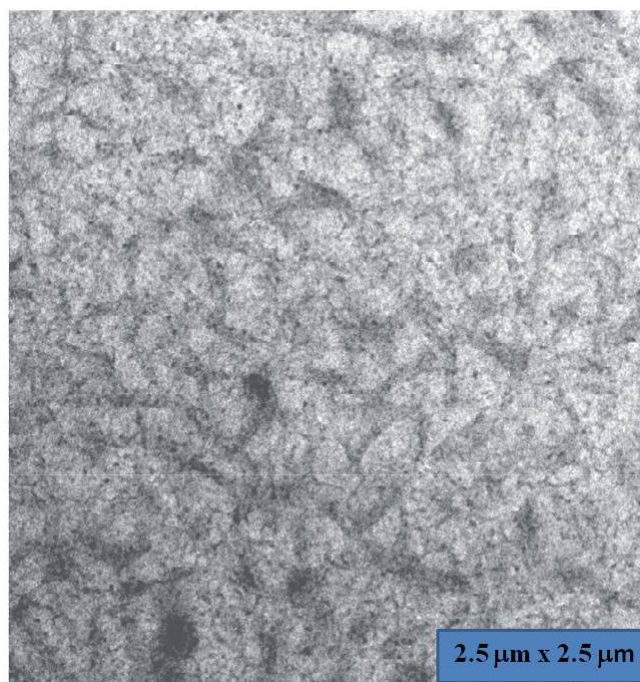


Figure 4.2 TEM bright field image of LMW P3HT performed at -120°C to avoid damages of the layers due to electron beam [7, 9].

Note that the bright field images have to be taken with a certain amount of under focus (phase contrast) in order to visualize the contrast of those whiskers, indicating that the thin P3HT films consist of two phases, a crystalline one which is embedded in an amorphous region. Contrary to that, if the whiskers are not embedded within a matrix it would show a mass-thickness contrast in TEM, noticeable by in-focus visibility. Since this is not the case, the assumption of a two phase system with crystals embedded in amorphous matrix is highly

probable. The graphs also display nicely, that many of the whiskers are bundled together and these bundles are surrounded by a non-crystalline phase.

4.4. Determination of Layer Thickness

Reflectivity measurements were performed to determine the film thicknesses. Fig. 4.3a shows the results of the reflectivity measurements of the samples prepared from different solution concentrations. Due to interference of waves reflected from the vacuum-sample and film-substrate interfaces, Kiessig fringes are clearly visible. The film thickness, t , was obtained from the distance ΔQ_z between two consecutive maxima, where $t = 2\pi/\Delta Q_z$. Except for the thickest sample #1, all samples show the large number of Kiessig fringes which verify the homogeneity of the film thickness which fluctuates by only about 3 nm within the illuminated sample area. The extracted film thickness values are shown in Table 4.2.

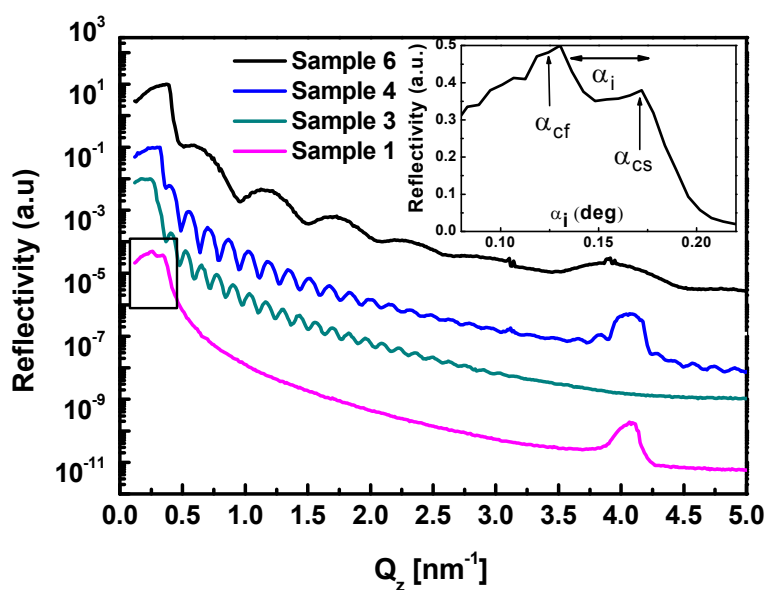


Figure 4.3a Reflectivity measurements of P3HT samples of various thicknesses. The inset shows the angular region of total external reflection of sample #1. Further GID and GOD scans were recorded setting the incidence angle α_i to $\alpha_{cf} < \alpha_i < \alpha_{cs}$, where α_{cf} and α_{cs} are the angle of total external reflection of film and substrate, respectively.

Considering the relation between concentration and film thickness of the other samples the thickness of sample #1 was estimated to be $t \approx 200$ nm. Because of the large thickness sample #1 displays the two critical angles, α_{cf} and α_{cs} , very well (see inset of Fig. 4.3a). For the following GID and GOD scans the incidence angle, α_i , was fixed under the condition $\alpha_{cf} < \alpha_i < \alpha_{cs}$, in order to maximize the ratio between film to substrate scattering.

S. N.	Sample	Thickness t , (nm)	d_{100} (nm)	d_{020} (nm)	Crystallite Size L_c (nm)
#1	40mg/ml on HMDS	No thickness oscillation found	1.57 ± 0.02	0.38 ± 0.02	40.0 ± 0.5
#2	10mg/ml on HMDS	48 ± 3	1.56 ± 0.05	0.38 ± 0.02	23.5 ± 2
#3	5mg/ml on HMDS	40 ± 3	1.55 ± 0.07	0.38 ± 0.03	24.7 ± 2
#4	5mg/ml on OTS	40 ± 3	1.55 ± 0.07	0.38 ± 0.03	23.1 ± 2
#5	3mg/ml on HMDS	27 ± 2	1.56 ± 0.07	0.38 ± 0.04	16.8 ± 3
#6	1mg/ml on HMDS	10 ± 2	1.55 ± 0.05	0.38 ± 0.05	12.4 ± 3

Table 4.2 Calculated thickness and structural properties of crystallites of P3HT samples at Room temperature.

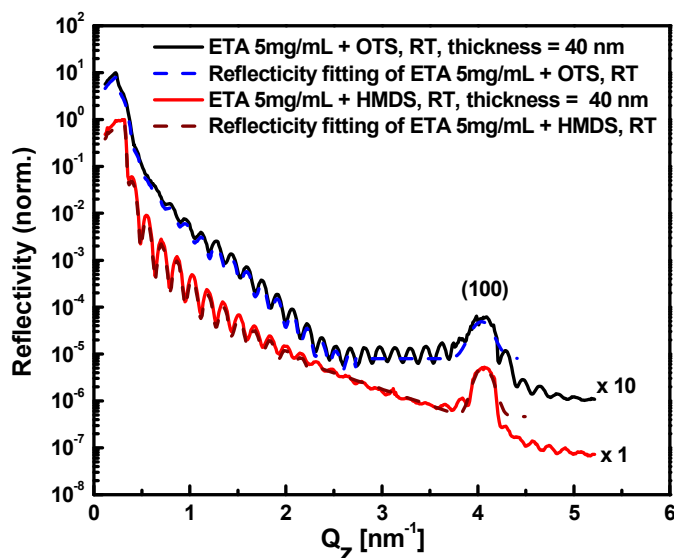


Figure 4.3b Reflectivity measurements of sample #3 and sample #4 corresponding to pre-treatment of substrate by HMDS and OTS modified substrate, the thickness of both samples is same ($t = 40$ nm), for the better clarity of individual curve, black curve intensity multiplied by 10.

At the same time Fig. 4.3b shows the similar nature of Kiessig fringes for 5mg/ml P3HT samples having thickness ~ 40 nm on top of OTS and HMDS coated substrates. extending the reflectivity curves we can see the appearance of broad Bragg peak for P3HT sample on top of the OTS coated SiO_2/Si substrate, which is not well pronounced and shows the shouldering effect, which clearly resembles the presence of random orientation and small size of crystallites, while there is no shouldering effect found for P3HT grown above HMDS

coated SiO₂/Si substrate, as well as appeared Bragg peak (100) is sharper than OTS sample, indicates the better crystal orientation. Using Scherrer's equation [3] the measured FWHM of the (100) peak was used to determine the correlation length, L_c , parallel to surface normal. L_c can be identified as the crystallite size in this direction and the values are listed in Table 4.2. Considering two layer system we have fitted the both reflectivity curves, their computed values after fittings have shown under table 4.3.

Sample P3HT 5mg/ml	Thickness SiO₂ (nm)	Thickness P3HT (nm)	Air-P3HT Roughness (nm)	P3HT-SiO₂ Roughness (nm)	Density g/cm³
HMDS	271	41.00	1.24	1.47	1.371
OTS	284	43.10	1.93	1.280	1.373

Table 4.3 Computed values from fitting of various reflectivity scans at RT for HMDS as well as for OTS coated substrate.

4.5. X-ray Grazing-Incidence Diffraction Studies

For a detailed study of the structural properties of LMW fraction thin films ($t \sim 10$ – 200 nm) grazing incidence diffraction techniques (GID and GOD) [4] have been employed, which are well explained in details under chapter 2.

As we know, P3HT film shows mostly two preferred lamellae orientations structure, namely, edge-on and face-on orientation [5]. To understand it better in details such 2D lamellae structure orientation we have exploited the GID and GOD X-ray diffraction. The scattering scheme has already explained and shown in chapter 2, Figure 2.11. This GID and GOD setup allows measurement of a momentum transfer in the directions parallel and perpendicular to the surface normal. For the OOP scan, one changes the angle of exit, α_f with respect to the surface under conditions of fixed incidence angle α_i [5, 6], in the second case the in-plane diffraction angle $2\theta = \theta_i + \theta_f$ is varied for fixed α_i [6, 7]. Both GID and GOD are realized at extremely reduced penetration depths of the probing X-ray within the sample.

Our X-ray measurements were mainly performed at European Synchrotron Radiation Facility (ESRF), Grenoble, France at the undulator beamlines ID01 and ID10B ('Troika II') using wavelengths 1.54 \AA and 0.92 \AA , respectively, and an energy resolution better than 10^{-3} . Additional measurements were performed at Delta (University of Dortmund). Considering the

wavelengths used at both ESRF beam lines (ID01/ID10B), the critical angle of thin P3HT film and underlying substrate $\alpha_{cf} = 0.14^\circ$, $\alpha_{cs} = 0.23^\circ$ and 0.09° , 0.14° , respectively.

The data were collected by a point detector or a 1D -position sensitive detector (PSD) oriented parallel to the surface normal. It could be scanned both horizontally and vertically with respect to the direct beam. For GID, a Soller slit was installed in front of the detector, providing an angular resolution of $\Delta\theta = 0.1^\circ$. Due to alignment of the PSD in vertical scanning direction a range of vertical scattering angle of about $\Delta\alpha_f \sim 6^\circ$ could be captured by a single exposure.

4.6. GID and GOD Studies at Room Temperature

GID profiles of film made from LMW fraction with film thickness of 40 nm for different angle of incidence α_i^s are shown in Fig. 4.4. Depending on α_i the scattering signal was detected from polymer thin film only at $\alpha_i = 0.12^\circ$ (black curves), the film and few nanometers of substrate at $\alpha_i = 0.18^\circ$ (red), and from the film and hundreds of nanometers of substrate ($\alpha_i = 0.23^\circ$ green). Five peaks are present for the case of LMW fraction at the smallest α_i .

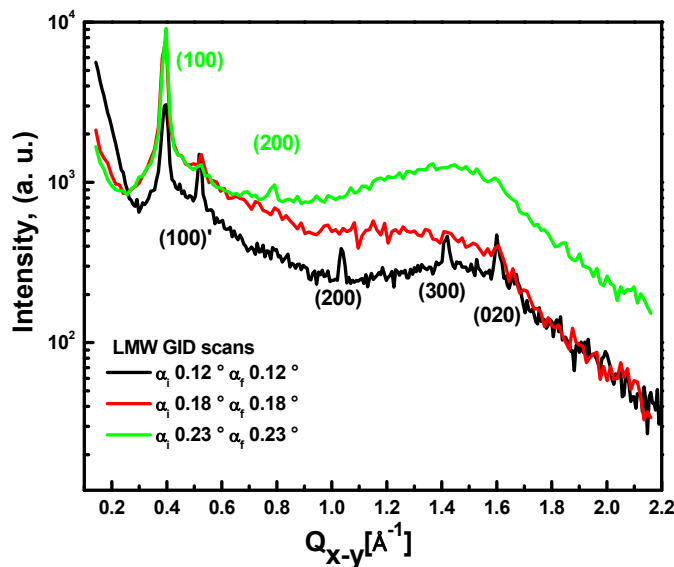


Figure 4.4 GID profiles for the low molecular weight fraction. Surface, subsurface and bulk profiles are shown by black and red and green curves, respectively.

Increasing α_i structural peaks of higher order (Figure 4.4, green and red curves) appear only when $\alpha_i < \alpha_{cf}$. For higher incidence angle the diffuse halo close to $Q_{xy} = 1.4 \text{ \AA}^{-1}$ dominates on diffraction pattern. Because strong amorphous scattering of underlying SiO_2 starts to

dominate at the higher angles, therefore the structural information of the polymer film can be probed only at very shallow angles (see black curve, Fig. 4.4). The α_i dependence suggests that for small α_i the (100) stacking along surface normal direction is well pronounced compared to higher α_i ^s, as for higher α_i ^s diffuse scattering is too large to see the crystallites contribution from particular top surface or at the interface level. Additionally, for LMW fraction we found two different types of crystallization (polymorphism) shown by black and green indexes in the Figure 4.4. The diffraction intensity from planes parallel to the interface has been detected by grazing-incidence out-of-plane diffraction (GOD) (Fig. 4.5). Here α_i was fixed at the condition $\alpha_{cf} < \alpha_i < \alpha_{cs}$ and the detector angle α_f was scanned over a wide angular range.

Both molecular weight fractions display a well-pronounced periodicity normal to the surface due to alkyl chain stacking. The different inter-planar distances for such stacked sheets were found to be ~ 15.5 Å and ~ 16.5 Å for low and high weight molecular fractions, respectively. This reflects that the ‘d’-spacing might be a function of molecular weight. Both fractions show same shape of amorphous halo centered at $Q \approx 1.4$ Å⁻¹; probably caused by the scattering from SiO₂.

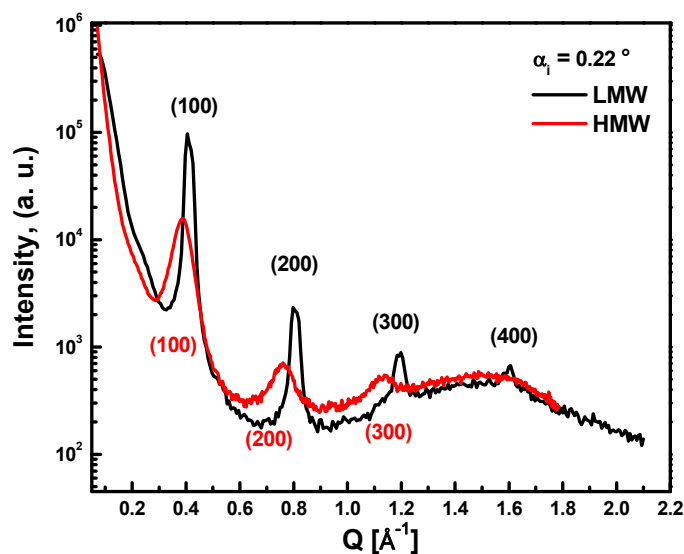


Figure 4.5 GOD profiles for the low and high molecular weight fractions, black and red curves.

The peaks for LMW are much pronounced and sharper than HMW fraction; it reveals a smaller crystallite size for HMW fraction compared to LMW material. The average crystal size was $D \sim 25$ nm and $D \sim 8$ nm for the LMW and the HMW fractions, respectively. The appearance of pronounced peaks for LMW than HMW does suggest the presence of higher degree of crystallinity compared to HMW fraction.

Our preliminary measurements indicate that the morphology of LMW P3HT films is more complex and provides better ordering of nanocrystalline domains and existence of two polymorphs. Therefore, our further study mostly focused on the detailed investigations of the LMW P3HT films. Considering the angular dependent results shown in Fig. 4.4 and Fig. 4.4, our further studies focussed on the measurements at shallow incident angles (α_i^S) with varying thickness of the samples. This can help to understand the contribution of bulk as well as surface-interface region.

4.6.1. Image Plate Measurements

We have first probed the thickest (sample #1) and thinnest sample (sample #6) by image plate exposures at Delta Synchrotron source, Delta, Dortmund, Germany. Here $\alpha_i < \alpha_{CS}$ was fixed and the 2D scattering of the film was recorded within 30 minutes of exposure time.

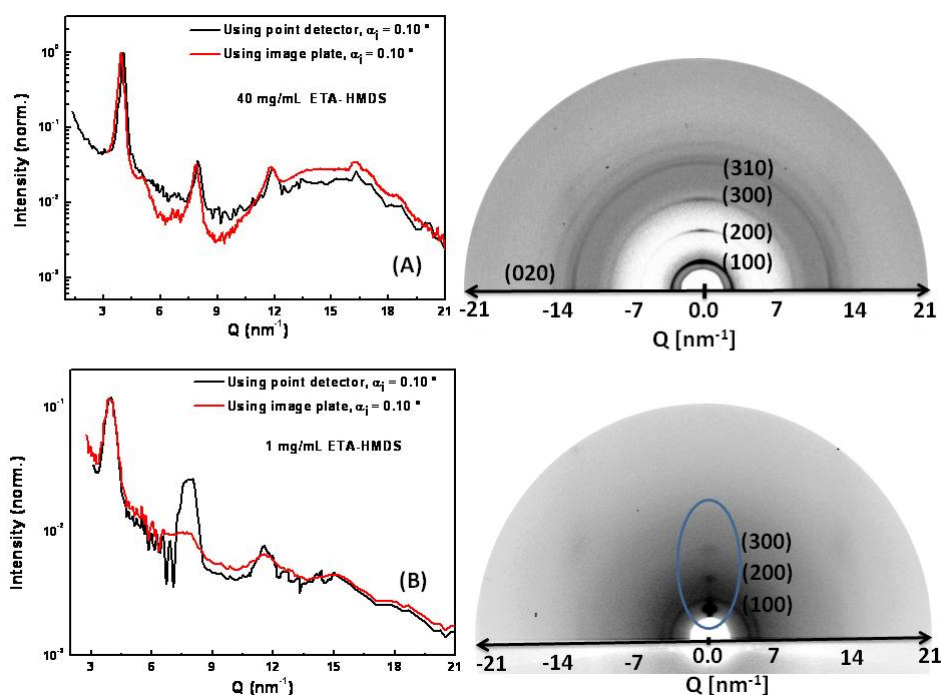


Figure 4.6 2D images taken in grazing- incidence geometry of sample #1 (A) and sample #6 (B) at 15.2 keV (right). Extracted lines scans are compared with point detector measurements taken at equal scattering geometry (left).

For sample #1 one can see the closed rings with Q radii corresponding to (100) and its higher multiples with a small preference along the surface normal. In addition one finds a ring related to (020) and another lattice parameter (Fig. 4.6a). The peaks appear onto a non-uniform background caused by diffuse scattering from disordered P3HT, the SiO_2 and the

background scattering of the experiment. As the background intensity is low close by the (200), no closed ring is seen for this reflection.

However, a line scan extracted from the image plate data showing the (h00) and (020) peaks coincide well with a scan taken with a point detector under same geometric conditions. In contrast to this, sample #6 displays distinct scattering spots in out-of plane direction (Fig. 4.6b) without a remarkable ring structure. Also there is no indication for the (020) peak. The different structural behavior found in both images can be interpreted by the transition from a random to a preferential orientation of the crystallites as a function of film thickness.

In order to study this different contrast of thick and thin films in detail, we performed GOD and GID line scan measurements with much higher intensity of the incident beam and improved signal to noise ratio at ESRF, Grenoble, France.

4.6.2. Grazing Incidence Diffraction (GID)

Fig. 4.7 shows the GID (in-plane) scans of films with three different thicknesses and two different surface treatments. At least 11 sharp reflections are visible for the thickest sample #1 as already seen on the image plate picture in Fig. 4.6a where at least a few peaks in the high angle range are missing due to low signal to background ratio.

Concerning the previous structure investigations for the same material [2, 7, 8], the low order peaks (100), (200) and (300) are related to the lamellar ordering of the phase separated structure in direction of the alkyl side chains. Further peaks appear at $Q_{xy} = 13.5, 14.4, 15.7, 16.4$ and 17.0 nm^{-1} . The peak at $Q_{xy} = 16.4 \text{ nm}^{-1}$ is indexed by (020) [5, 8, 9] and is associated by the in-plane π - π stacking distance which is 0.388 nm.

Following the structure solution suggested by Prosa et al. [10] and Brinkmann et al. [11]. This distance is very close to the distance between the two sulphur atoms of the thiophene backbones of 0.38 nm indexed with (002). Both peaks cannot be exactly resolved in our experiment. The other peaks are located on a broad amorphous background. One is centered at 11.0 nm^{-1} and is less dependent on film thickness; the second amorphous halo is centered at 16.0 nm^{-1} and is addressed to the amorphous scattering of SiO_2 .

It is observed that the low order peaks decrease as the film thickness decreases. One can observe the decrease of (100) peak intensity of sample #3 ($t = 40 \text{ nm}$) in comparison to sample #1 and it is completely disappeared for sample #6 ($t = 10 \text{ nm}$). This behavior is same for HMDS and OTS coated dielectric SiO_2/Si substrates having same polymer thickness (compare samples #3 and #4). At the same time most of the other wide angle peaks disappear

with decreasing film thickness as well except that of (020/002). Therefore the vanishing peaks must be indexed by reflections with $h \neq 0$. The samples with the intermediate thicknesses acquiesce into the trend (data not shown).

4.6.3. Presence of Polymorphism

Fig. 4.7 also shows the existence of two sets of additional reflections for the thickest sample, which is a direct evidence of polymorphism nature of LMW P3HT fraction. The second form indexed with (100)' appears at higher $Q_{x-y} = 5.25 \text{ nm}^{-1}$ compared to (100) ($Q_{x-y} = 4.05 \text{ nm}^{-1}$). It reflects an inter-planar distance of $d' = 1.20 \text{ nm}$ compared to the main form with $d = 1.56 \text{ nm}$. The appearance of higher order peaks such as (200)' and (300)' in addition to (200) and (300) gives evidence for perfect ordering of both polymorphs. Interestingly, such dual form is only observed at samples with highest concentration but not for thinner films. Like for the thick films, polymorphism was also found for the powder samples [9]. The same evidence again shown by out-of-plane scan as shown in Figure 4.8 for thick film only.

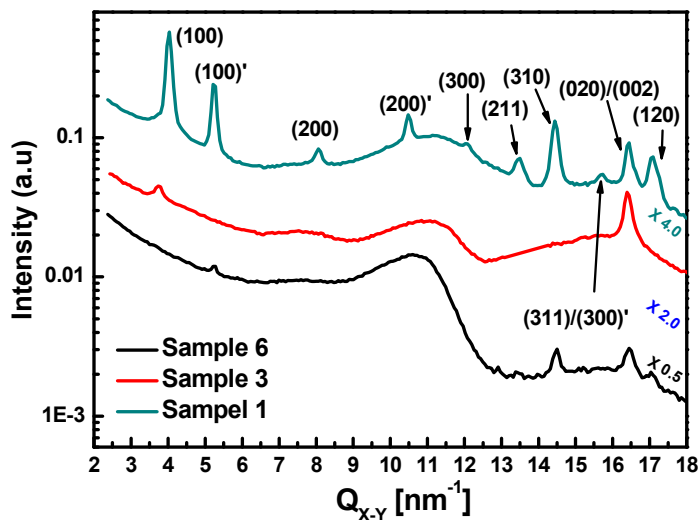


Figure 4.7 GID scans from samples with different thickness measured at $\alpha_i \leq \alpha_{cs}$. For better clarity all scans are separated by an offset factor.

4.6.4. Grazing Incidence Out-of-Plane Diffraction (GOD)

Fig. 4.8 shows the GOD scans taken at ESRF. Unfortunately, by technical reasons the low angle peaks in the range $Q < 8.0 \text{ nm}^{-1}$ of samples #1, #3 and #6 are affected by parasitic scattering from beam line components. These deficits can be compensated by GOD line scans

for sample #1 (after thermal treatment) and sample #6 shown in Fig. 4.6a,b where most of the high order peaks are no more visible due to the much lower peak to noise ratio. Considering the curves in Figs. 4.6a-b and Fig. 4.8 most of the wide angle peaks already found in GID (Fig. 4.7) appear for thickest sample. In addition further peaks are displayed at $Q_{xy} = 12.8, 14.4, 15.7$ and 17.0 nm^{-1} where the second one is most intense. These peaks are sitting on an amorphous halo centered at $q_{x-y} = 13.5 \text{ nm}^{-1}$ which approximately scales with film thickness and may reflect the diffuse scattering from disordered polymer units. As found in GID films of same thickness but prepared on HMDS or OTS coated SiO_2/Si substrates (sample #3 and #4) display same number of peaks with nearly same intensities.

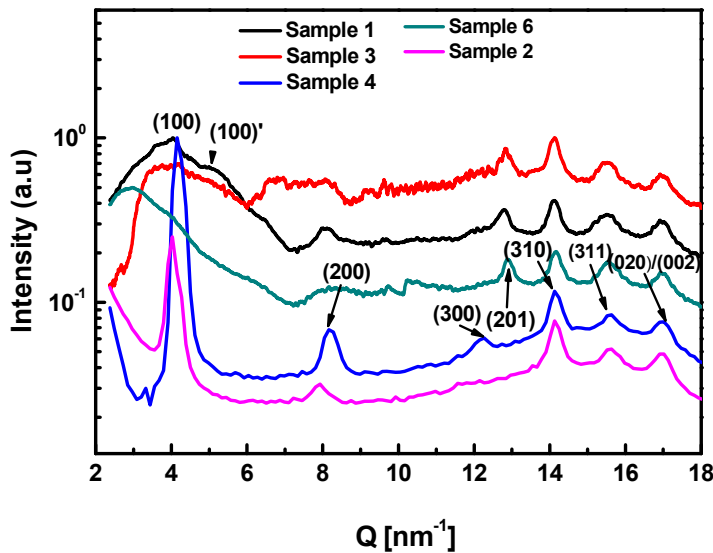


Figure 4.8 GOD scans for samples of different thicknesses. The incidence angle is $\alpha_i \leq \alpha_{cs}$. In low angle range the diffraction curves suffers from parasitic scattering of beam line components. For information in this Q-range refer to Figure 4.7.

In contrast to GID, the low order Bragg peaks appear for all samples independent from film thickness. This finding is in agreement with the image plate data shown in Fig. 4.6. As long as the nano-crystallites are randomly oriented the scattering provides closed Scherrer rings (Fig. 4.6a) and distinct low angle peaks are visible in GID (Fig. 4.8) and GOD (Fig. 4.8). Reducing the film thickness the low angle peaks in GID disappear but remains in GOD which is the situation shown in Fig. 4.6b.

However, there is a discrepancy in explaining the wide angle peaks missing in Fig. 4.6b but being clearly visible in Figs 4.7 and 4.8. This discrepancy can be explained by the different sensitivity of Delta and ESRF experiments. The orientation distribution of nanocrys-

tals contains two components; one is the preferential alignment of nanocrystals along the surface normal and the second is associated with the remaining, not aligned nanocrystals.

The ratio of both components is changing with decreasing the film thickness for the benefit of the aligned component. Due to the higher background scattering at Delta experiment the random component is no more visible in Fig. 4.6b but measurable in Figs. 4.7 and 4.8 taken at ESRF. Based on present data we cannot decide whether the non aligned component of orientation distribution is in fact random or perhaps bimodal, ones corresponding to edge-on and another to face-on orientation of crystallites with respect to the interface.

Based on data shown in Fig. 4.7 and 4.8 we have calculated the inter-planar distances, d_{100} and d_{020} , and the size of crystals, L_c , and summarized in Table 4.2. d_{100} and d_{020} remain constant in all scan directions and for all thicknesses within error bars. However, the present d_{100} values are smaller than that obtained from our previous powder measurements ($d_{100} = 1.58$ nm) [7]. Using Scherrer formula [3] we have computed the average size of crystals for the samples of different thickness. Using the width of the (100) peaks, the crystal size in that direction varies from 12 nm for sample #9 to 40 nm for the thickest film (sample #1).

4.7. Structure Model

Using all angular positions of peaks measured in GOD and GID scans, we evaluated an average unit cell of the nano-crystallites present within P3HT samples. For sample #1 we have found a larger number of peaks in both GOD and GID scans. For thinner films most of the peaks are still visible in GOD, but only one or two of the wide angle peaks remain in GID. This refers to a crystal structure of perfect crystallites which represents the particular low molecular weight fraction under investigation.

The peak positions found have not been matched with the assumption of an orthorhombic cell as suggested by Tashiro et al. [12], with $\mathbf{a} = 1.663$ nm, $\mathbf{b} = 0.775$ nm and $\mathbf{c} = 0.777$ nm. Multiples of (100) and one of both (020) and (002) were found by Kline et al. [13] only. Our experiment cannot be indexed by an orthorhombic cell. However, the number of structure peaks is still too small in order to find a unique structure solution. Our fits have considered the known $\pi - \pi$ distance of $\mathbf{b}/2 = 0.38$ nm. However, the unit cell can be triclinic or monoclinic. In present case several unit cells matches with the experimental data. Out of them we have used the unit having lattice parameters $\mathbf{a} = 1.59 \pm 0.02$ nm, $\mathbf{b} = 0.75 \pm 0.02$ nm, $\mathbf{c} = 0.76 \pm 0.02$ nm, $\beta = 101 \pm 3^\circ$ and $\alpha \approx \gamma \approx 90^\circ$ for further indexing. This cell is approximately monoclinic and not much different from the structure solution suggested by Brinkmann et al.

[11] and Prosa et al. [14] and which were extracted from material which differs from the low molecular weight fraction probed here. Based on this, our model corresponds to structure type I. A schematic scheme of the unit cell is shown in Fig. 4.9. Because the lattice parameters b and c are approximately same the peaks indexed with (020) and (002) may merge together. Because we are rather interested to investigate how the structure parameters change with film thickness we were not keen to find the best structure solution.

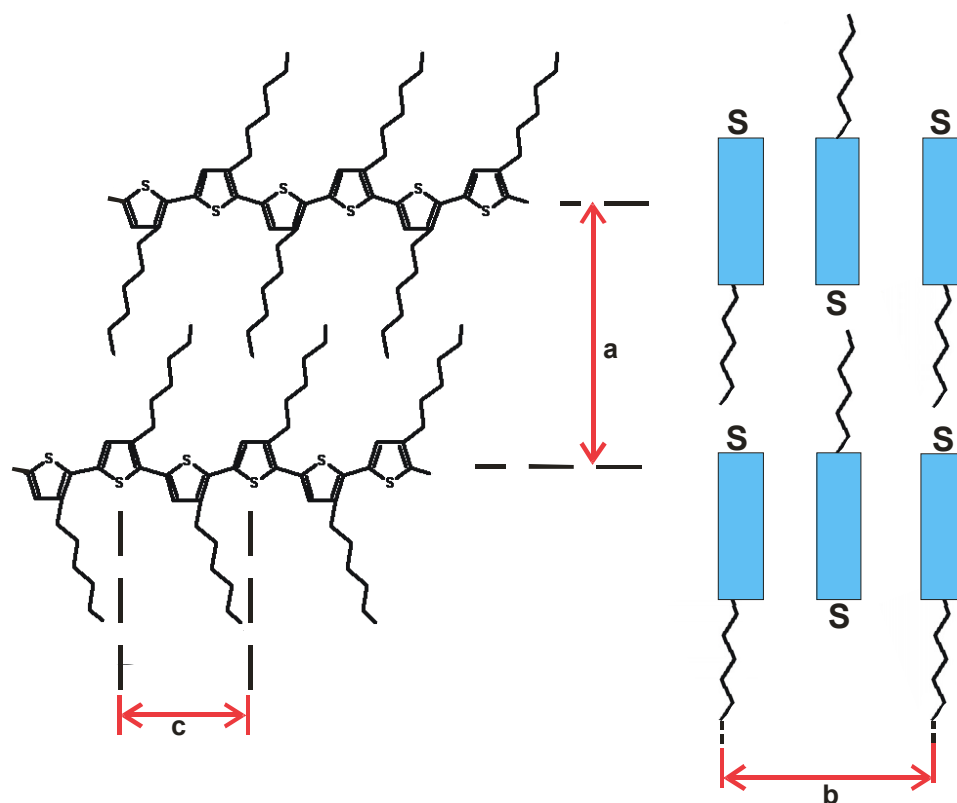


Figure.4.9 Evaluated monoclinic unit cell of LMW Poly(3-hexylthiophene) fraction.

4.8. Interface Induced Ordering

Fig. 4.10 show the GID scan of sample #3 taken at three different angles of incidence, changing from $\alpha_i = 0.10^\circ$ to 0.12° , where $\alpha_i \leq \alpha_{cs}$. Whereas in the first case X-rays penetrate the top region of the film only, the other cases probe the whole film. Two peaks are visible – (100) and (020), increasing in intensity for increasing α_i . At same time the intensity of the amorphous halo around $Q_{xy} = 16.0 \text{ nm}^{-1}$ increases as well which is identified by scattering from SiO_2 . At the same time the halo at $Q_{xy} = 11.0 \text{ nm}^{-1}$ is not affected. One can see the improvement of in-plane ordering as the angle of incidence increases. All gives evidence that the crystal peaks are mainly caused by crystallites located at the film to insulator interface and the in-plane ordering maintained throughout the film thickness.

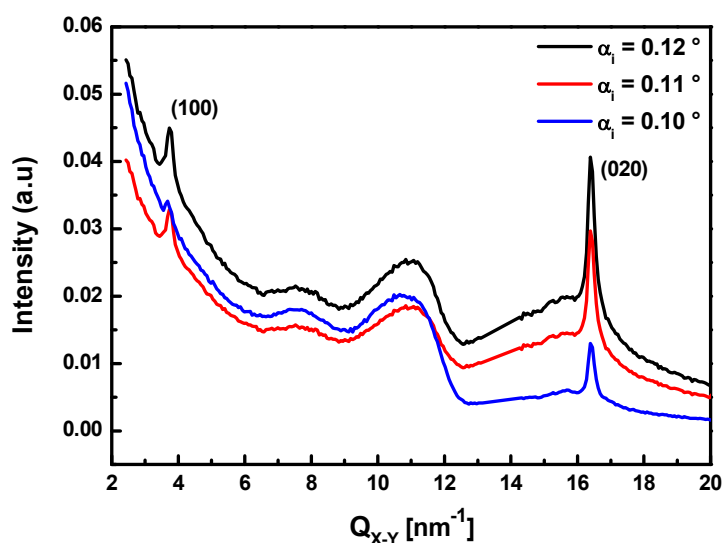


Figure 4.10 In-plane measurements of sample #3 at three different α_i , corresponding to a probe of the surface and the whole film, respectively.

4.9. Discussion

Based on the AFM, TEM and GID and GOD studies at room temperature, there is a direct indication of the thickness dependence of crystallinity and structural ordering and its orientation in low molecular weight (ethyl-acetate) fraction P3HT. We have shown that the crystalline order of films made of LMW fraction changes as a function of film thickness. For film thicknesses above 200 nm the film structure consists of randomly oriented nanocrystallites of 25 - 40 nm size diluted in an amorphous matrix (Fig. 4.6a). Decreasing the film thickness the main change of morphology consists in narrowing the distribution of crystal orientation (Fig. 4.6b). Using the ratio between the total amount of scattering intensity under Bragg peaks and that under amorphous halos one can make an estimate of the degree of crystallinity. In contrast to powder samples [9] such estimate for thin films contains several uncertainties. Our data for thin films extracted from line scans (only along surface normal direction) following the Ruland's method [15] indicates the increase in degree of crystallinity with decreasing molecular weight like the powder samples [9].

Finally, one has to note that the ESRF measurements have provided a better understanding of structural order in thin films of low weight P3HT. In terms of ordering we found two components; one aligned and another random in orientation. In terms of crystal structure the larger number of Bragg peaks, in principle, would allow a better structure solution. However, the number of peaks found is still too small for a unique structure solution which holds

for most of the structures published in literature. Structure solution of P3HT powders [7, 12] provided (100) and (020) peaks which were indexed using respective stereo-chemical arguments from powder data published by, Tashiro [12], Prosa [10, 14] and Meille [16]. The best structure solution for low molecular weight P3HT was published by Brinkmann et al. [11] recently. Unfortunately, it cannot be transferred to our material due to the film formation from a different solvent and slightly larger molecular weight of the P3HT that was used in their study. The refined crystal structure is assumed to be the best fit solution over the whole sample. The lattice parameters might slightly vary among the crystals and probably change at the film-substrate interface. The later one could explain that a few peaks appeared in GID or GOD only. This is supported by the polymorphism which appeared at thick pristine films only. It reflects the effect of small fluctuation of crystal growth energy during the preparation process.

Recently, Kline et al.; precisely commented up on the interdigitation of side chains in P3HT as well as for di-block copolymer combination of P3HT. From the combined measurements of XRD, polarized IR transmission spectroscopy and Near edge X-ray fine structure spectroscopy they pointed out that the side chains of copolymers of poly(alkylthiophenes) can and do interdigitate substantially, whereas they do not interdigitate for poly(alkylthiophenes) only, the side chain interdigitation provides a mechanism for three-dimensional ordering; without it, poly(alkylthiophenes) are limited to small domains and poor performance. They have also claimed the alkyl-side chains tilt from the surface normal is 56° . Under our prediction based on our current results, the molecular packing is such that the thiophene rings are arranged more or less parallel to each other defining the lattice parameter b . Our current measurements indicate that the side chains are partially interdigitating, currently we cannot comment up to what extent is this interdigitation (disordered or partially or fully interdigitated) and how much the side chains tilted with surface normal, as no single technique can determine the interdigitation of alkyl side chains but the presence of three orders of (100) peak along surface normal direction, as well as presence of (hk0) and (hkl) peaks indicates the partially presence of three-dimensional ordering of these molecules, this cannot possible without any extent of side chain interdigitation. This is also supported by the presence of polymorphism II form, where the side chains are perfectly normal to surface with increased b spacing, which hints for presence of interdigitation under this II form [17].

Further, each second chain attached to a thiophene ring aligns into same direction. The degree of interdigitating defines the stacking distance (lattice parameter a). The distance along a single thiophene backbone (lattice parameter c) is very close to the distance to the neighbor-

ing thiophene backbones. Due to the alternative arrangement of chains, c is the distance between two second consecutive thiophene rings (Fig. 4.9). Similar arguments hold for b , it measures the distance between two subsequent backbones assuming that two neighbored thiophene rings are shifted by $c/2$ to each other. Following the model of Prosa et al. [10, 14] the aliphatic chains are tilted by a certain angle (β - angle) with respect to the thiophene rings. A local disorder of side chain alignment may result due to the appearance of the repetition units along the polymer backbone and it might be change the alignment of thiophene rings to each other as seen by a change in angles between axes and the diffuse scattering hump at $Q_{xy} = 1.6 \text{ \AA}^{-1}$.

In general, we have shown the room temperature studies of LMW P3HT, where the thickness dependence is essential for the understanding of structural properties of the thin layers. The pinning effect starts dominating when the size of crystals become in the range of film thickness, from where the orientation ordering starts dominating.

Here, one must note that the above described structures for LMW fraction is the as grown structure, which particularly depends on the growth conditions and the substrate treatment. It does not reflect the structure at equilibrium condition, for which one needs the annealing or stepwise heating. Under next chapter we will show that annealing is an important step to bring such structural morphology into equilibrium position.

4.10. References

- [1]. Samori, P.; Francke, V.; Mangel, T.; Muellen, K.; Rabe, J. P. *Opt. Mater.*, 9, 390, 1998.
- [2]. Kline, R. J.; McGehee, M. D.; Kdnikova, E. N.; Liu, J.; Frechet, J. M. J. *Adv. Mater.*, 15, 1519, 2003.
- [3]. Yang, C.; Orfino, F. P.; Holdcroft, S.; *Macromolecules*, 29, 6510-6517, 1996.
- [4]. U. Pietsch, V. Holy, T. Baumbach, *High-resolution X-ray diffraction from thin films and lateral nanostructures*, Springer, Berlin, 2005.
- [5]. R. J. Kline, M. D. McGehee, M. F. Toney, *Nature Mat.* 5, 222, 2006.
- [6]. T. J. Prosa, M. J. Winokur, J. Moulton, P. Smith, A. J. Heeger, *Macromolecules*, 25, 4364, 1992.
- [7]. A. Zen, J. Pflaum, S. Hirschmann, W. Zhuang, F. Jaiser, U. Asawapirom, J. P. Rabe, U. Scherf, D. Neher, *Adv. Funct. Mater.*, 14, 757, 2004.
- [8]. Sirringhaus, H.; Brown, P. J.; Friend, R. H.; Nielsen, M. M.; Bechgaard, K.; Langeveld-Voss, B. M. W.; Spiering, A. J. H.; Janssen, R. A. J.; Meijer, E. W.; Herwig, P. T.; de Leeuw, D. M.; *Nature*, 401, 685-688, 1999.
- [9]. Zen, A.; Saphiannikova, M.; Neher, D.; Grenzer, J.; Grigorian, S.; Pietsch, U.; Asawapirom, U.; Janietz, S.; Scherf, U.; Lieberwirth, I., Wegner, G.; *Macromolecules* 39, 2162-2171, 2006.
- [10]. Prosa, T. J.; Winokur, M. J.; Moulton, J.; Smith, P.; Heeger, A. J., *Macromolecules* 25, 4364-4372, 1992.
- [11]. Brinkmann, M.; Rannou, P.; *Adv. Funct. Mater.*, 17, 101-108, 2007.
- [12]. Tashiro, K.; Keiko, O.; Yasuhisa, M.; Masamichi, K.; Tsuyoshi K.; Katsumi, Y.; *J. poly. Sci.: Part B: Poly. Phys.*, 29, 1223-1233, 1991.
- [13]. Kline, R. J.; McGehee, M. D.; Kadnikova, E. N.; Liu, J.; Frechet, J. M. J.; Toney, M. F.; *Macromolecules*, 38, 3312-3319, 2005.
- [14]. Prosa, T. J.; Winokur, M. J.; McCullough R. D.; *Macromolecules*, 29, 3654-3656, 1996.
- [15]. W Ruland, *Acta Cryst.*, 14, 1180, 1961.
- [16]. S. V. Meille, V. Romita, T. Caronna, *Macromolecules*, 30, 7898, 1997.
- [17]. Kline, R. J.; DeLongchamp, D. M.; Fischer, D. A.; Lin, E. K.; Richter, L. J.; Chabiny, M. L.; Toney, M. F.; Heeney, M.; McCulloch, I.; *Macromolecules*, 40, 7960, 2008.

Chapter 5

Temperature Dependent Structural and Crystallinity Studies of LMW Poly(3-hexylthiophene) by X-ray Diffraction Methods

As we know, the morphology of thin films at the polymer-to-insulator interface is of great importance for OFET applications. In order to access this polymer-substrate interface we have prepared samples of varying thickness. We have performed grazing-incidence X-ray diffraction and field effect mobility measurements to correlated the thickness dependence of structural order and the electrical parameters in low molecular weight ($M_w \sim 2.5$ kDa) poly(3-hexylthiophene) (P3HT).

At the same time to understand the interface nature, improvement of crystallinity as well as recrystallization mechanism and excess of this information at the any length scale of film thickness we have carried out the temperature dependent in-plane and out-of-plane X-ray diffraction measurements, which helped us to understand the surface-interface nature for bulk to thin films as well as provide the information about structure improvement which ultimately gives idea about degree of crystallinity before and after heating. As it is well know that the samples prepared through spin-coating technique are not thermodynamically stable, simply due to less spinning time. Therefore, annealing can play their important role to improve the surface structure ultimately the mobility of the system. At the same time temperature dependent studies supported our pinning model where the size of crystals matters – when the size of crystallites becomes in order of film thickness ~ 25 nm, there is a preferential alignment of the molecules along the surface normal direction.

The recent studies on low molecular weight P3HT did not provide sufficient information on the effect of layer thickness on morphology and mobility. Jia et al. [1] have shown the thickness effect on the performance of high molecular weight P3HT-based (98.5% regioregular) OFET devices. They found that the mobility and the drain current increase with respect to thickness. The on-off ratio decreases and saturates for thicknesses above 60 nm. As these observations are purely based on device characteristics, they cannot give a clear hint on the thickness-dependent structural order variation inside the individual films. Therefore, a systematic study of the crystalline structure as a function of film thickness in P3HT is still desirable. This will also provide the information on the particular film structure close to the inter-

face of the gate insulator since the first few monolayers close to the gate oxide are mostly responsible for the efficient charge flow from source to drain inside the active channel region [2]. On the other side, in contrast to X-ray measurements the field effect mobility is found to be constant within the whole investigated range. Our findings give evidence that the charge transport in low molecular weight P3HT is dominated by the ultrathin layer stabilized at the film-to-insulator interface. Despite the very uniform orientation of the crystallites within this layer, the field effect mobility remains low for all thicknesses. This is attributed to the presence of amorphous regions between highly crystalline domains, which ultimately limits the charge transport in the layer plane.

From the last chapter, we have already seen some of these properties as stated above for the LMW fraction of P3HT at room temperature utilising the AFM, TEM and X-ray diffraction measurements. Our findings based on AFM, TEM & X-ray measurements suggest that the thin film of low molecular weight fraction samples consist of highly ordered crystallites embedded in an amorphous matrix having the “ribbon” like morphology [3]. LMW molecules are short and tend to adopt a twisted disordered conformation.

In this chapter we present X-ray investigations of the structure and its thermal behaviour of low molecular weight P3HT films in relation to charge carrier mobility measured with respective thin film OFETs. At first glance our work has been focused on systematic study of structure and its relation to electrical properties of the films as a function of film thickness for mainly HMDS coated SiO₂/Si substrate. We will show that the higher crystalline ordering found for thin films compared to the bulk one does not result in higher carrier mobility as long as the nanocrystals are separated by large amorphous regions.

5.1. Sample Preparation and Measurements Details

All the sample preparation steps were well explained under chapter 3 and chapter 4. All X-ray measurements were performed under vacuum conditions ($\sim 10^{-3}$ mbar) using the conventional DHS 900 domed hot stage (Fig. 3.4) provided by Anton Paar GmbH, Graz, Austria. For temperature-resolved measurements the temperature has been increased in steps of 10 °C from room temperature up to the melting point of the individual sample with an accuracy of $\pm 0.5^\circ$. Data were taken after stabilization of the respective temperature on the sample surface.

5.2. Temperature Dependent Reflectivity Measurements

Temperature dependent thickness variation of thinnest film (1 mg/ml) samples were measured by X-ray reflectivity from the angular separation of Kiessig fringes for all elevated temperatures. The thickness was determined via fitting the reflectivity curve using the XOP programme, provided by ESRF based on Parratt formalism, the calculated thickness at room temperature was 17 nm. At the same time to understand better about the thin film morphology, roughness with respect of temperature increment we have done the series of reflectivity measurements for various temperatures from room temperature up to the melting point of the LMW fractioned polymer and all reflectivity scans fitted via XOP programme (Fig. 5.1a-b), all the values obtained after fitting (Fig. 5.1c) are summarize in table 5.1. One can see that the P3HT-SiO₂ interface roughness and film thickness are increasing as the temperature increases, while Air-P3HT roughness is almost constant.

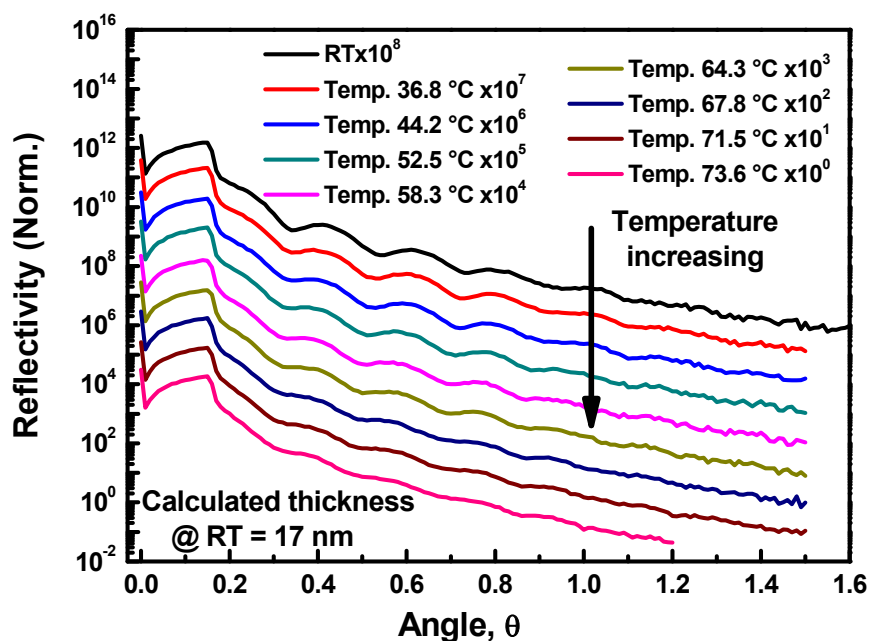


Figure 5.1a Temperature dependent reflectivity measurements performed at Delta synchrotron source for thinnest film of thickness 17 nm. For better clarity each scan is multiplied by factor of 10.

Finally the 35 % film thickness increased around melting point (23.1 nm) comparison of thickness at room temperature (17 nm). From Fig. 5.1b one can see that at the temperature (58.5 °C) there is a sharp change of slop, this point can be considered as the glass-transition temperature of the polymer from where the solid thin film converted to much soft and rubbery state.

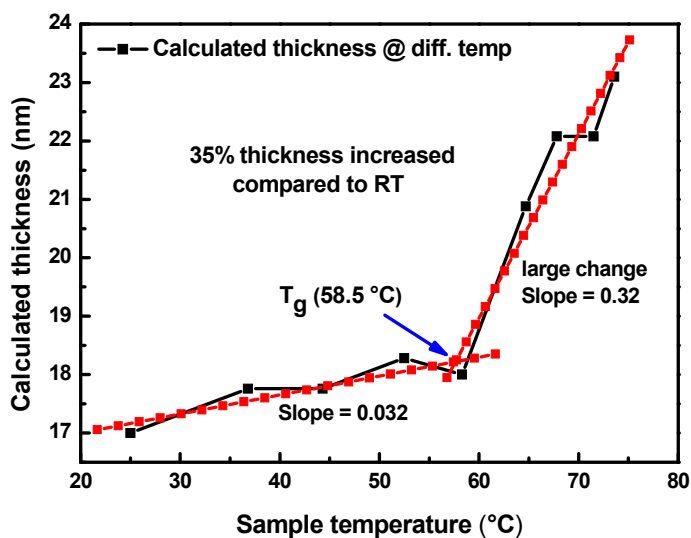


Figure 5.1b Temperature dependent thickness variation using the reflectivity measurements, the abrupt increase of thickness at 60 ° indicates the T_g temperature of sample.

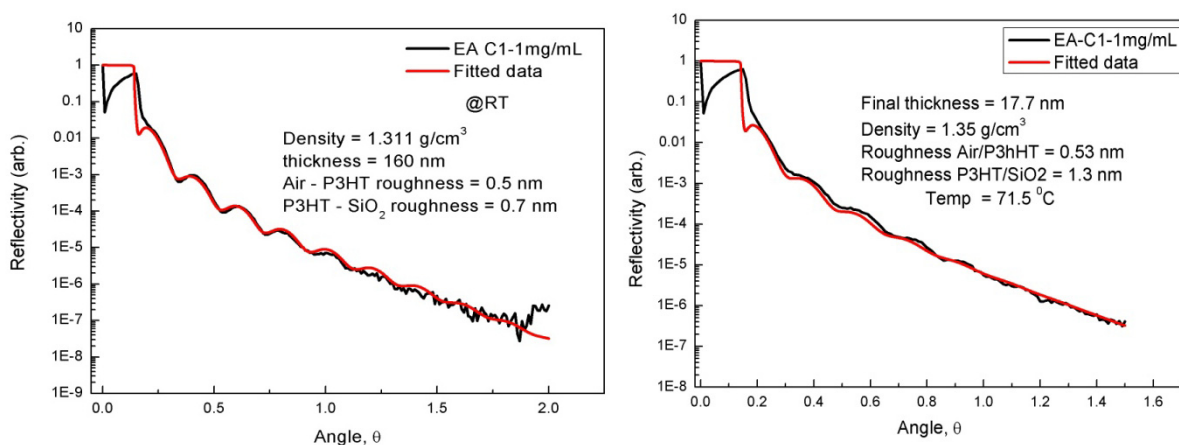


Figure 5.1c Temperature dependent reflectivity curve fitting using Parrat formalism (a) for room temperature, (b) at elevated temperature 71.5 ° C.

Temperature °C	Thickness nm	Air-P3HT Roughness (nm)	P3HT-SiO ₂ Roughness (nm)	Density g/cm ³
RT	16.0	0.48	0.70	1.353
58.3	16.5	0.50	0.80	1.350
71.5	17.7	0.53	1.30	1.350

Table 5.1 Computed values from fitting of various reflectivity scans at elevated temperatures.

In general the findings on temperature dependent reflectivity measurements are in agreement with the similar results published by Werzer et al. [4]. They have done temperature dependent X-ray diffraction and reflectivity measurements for rr- P3HT of molecular weight (M_w) = 45,000 g/mol at the various temperatures. They have also observed an increase of the (100) lattice spacing associated with an increase of total film thickness of 15%. The FWHM of the peak was decreasing and the intensity was increasing up to 150 °C, followed by decrease of intensity, and a complete disappearance at 200° C. The less thickness expansion in case of Werzer et al. could be due to high molecular weight, as due to high molecular weight and long chain length these molecules are less mobile or not very kinetically active, where as the effect is vice versa in case of low molecular.

5.3. Structure Investigation as a Function of Temperature

There are no systemic temperature studies done on P3HT, except for high molecular weight fraction observed by Werzer et al. [4], P3HT films were not systematically inspected at varied temperatures above room temperature. However, technically most of the films were treated by an annealing step to improve the film quality only [3, 5]. X-ray diffraction measurements have been performed between room temperature and about 100 °C using stepwise heating. All measurements performed after reaching the stable temperature on top of sample surface. At the same time slow cooling has done but with in time limit of 30 minutes, due to the limited beamtime periods and number of samples. The cooling rate was 4 °C/min.

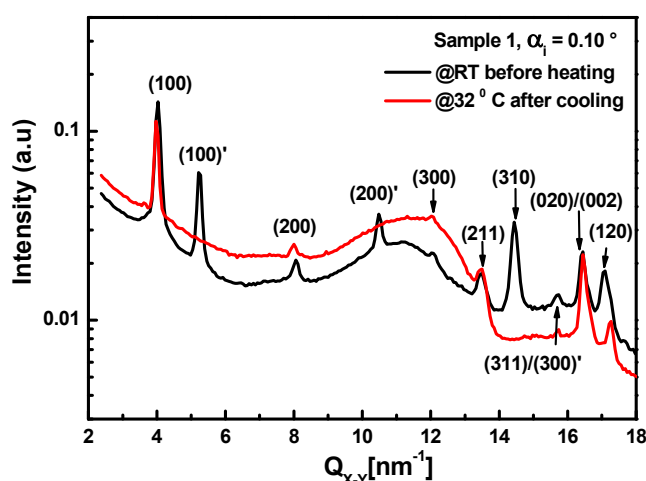


Figure 5.2 Temperature dependent study of sample #1 at $\alpha_i \leq \alpha_{cs}$. The polymorphism of the pristine sample disappears after the heating cycle.

Fig. 5.2 shows the GID scans of sample #1 before and after heating above 100 °C. The mentioned polymorphism or dual form is only present in the pristine sample at room temperature. After the heating cycle the structure with 'd₁₀₀'=1.20 nm disappeared indicating that the 2nd polymorph form is thermodynamically less stable compared with the 1st one with d₁₀₀ = 1.56 nm.

At the same time the peak at Q_{xy}= 14.4 nm⁻¹ also disappeared accompanied by a change in the intensity ratio of both amorphous halos. At the same time peak (020) has improved in intensity and there is sharp reduce of background around it, indicates the improvement of in-plane ordering. All others peaks are not much affected except of change in intensity of background scattering. This indicates that the crystal structure is maintained after annealing.

5.4. Influence of Film - Substrate Interaction & Thermal Expansion

5.4.1 For Out-of-Plane – (100) Peak / Thermal Expansion

Fig. 5.3a show the temperature dependence (100) peak behavior measured for sample #1 under GOD geometry. One can see that when the temperature increases, the (100) reflection shift to lower Q values accompanied by a decrease of peak intensity. This trend is continuous up to the complete disappearance of the peak. The temperature of complete disappearance can be associated with the melting point of the ethyl-acetate fraction of P3HT.

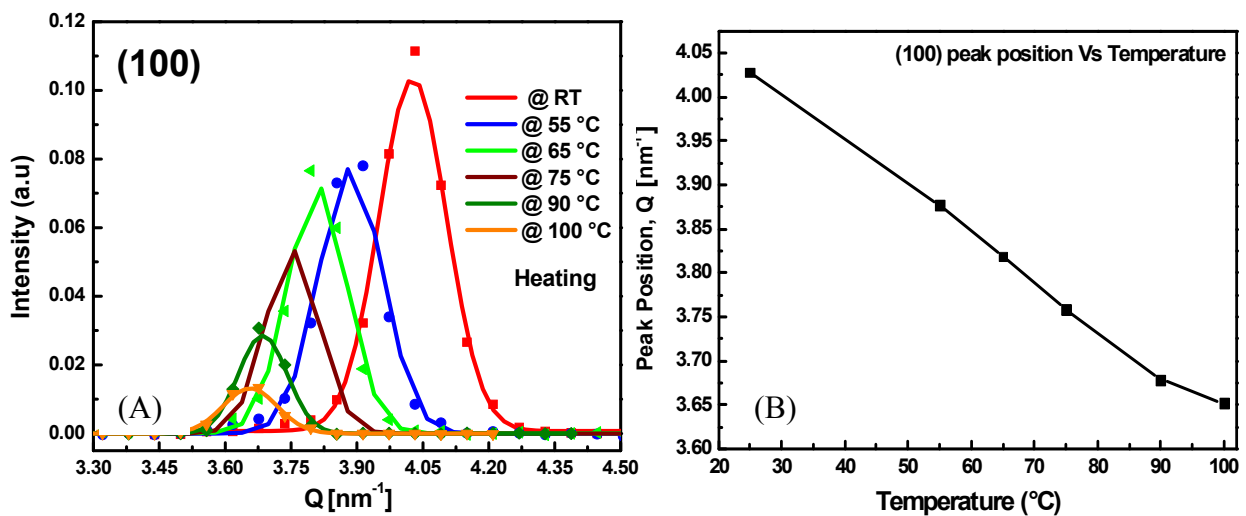


Figure 5.3a Temperature dependence of the (100) peak studied for sample #1 at $\alpha_i \leq \alpha_{cs}$ and the corresponding position shift in Q space, the peak shifting towards lower Q indicates the increase of 'd' spacing along normal direction.

Fig. 5.3b shows the temperature dependent variation of the (100) peak intensity measured by GOD scan for four samples of different thickness measured at ESRF. It shows a continuous decrease in intensity versus temperature for sample #1 and #3 but nearly constant intensity for the thinner sample #5 ($t=27$ nm) up to about 75 °C followed by a sharp drop. The same behavior was found for another sample similar to sample #6 of this series but at a different experiment performed at Delta. This much thinner sample ($t=10$ nm) exhibits a sharp drop of (100) intensity at 70 °C. This behavior shows that the substrate-layer interaction becoming remarkable for thin films only. The interaction also modifies the character of phase transition. It appears to be continuous decrease of intensity for thick films but sharp decrease of intensity for thin films. This can be explained by the strong substrate layer interaction between the nanocrystals pinned at the insulator interface for thin films. In thick films, melting of crystal may start at the film surface and proceed down to the interface of the film where the interactions are stronger and thus the melting temperature higher, as found for systems with interface melting [6].

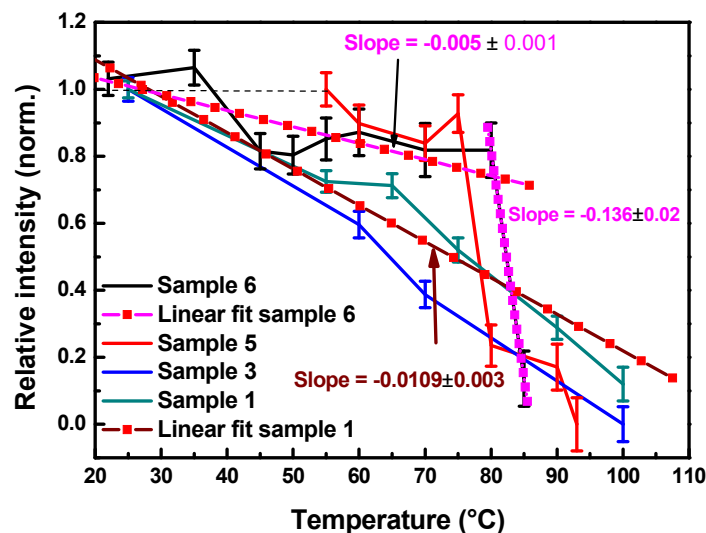


Figure 5.3b Temperature dependent relative intensity studies of thick and thin films measured at ESRF. The sample shown in black was measured at Delta.

This behavior differs from thin layers with a sharp melting temperature. To understand further features of the thermal expansion, we have plotted the inter-planar distance ' d_{100} ' versus temperature. As seen in Fig.5.3c the both thin and thicker film shows the same increase of d_{100} between room temperature and about 80 °C but rather large error bars. The calculated (100) peak position thermal variation coefficient is 2.515×10^{-4} . At the same time their calculated inter-planar distance thermal expansion coefficients for bulk films (~ 200 nm), thin film

(17 nm) and thinnest film (11 nm) are as follows 1.35×10^{-3} , 1.62×10^{-3} and $1.22 \times 10^{-3} \text{ T}^{-1}$. This is almost constant for bulk as well as thin films.

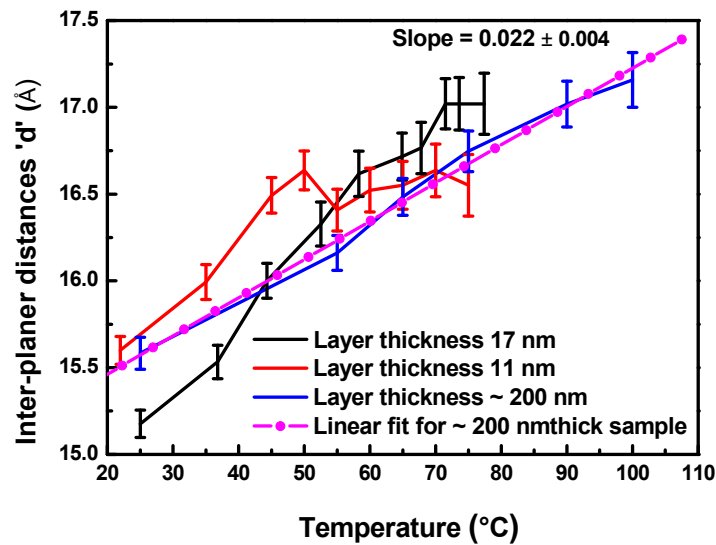


Figure 5.3c Temperature dependent inter-planer distances 'd' of three samples with different thickness.

5.4.2. For In-Plane – (020) Peak / Thermal Contraction

Figs. 5.4a-b show the temperature dependence contraction of (020) reflections measured for sample #1 in GID geometry, respectively. From Fig. 5.5a one can see that when the temperature increases, the (020) reflection shift towards higher Q values accompanied by a decrease of peak intensity.

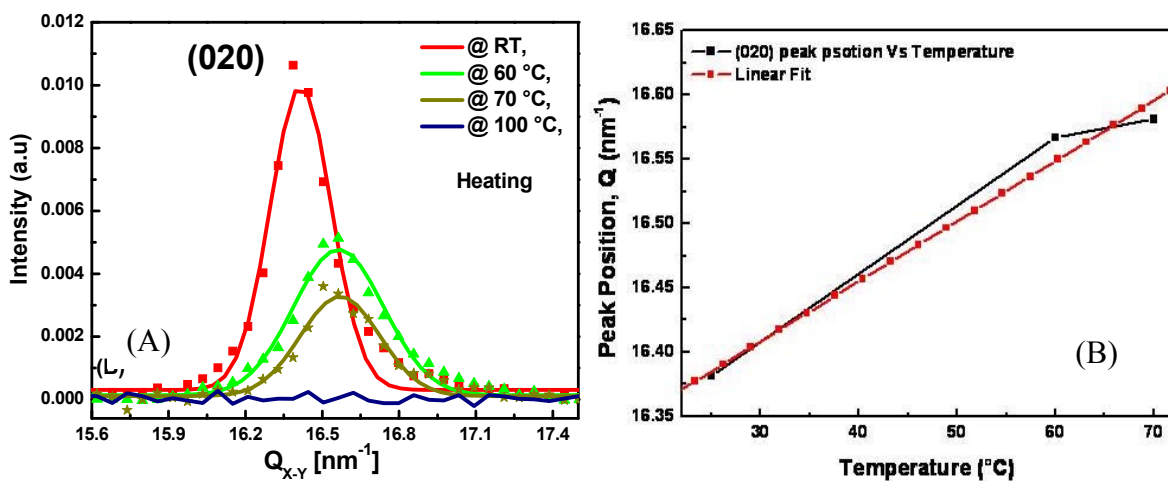


Figure 5.4 (a) Temperature dependence of (020) peak studied at sample #3 at $\alpha_i \leq \alpha_{cs}$. The shift of (020) peak towards higher Q_{x-y} value indicate the decrease of 'd' spacing lateral direction, (b) shows the (020) peak position variation with temperature increase.

This trend is continuous up to the complete disappearance of the peak intensity. At the same time, the (020) peak positions shift towards higher Q_{xy} values as the temperature increases, indicating a decreasing of d_{020} spacing, i.e. a reduction of the π - π distance. The calculated (020) peak position thermal variation coefficient is 2.145×10^{-4} , it is similar order like (100) peak position expansion.

In combined, increase of temperature gives rise to an expansion of the nano-crystals along the axis of alkyl-chains (**a** direction) accompanied by a contraction of π - π -distance (**b** direction). After cooling down the lattice deformation is almost reversed.

5.5. Mobility Measurements.

Field effect mobility measurements have been performed for samples with different thickness to correlate the structural parameters with electrical properties. The corresponding output and transfer characteristics display a remarkable hysteresis. Linear and saturation regions are quite blurred and unstable. To minimize these hysteresis effects, we have averaged the forward and back scans of the output characteristics for every gate bias. OFET mobilities as calculated from the gate-bias dependence of the averaged saturation current and plotted in Fig.5.5.

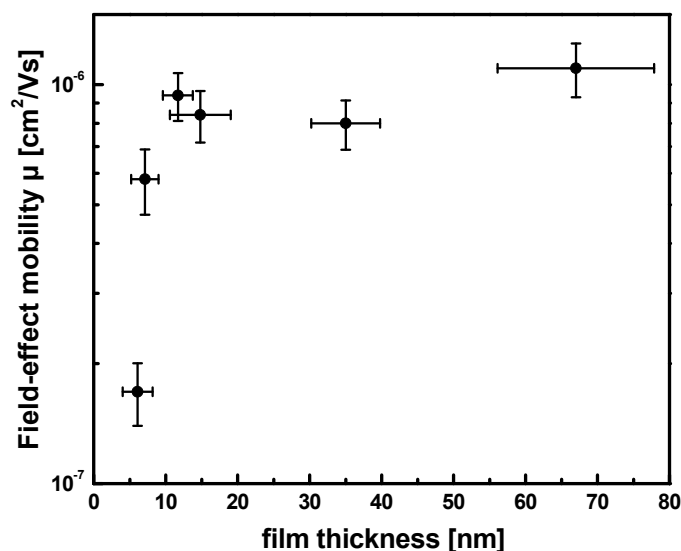


Figure 5.5 Thickness dependent field-effect mobility of low molecular weight P3HT, extracted from the OFET output characteristics (I_{DS} vs. V_{DS} at fixed V_{GS}).

Except for the thinnest film, the field-effect mobility remains almost constant within the wide range of thicknesses, with an average mobility of ca. $10^{-6} \text{ cm}^2/\text{Vs}$. Fluctuations

within 20% can be related to varying experimental conditions. Particular AFM inspections at the thinnest film (Fig. 5.6) gave hint for incomplete wetting which seems to be the reason for the much lower field effect mobility of LMW thin film sample compared to the thick film. When comparing the results from X-rays and OFET thickness dependent measurements one should keep in mind, that the thickness determination with a surface profiler (as used to determine the polymer layer thickness in the transistor structures) underestimates the true thickness. For thin layers, the thickness values measured with the profiler are approximately half of those obtained from the analysis of the Kiessig-fringes. This can be explained by the compression of the soft polymer by the probe of the profiler.

We further, observed that the field-effect mobility increases by the factor of two by annealing the polymer layer for 5 min at 55 °C, as compared to the pristine device, which was left in a vacuum for 5 h to remove residual solvent from the film. The pristine sample has a field-effect mobility of $(4.1 \pm 0.6) \times 10^{-7} \text{ cm}^2/\text{Vs}$ (film thickness $18.3 \pm 1.6 \text{ nm}$ as determined with a surface profiler) the mobility of the annealed sample was $(9.5 \pm 1.3) \times 10^{-7} \text{ cm}^2/\text{Vs}$ (for a comparable film thickness of $23.5 \pm 2.4 \text{ nm}$).

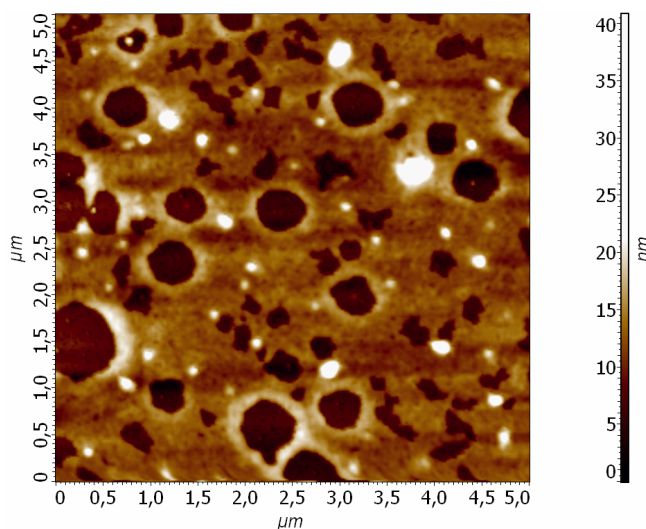


Figure 5.6 Dewetting effect found for thin films of LMW P3HT fraction.

5.6. Discussion

As we have already discussed the LMW P3HT properties at room temperature in chapter 4. Considering all together now and summarizing all, we can say

Our results directly indicate the thickness dependence of crystallinity and structural ordering and its orientation in low molecular weight (ethyl-acetate) fraction P3HT. We have

shown that the crystalline order of films made of P3HT changes as a function of film thickness.

For films with thicknesses in the order of few 100 nm the film structure consists of randomly oriented nanocrystallites diluted in an amorphous matrix (chapter 4, Fig. 4.6a). Decreasing the film thickness the main change of morphology consists in narrowing the distribution of crystal orientation (chapter 4, Fig. 4.6b). Following the suggestion by Kline et al. [7] this is explained by a preferential alignment of crystals at the film-to-insulator interface. Kline et al. [7] verified their assumption by the very narrow width of (100) rocking curves for thin films. We found evidence by at least three different experiments: Using α_i resolved measurements we have shown that the crystal peak intensities and scattering from the interface increases with respect to penetration depth of probing X-ray with the sample independent from whether the film was prepared either on HMDS or OTS coated SiO₂/Si substrates. In addition we have shown that the melting behaviour of the films changes qualitatively by decreasing the film thickness. Finally, we found direct pictures of the changing orientation distribution by imaging of 2D scattering. Moreover, using highly intense synchrotron radiation of ESRF we could determine the orientation of the pinned nanocrystals.

For films below about 25 nm, we find a drop of (100) peak intensity in GID which is not observed in GOD. The disappearance of (100) peaks in GID can be interpreted by a preferential alignment of the **a**-axis of nanocrystals parallel to the film normal which corresponds to an “edge-on“ geometry. Considering the average crystalline size listed in Table 4.2 (chapter 4), the change in alignment appears when the domain size equals to the film thickness. The effect of interface alignment is known from liquid crystals [8] and decays exponentially from the interface towards the bulk. It looks like that the thin LMW films behave like smectic phase of liquid crystals while the thick films as nematic phase. The interface alignment might also be essential for polymers at interfaces as well. The particular control of the interface effect via surface engineering could help for a better understanding of thickness dependence of mobility.

About the comparison of electronic and structural properties, we have found that the mobility remains constant over a wide range of thicknesses, despite of a significant increase in in-plane ordering when decreasing the layer thickness, as revealed by our X-ray measurements. Based on our structural and electrical properties we presume the existence of an interface-near ultrathin crystalline layer, stabilized by the strong interaction between the polymer chains and the gate insulator, with the main chains oriented almost exclusively parallel to the substrate. This interface region is present in all samples but dominates for samples of having

thickness about ~ 25 nm, and it is responsible for charge transport in OFET devices. Despite this high structural order, the mobility of carriers remains quite low. As pointed out in the introduction, several authors provided evidence for the existence of amorphous regions in between highly-crystalline lamellae (or nanofibrils) in short chain P3HT samples, even in films grown by epitaxial solidification. It is, therefore, plausible to propose that such inter-lamellar zones also exist in those highly-ordered ultrathin layers stabilized very close to the gate insulator and they ultimately determine the charge transport in OFETs made from LMW P3HT.

The drop in mobility has found when decreasing the layer thickness ~ 10 nm (see Fig.5.5), it could be that P3HT film partially dewets below a critical layer thickness as shown in Fig. 5.6. Although these very thin layers are characterized by a high degree of chain alignment, with low degree of orientation disorder.

We did not observe any significant effect of SiO₂ surface treatment on the layer morphology, nor on the transport properties of our low molecular weight material. The carrier mobilities reported here are much lower than those published by Kline et al. [7] for short chain P3HT on OTS, though our X-ray measurements reveal a high structural order of the layer stabilized at the semiconductor-insulator interface. To solve this obvious discrepancy, a comparative investigation of the polymer samples used by other laboratories would be needed (which is beyond the scope of this thesis), but we like to point out again that the low mobility measured in this study is in accordance with the generally accepted structural model for short chain P3HT, as outlined above.

Our X-ray studies on as-prepared layers show that the presence of a second metastable polymorph (phase II), which disappears upon annealing. The concurrent increase in mobility of annealed samples suggests that the mobility of carriers in this metastable phase II is quite lower. This lower mobility is probably due to the larger in-plane π - π stacking distance of polythiophene layers and lower rate for interchain hopping.

We have already shown the monoclinic unit cell structure of such P3HT nano-size crystallites (chapter 4), this is to be an average over the whole sample. We found a complete change of crystal unit cell with increasing temperature. Moreover, the phase transition between solid and melt changes as a function of thickness. It is found to be continuous drop of intensity for thick films, but sharp drop for thinner films. The layer thickness where we found a change in the temperature behaviour first gives a rough estimate for the decay length of interface interaction towards the bulk. Because the peaks width remains constant while decreasing in intensity, the numbers of crystallites decrease with increasing temperature for film

thickness above the interface decay length. The crystals dissolve and the amorphous film which melts as a whole. This differs from thin films where the crystals kept pinned at the film-substrate interface up to the melting temperature. Due to the interface interaction the later one is expected to change as a function of film thickness.

In summary, LMW fraction has shown some adventitious structure properties and even quiet large size of crystallites. Such LMW fraction is good for studying the structural properties of semi-crystalline class of polymeric material. Unusually, LMW P3HT fraction has shown very limited charge carrier mobility values ($\sim 10^{-5} \text{ cm}^2\text{V}^{-1}\text{s}^{-1}$), where crystallites are embedded in an amorphous matrix and block the charge to flow from source to drain.

Due to this deficiency, we have further considered and studied the HMW fraction of P3HT as for device application it is more suitable class of material having the mobility in range of $\sim 10^{-2} \text{ cm}^2\text{V}^{-1}\text{s}^{-1}$ then LMW fraction. Therefore our further studies will be based on HMW fraction structural studies and how to modify or improve its structure which will ultimately increase the charge carrier mobility, one of the decisive parameter of device performance.

5.7. References

- [1]. Jia, H.; Srinivas, G.; Pant, G. K.; Wallace R. M.; Gnade, B. E.; *J. Vacuum Sci. & Tech. A.*, 24, 1228-1232, 2006.
- [2]. Tanase, C.; Meijer, E. J.; Blom, P. W. M.; de Leeuw, D. M.; *Org. Electron.*, 4, 33-37, 2003.
- [3]. Zen, A.; Pflaum, J.; Hirschmann, S.; Zhuang, W.; Jaiser, F.; Asawapirom, U.; Rabe, J. P.; Scherf, U.; Neher, D.; *Adv. Funct. Mater.*, 14, 757-764, 2004.
- [4]. Werzer, O., Matoy, K., Strohriegl, P., Resel, R. *Thin Solid Films*, 515, 5601-5605, 2007.
- [5]. Zen, A.; Saphiannikova, M.; Neher, D.; Grenzer, J.; Grigorian, S.; Pietsch, U.; Asawapirom, U.; Janietz, S.; Scherf, U.; Lieberwirth, I., Wegner, G.; *Macromolecules*, 39, 2162-2171, 2006
- [6]. Petermann, J.; Gleiter, H.; *J. Polym. Science*, 14, 555-558, 2003.
- [7]. Kline, R. J.; McGehee, M. D.; Toney, M. F.; *Nature Mat.*, 5, 222-228, 2006.
- [8]. Gennes, P. G.; Prost, J.; *The physics of liquid crystals*, 2nd ed.; Birman, S.; Edwards, S. F.; Llewellyn, C. H.; Rees, S. M.; Oxford University press: New York, Vol. 10, p 507, 1993.
- [9]. Tashiro, K.; Keiko, O.; Yasuhisa, M.; Masamichi, K.; Tsuyoshi K.; Katsumi, Y.; *J. poly. Sci.: Part B: Poly. Phys.*, 29, 1223-1233, 1991.
- [10]. Prosa, T. J.; Winokur, M. J.; Moulton, J.; Smith, P.; Heeger, A. J., *Macromolecules*, 25, 4364-4372, 1992.
- [11]. Brinkmann, M.; Rannou, P.; *Adv. Funct. Mater.*, 17, 101-108, 2007.
- [12]. Meille, S. V.; Romita, V.; Caronna, T.; *Macromolecules*, 30, 7898-7905, 1997.

Chapter 6

Room Temperature Based X-ray Structure and Crystallinity Studies of HMW Poly(3-hexylthiophene)

This chapter reporting about crystalline structure of spin coated thin films of high molecular weight (HMW) regioregular poly(3-hexylthiophene) (P3HT) ($M_n \sim 30,000$) at room temperature. The structural behaviour again for HMW thin and thick films are strongly dependent on film thickness like the LMW fraction. Our results indicate different growth mechanism for thick as well as thin films.

Our room temperature HMW fraction studies based on exploiting the typical surface-interface techniques i.e. Atomic force microscopy (AFM), Transmission Electron Microscopy (TEM) and X-ray scattering techniques particularly, X-ray diffraction methods utilising the grazing incidence geometry (GOD and GID scans). X-ray diffraction studies are our primarily focussed those were well supported by AFM and TEM as secondary techniques.

Here, X-ray diffraction studies were performed in order to understand the distribution of crystallinity along the whole thickness of film, the molecular orientation and the nanoscale morphology of HMW fraction of Poly (3-hexylthiophene) (P3HT) thin films. To understand further surface-interface induced film morphology and ordering, we have exploited different kinds of dielectric layers, mainly HMDS, OTS and bare SiO_2 . To understand the thickness effect only two kinds of samples prepared by utilising different dielectric layers basically are bulk films having thickness ~ 200 nm and the ultrathin films of having thickness ~ 10 nm. Further structural information was obtained by employing the X-ray grazing incidence in-plane and out-of-plane diffraction using synchrotron radiation. The X-ray analysis reveals that the films are mainly amorphous and contain randomly oriented nanocrystallites with the best match for a monoclinic unit cell. Interestingly, the film morphology varies as a function of film thickness. Similarly like LMW, HMW fraction also shows the random orientation of nanocrystallites changes to preferential orientation of lamellae along the surface normal, when the size of crystallites becomes of the order of film thickness, i.e. ~ 20 nm.

6.1. Sample Preparation

All the samples prepared by spin coating technique, which is described in detailed in chapter 3. The molecular weight explored of HMW P3HT is $M_n = 30,000$ g/mol, $M_w = 40,000$

g/mol, having the polydispersity (M_w/M_n) = 1.32 where the number of thiophene rings were 151 and the length of molecule is 64 nm. All these macromolecular parameters derived from Gel Permeation Chromatography (GPC) technique are summarized in table 6.1. To understand the thickness dependent behaviour we have prepared number of samples of varying thickness. Interface dependent behaviour has been studied by varying the dielectric layer between the sample and the substrate (chapter 3, Fig. 3.7). All the samples have been analyzed and the results are summarized in table 6.2. The first substrate was untreated or bare SiO₂/Si. The other two were Hexamethyldisilazane (HMDS) and Octadecyltrichlorosilane (OTS), [1, 2] coated SiO₂/Si substrates, respectively. To vary the thickness of the polymer layer, the concentration of P3HT in chloroform solution was varied; and produced the samples of having concentration 1 mg/ml & 40 mg/ml only.



Figure 6.1 Systemic demonstrations of 3 kinds of sample preparation for HMW fraction study.

Compound	M_n / g/mol	M_w / g/mol	PD	DP	L [nm]
Concentration (thickness) = 40 mg/ml ~ 200 nm (thick films) 1 mg/ml ~ 10 nm (thin films)					
P3HT chloroform fraction	30,000	40,000	1.32	151	64

Table 6.1 All the macromolecular parameter derived for HMW Poly(3-hexylthiophene).

6.2. Atomic Force Microscopy (AFM) Studies

The morphology of as prepared layers from the chloroform fraction of P3HT has been studied using AFM. Samples prepared from the chloroform fraction exhibit a granular morphology or isotropic nodule like structure (Fig. 6.2 a-b) having the size of crystallites 10 ± 2 nm. In general the findings on as-prepared layers are in agreement with the results of AFM

studies published by Kline et al. [3]. The AFM measurements provide the image of the top surface. At the same time we must keep in mind that most of the charge-carriers in an organic device is carried within approximately ~ 5 -10 nm of the interface with the gate dielectric [4]. Parallel to it, our XRD measurements reveal that the type of crystalline order that prevails throughout the film, while the AFM measurements show only top surface morphological images. It probably hints for the presence of similar morphology along the whole range of thickness, even at the bottom interface, however, we cannot rule out the possibility that interactions with the substrate lead to a different structure at the bottom interface.

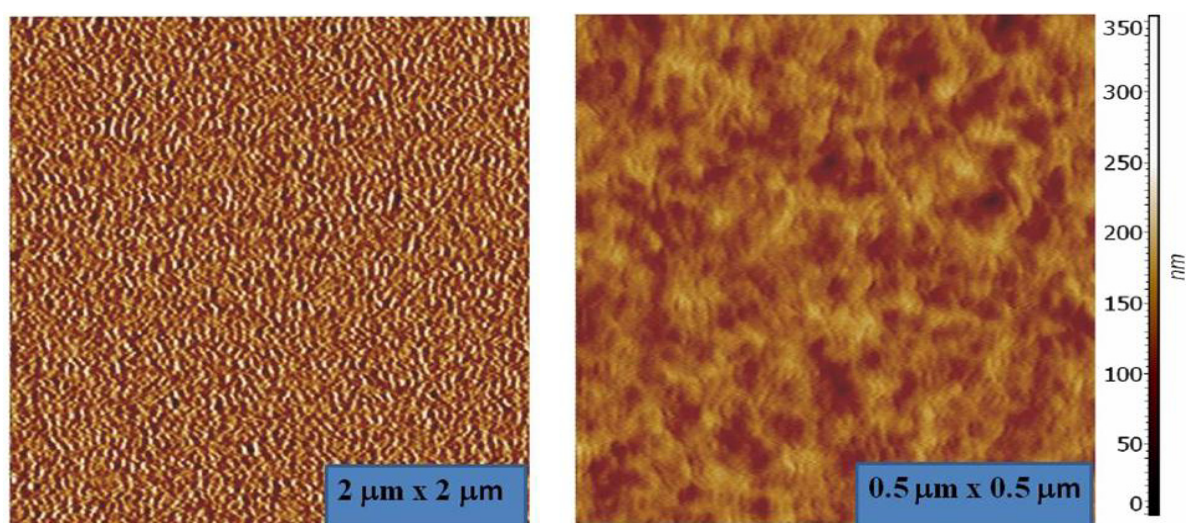


Figure 6.2a-b Tapping mode atomic force microscopy (AFM) images of a HMW fraction of P3HT having molecular weight (M_w) = 30,000 g/mol, (a) Phase image, (b) topography image [15].

6.3. Transmission Electron Microscopy Study

Figure 6.3a shows the TEM images from the chloroform fraction measured at 150 °C to avoid the sample damage using electron beam. The AFM image (Fig. 6.2a-b) shows a nodule-like structure and the BF micrograph (Fig. 6.3a) shows small crystallites (white spots). In order to identify the crystalline character of this fraction, we recorded the electron diffraction pattern (Fig. 6.3b), which revealed a diffuse ring pattern.

In fact, it has been published in the literature that semicrystalline material will produce a diffraction pattern in TEM consisting continuous ring, while small and imperfect crystallites will show a fuzzy ring [5]. Our TEM measurements inflect support to our AFM measurements.

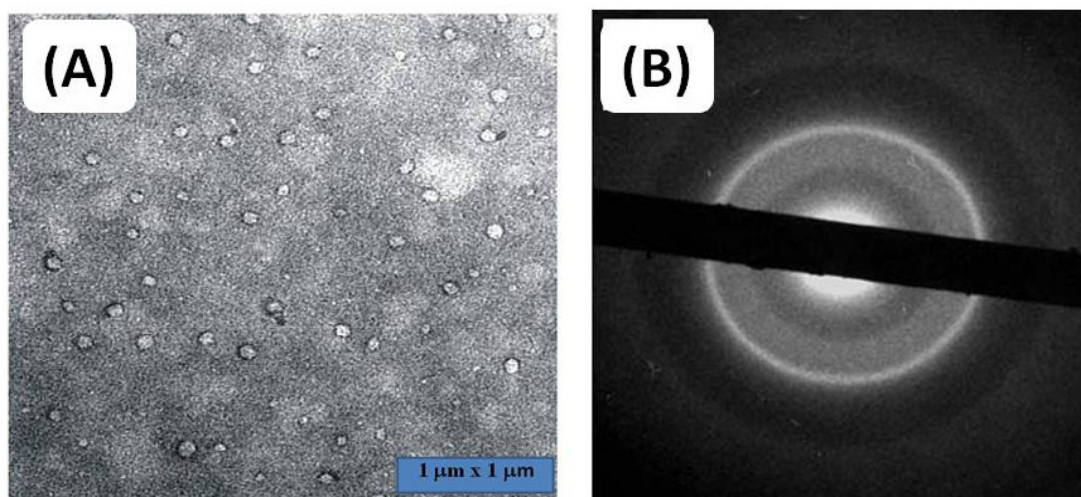


Figure 6.3 (A) TEM bright field image of the HMW fraction of P3HT, the measurement was performed at 150 °C to avoid damage of the layers due to the electron beam, (B) TEM diffraction pattern [15].

S.N.	Samples	Thickness t , (nm)	d_{100} (nm)	Crystallite Size L_c (nm)
#1	40 mg/ml on HMDS	No thickness oscillation found	1.64 ± 0.02	9.0 ± 1.0
#2	40 mg/ml on OTS	No thickness oscillation found	1.64 ± 0.02	9.7 ± 1.0
#3	40 mg/ml on Si/SiO ₂	No thickness oscillation found	1.63 ± 0.02	9.0 ± 1.0
#4	1 mg/ml on HMDS	11 ± 0.5	1.73 ± 0.02	9.2 ± 1.1
#5	1 mg/ml on OTS	12 ± 1	1.63 ± 0.02	9.05 ± 1.1
#6	1mg/ml on Si/SiO ₂	11 ± 1	1.70 ± 0.02	8.2 ± 1.4

Table.6.2 Calculated thickness and structural properties of crystallites of P3HT samples at room temperature.

6.4. Determination of Layer Thickness

X-ray reflectivity measurements were performed to determine the film thicknesses. Fig. 6.4 shows the results of the reflectivity measurements of the samples prepared from different solution concentrations 1 mg/ml and 40 mg/ml, which describe as thin and bulk films. Due to interference of waves reflected from the vacuum-sample and film-substrate interfaces,

Kiessig fringes are clearly visible. The film thickness, t , was obtained from the distance ΔQ_z between two consecutive maxima, where $t = 2\pi/\Delta Q_z$. Except for the thickest sample, thin film sample shows a large number of Kiessig fringes which verify the homogeneity of the film thickness and fluctuates by only about 3 nm within the illuminated sample area. The extracted film thickness values are shown in Table 6.2.

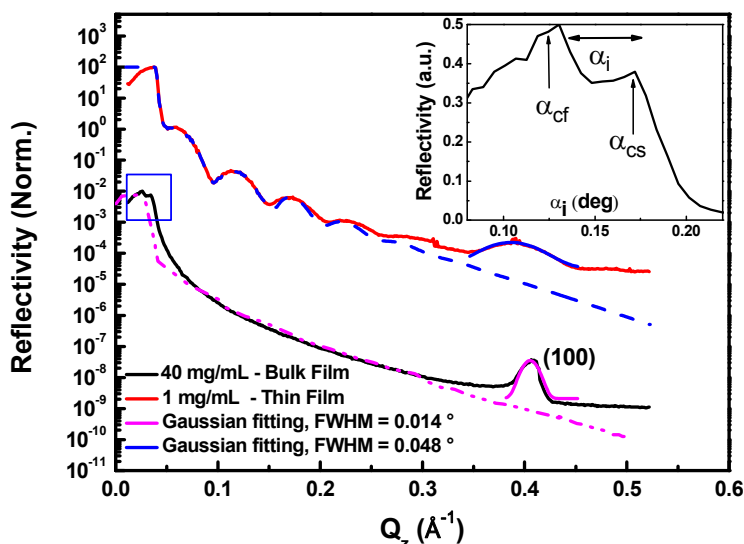


Figure 6.4 Reflectivity measurements of HMW P3HT of bulk and thin film samples. The inset shows the angular region of total external reflection of bulk sample. Further GID and GOD scans were recorded setting the incidence angle α_i to $\alpha_{cf} < \alpha_i < \alpha_{cs}$, where α_{cf} and α_{cs} are the angle of total external reflection of film and substrate, respectively. All the dashed lines correspond to reflectivity fitting curves using XOP program.

Considering the relation between concentration and film thickness of the other samples the thickness of sample #1 was estimated to be $t \approx 200$ nm. The bulk sample displays the two critical angles, α_{cf} and α_{cs} , very well (see inset of Fig. 6.4). Following this critical angle criteria the incidence angle, α_i , was fixed under condition $\alpha_{cf} < \alpha_i < \alpha_{cs}$, for both GOD and GID. At the same time Fig. 6.5 shows the comparison of thin films (1mg/ml) of HMW P3HTs having different dielectric layers beneath of polymer films. Their calculated thicknesses are around 10 nm average.

The reflectivity scans can be extended up to the first Bragg peak indexed by (100) and utilizing the Scherrer's equation [6, 7], the measured FWHM of the (100) peak was used to determine the correlation length, L_c , parallel to surface normal, also identified as the crystallite size in this direction and it is listed in Table 6.2.

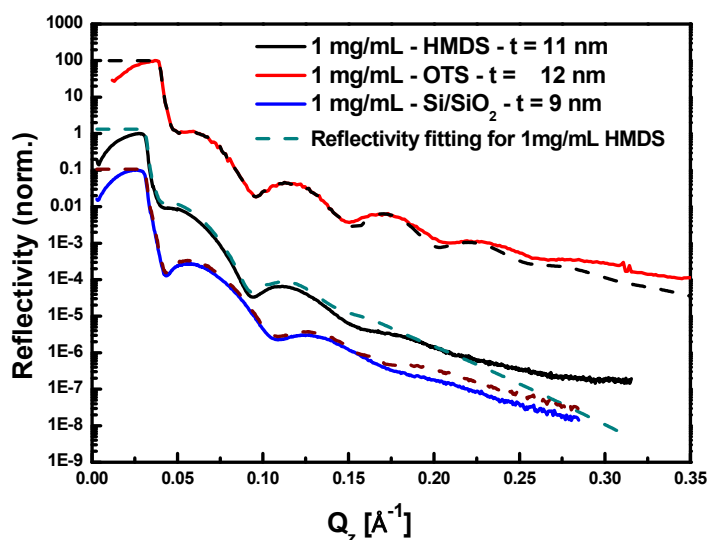


Figure 6.5 Comparison of reflectivity scans for thin films of HMW P3HTs layers of having same concentration, 1 mg/ml but different dielectric layers. For better clarity individual scans are multiplied by the factor 10. All the dashed lines correspond to reflectivity fitting curves using XOP program.

6.5. Differential Scanning Calorimetry

Figure 6.6 shows the DSC thermogram from powder samples prepared from the HMW P3HT chloroform fractions. The systematic heating was done with constant heating rate of 10 K/min. Melting and crystallization temperatures were determined by considering the peak values of the second heating and cooling scans, respectively.

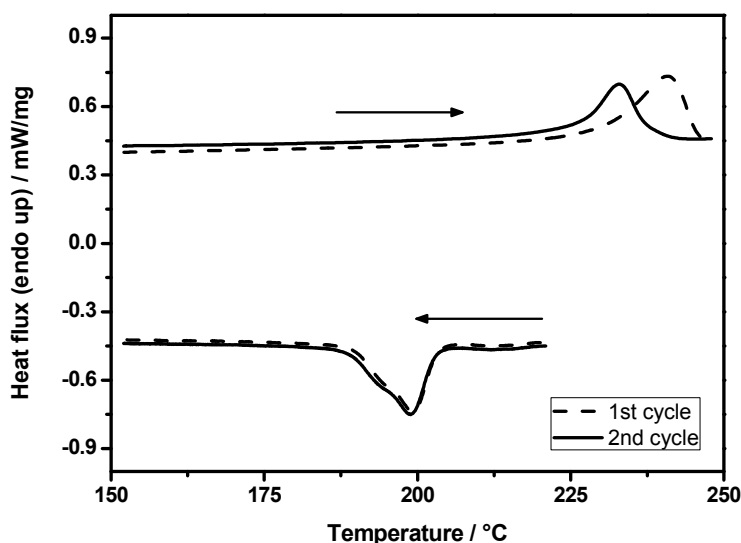


Figure 6.6 DSC thermograms measured from solution-crystallized sample of chloroform fraction. The dashed and solid lines refer to the first and second heating/cooling cycles, respectively.

Our experiments give the evidence of the structural changes, the structure appears at elevated temperature is better ordered compared to at RT. For technologically relevant films of HMW P3HT with thickness larger than 100 nm both structural parameters are best at a temperature close to 200 °C. As shown by the DSC diagram in Figure 6.6, melting and crystallization properties of our batch are typical for regioregular P3HT with an endothermic melting peak at ca. 235 °C upon heating and exothermic crystallization at ca. 190 °C [9]. Following the arguments in Malik et al. [10] the bulk melting point should be ca. 225 °C. Thus, the structural changes as disclosed by our X-ray studies occur at significant lower temperatures as the melting of the polymer crystals. One second interesting observation is that the (020) reflection stays well visible even at 260 °C, this supports our bi-model phase behavior.

6.6. X-ray Grazing Incidence Diffraction Studies

For the detailed study of the structural properties of HMW fraction thin films ($t \sim 10\text{--}200$ nm) grazing incidence diffraction techniques (GID and GOD) [11] have been employed, which are explained in detail in chapter 2. All the data are in well agreement with the literature values [8, 12-15]. The scattering scheme is also shown in chapter 3, Fig. 3.4.

The X-ray diffraction measurements were carried out using synchrotron radiation at BW2 at Hasylab/Desy, Hamburg, Germany, using a wavelength $\lambda = 1.24$ Å, at BL9 station of Delta ($\lambda = 0.8267$ Å) and at ID10b of ESRF ($\lambda = 0.8236$ Å). At Delta we used an Image plate with 3450x3450 pixels of 100 μm size spaced at 43 cm from the sample probed with a beam size of 0.5x1.5 mm². At ESRF we used a CCD camera with 2048x2048 pixels of 65 μm size set at 30 cm from the sample. Here the beam size was 0.1x0.3 mm². A pixel detector was used at Hasylab. In all measurements the incident angle and the angle of exit within the incident plane are α_i and α_f , resp., and the in-plane scattering angle is 2θ . For comparison all angular coordinates are transformed into Q-space [9].

6.6.1. Image Plate Measurements

The typical structures of as-grown samples of HMW fraction on HMDS as well as OTS modified SiO₂/Si substrates are shown in Fig. 6.7 recorded by image plate exposure at room temperature. Thick sample (~ 200 nm) shows the typical ring structure of wide angle reflections. In addition, out-of plane (h00) peaks appeared with certain angular distribution increasing with increasing h. One can also see the textured appearance of (310) peak for HMDS modified substrate, while (020) in-plane peak, which is in general a lateral contribu-

tion of structure completely absent. Whereas OTS is showing complete Debye-Scherrer rings patterns for (020) set of planes as well as preferentially oriented (310) and (100) set of planes. The preferential orientation of (100) set of planes along normal direction indicate the alky-side chains orientation along normal direction and preferential edge-on orientation dominates on flat-on orientation. The appeared (310) peak as a textured along normal direction for HMDS coated SiO_2/Si substrate, clearly shows the difference of surface mediated interaction of HMDS and OTS dielectric layers. Whereas due to the broad orientation of (310) peak, (211) and (301) peaks appeared in vicinity of it have merged with the individual intensity of (310), due to which the (310) peak appeared sharper than (100) set of planes.

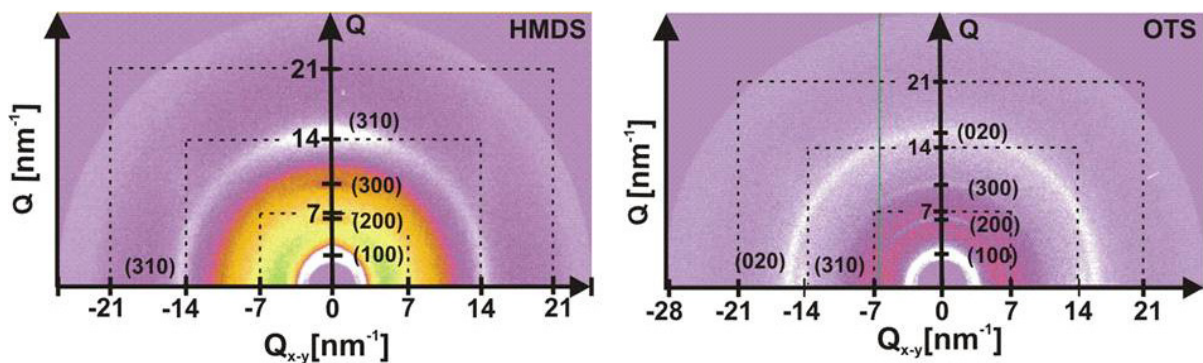


Figure. 6.7 Image plate measurements of pristine sample of thickest films (~ 200 nm) on top of (a) HMDS coated SiO_2/Si substrate, (b) OTS coated SiO_2/Si substrate for $\alpha_i = 0.10^\circ$.

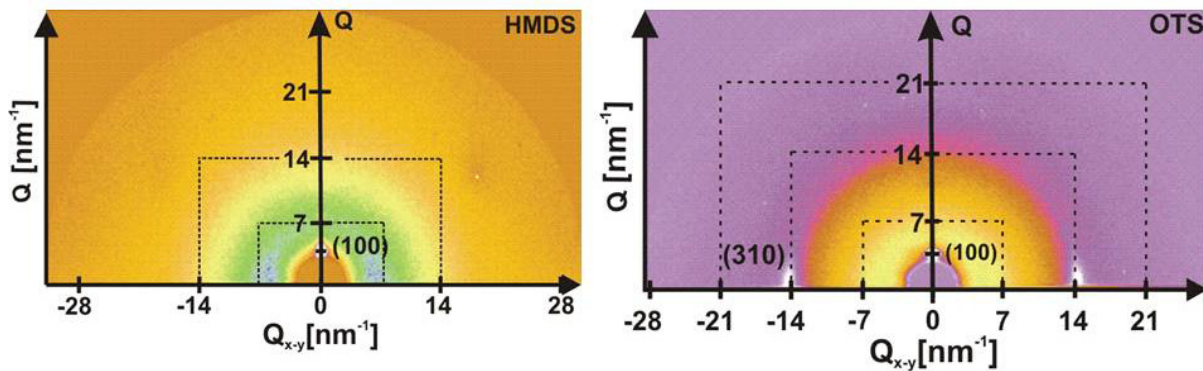


Figure. 6.8 Image plate measurements of as prepared sample of thinnest films (~ 10 nm) on top of (a) HMDS coated SiO_2/Si substrate, (b) OTS coated SiO_2/Si substrate for $\alpha_i = 0.10^\circ$.

In contrast to this, thinnest sample (~ 10 nm) does not provide any angular distribution (absent of rings) and present of diffraction spots along normal to surface directions clearly indicate the aligned out-of plane (h00) reflections, whereas under OTS coated SiO_2/Si substrate, there is also in-plane (310) peak, could be due to non parallelism of main chain, indicating the 3D orientation of crystallites and the crystallites are aligned at the film–substrate interface (Fig. 6.8). At the same time, considering both image plate measurements (Figs. 6.7

and 6.8) the different image patterns appeared for HMDS and OTS coated SiO₂/Si substrate directly indicate that for as prepared samples, OTS coated SiO₂/Si substrates provide the better structure formation at the interface level.

6.6.2. Grazing Incidence Out-of-Plane Diffraction

Following, the grazing incidence out-of-plane geometry shown in Fig. 3.4 (chapter 3), we have performed the OOP scans under the grazing incidence condition. Fig. 6.9 shows the typical OOP diffractogram for HMW fraction on top of HMDS coated SiO₂/Si substrate for thickest sample ~ 200 nm. The angle of incidence was fixed at $\alpha_i = 0.15^\circ$ was under the condition $\alpha_{cf} < \alpha_i < \alpha_{cs}$. The presence of (100) set of planes indicates the strong ordering along normal direction of substrate. The intensity ratio of (100) peak to (020) peak resembles the

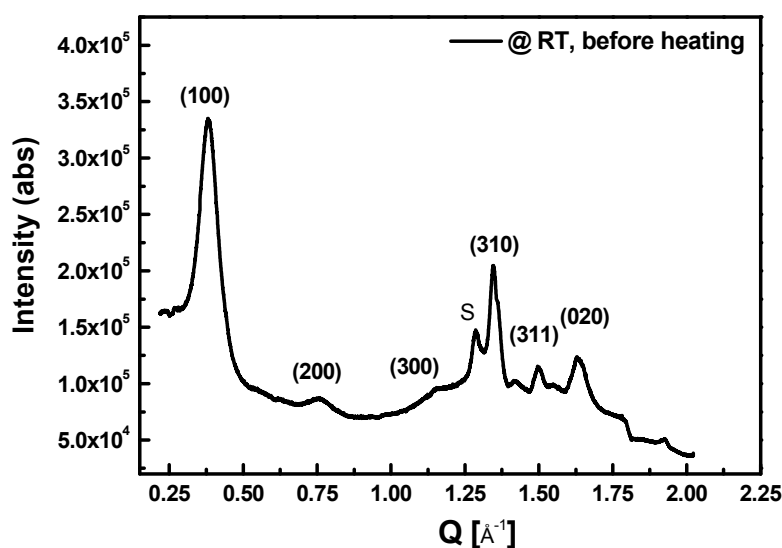


Figure 6.9 Out-of-plane scan measurement for thickest film ~ 200 nm for $\alpha_i = 0.15^\circ$ at Hasylab.

preferred edge-on orientation compared to flat on. At the same time presence of the rest peaks indicate the random orientation of crystallites along the normal direction. The appearance of (020) peak which is typical characteristics of GID scan, indicates that there are alkyl chains lying along the in-plane direction, which will typically hinders the charge flow along the in-plane direction. Fig. 6.10 shows the comparison of all three dielectric layers HMDS, OTS and bare SiO₂/Si for OOP scans of thick films of thickness ~ 200 nm. One can see clearly that for as spun samples the OOP patterns are almost same but comparing the (100) peak intensities indicate the highest intensity dominating by OTS coated SiO₂/Si substrate followed by HMDS and SiO₂/Si substrates having almost same intensity. It could be the indication that OTS di-

electric layer provides the best molecular packing at the interface level which ultimately enhanced the intensity of OTS sample. Whereas, still the presence of multiple peaks except of (100) and (020) indicates the domination of randomly oriented crystallites.

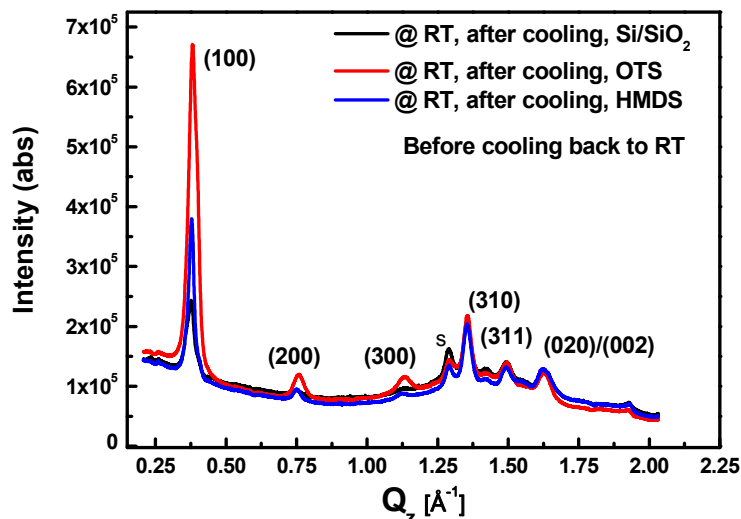


Figure 6.10 Comparison of OOP scans for samples of film thickness ~ 200 nm for $\alpha_i = 0.15^\circ$ on top three different modified substrate (HMDS; OTS & bare silicon dielectric layers).

Figure 6.11 shows the OOP scan for thinnest sample of thickness ~ 10 nm. One can clearly see the differences between the thick and thin films by comparing the Figs. 6.9 and 6.11. The (100) peak in thin film is almost disappear and there is huge domination of (020) and (310) peaks in thin film OOP scan compared to thick film. This could be due to less material and it could also indicates the dominance of flat-on orientation than edge-on orientation for as prepared samples (Fig. 1.9) where the molecules reorganised itself due to strong surface interface interaction coming from dielectric layers and in between thiophene molecules, where now the alkyl chains appear parallel to the substrate and π - π stacking come up along the surface normal direction (Fig. 1.9). The appearance of (310) peak found for image plate as well as for point detector. The (310) peak more dominating for thin films compared to thick films.

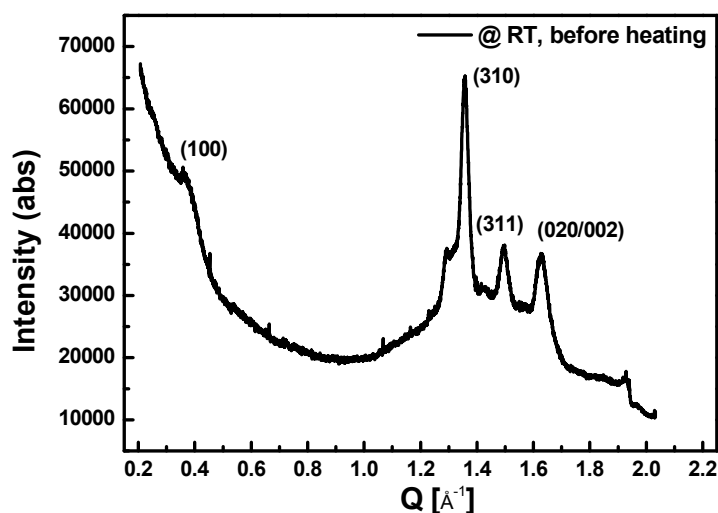


Figure 6.11 Out-of-plane scan measurement for thinnest film ~ 10 nm for $\alpha_i = 0.15^\circ$ at Hasyllab.

6.6.3. Grazing Incidence Diffraction (GID)

Typical, In-plane scans for HMW fraction of thick and thin films have shown under figures 6.12 and 6.13. Almost both scans are identical except of the intensity variation.

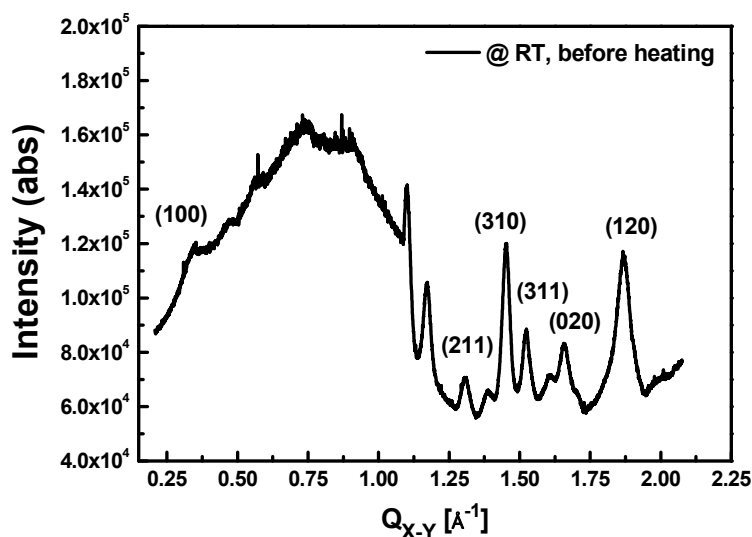


Figure 6.12 In-plane measurement for HMW P3HT thick film on top of HMDS coated SiO_2/Si substrate for as spun sample at $\alpha_i = 0.15^\circ$.

One can see the almost absents of (100) peak along in-plane direction. This indicates the least presence of alkyl-side chains along in-plane molecular packing direction. At the same time presence of multiple peaks still indicate the in-plane random distribution of crystal-

lites in both kinds of samples. With this, there is a huge domination of amorphous scattering at the $Q_{x-y} = 0.75 \text{ \AA}^{-1}$. Again, (310) peak dominating more in in-plane scans than out-of-plane scan. This shows their presence giving more impact in in-plane ordering, which might influence and further distort the (020) in-plane stacking.

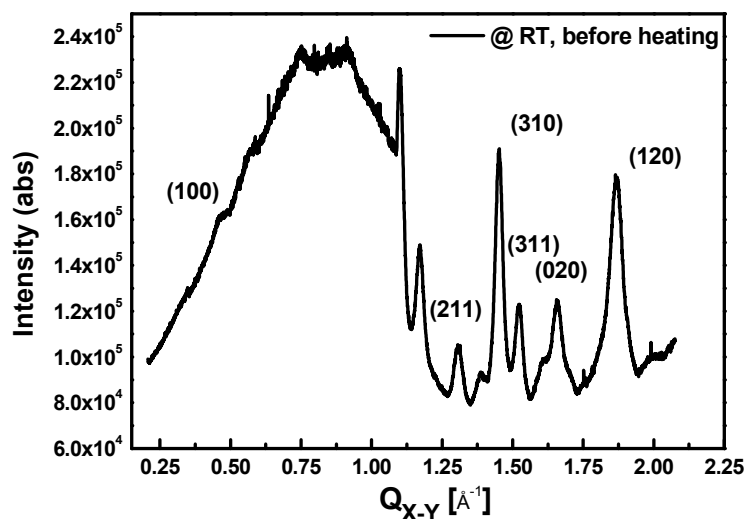


Figure 6.13 In-plane measurement for HMW P3HT thin film on top of HMDS coated SiO_2/Si substrate for as spun sample at $\alpha_i = 0.15^\circ$.

6.7. Discussion

We have seen the AFM, TEM, DSC, GID as well as GOD measurements at room temperature, combining all one can conclude HMW fraction properties as given below.

The higher molecular fraction has shown the broad (100)-reflection peak compared to LMW fraction, which is corresponding to the chain-chain interlayer distance appeared at $Q_z = 0.383 \text{ \AA}^{-1}$, as well as the reflection peak at $Q_{x-y} = 1.626 \text{ \AA}^{-1}$ caused by the stacking of the chains within the main chain layers. This latter peak is normally denominated as (020) reflection. Interestingly, even though peak width of HMW fraction is larger than LMW fraction, our measurements indicate 4-5 time bigger crystallites present in LMW fraction than HMW P3HT. At the same time the integrated intensities were higher in HMW fraction than LMW; this could be due to longer molecular length and multiple connections with next neighboring molecules.

Therefore, we can assume that in HMW fraction, the number of chains organized in well ordered domains increases largely with increasing molecular weight, however, the size and perfection of the crystallites decreases. The corresponding lattice constant normal to the substrate ('a') changes as well with the molecular weight i.e. alkyl chain stacking could be the

function of molecular weight [6-9]. Considering this we have already proposed the monoclinic unit cell for LMW and it would be well applicable to HMW fraction within slight changes in 'a' and 'b' values then the chain-chain interlayer distance is found to increasing from 15.8 Å for the ethyl acetate fraction to 17.3 Å for the chloroform fraction, while the chain-chain intra-layer stacking distance slightly decreases from 3.9 Å to 3.8 Å with increase in molecular weight. Parallel to it, the presence of (310) peak indicates the spaghetti like 3D ordering of molecules.

As we know HMW fraction has shown the high charge carrier mobility compared to its LMW counterpart, therefore it would be great if we can improve the structure properties of this fraction, especially by the recrystallization one can reduce the amorphous contribution and therefore crystallites part will increase. Thus, improving the crystalline to amorphous ratio can also induce the high mobility. Second contribution comes from surface- interface region, if by playing with different dielectric layer we can improve the molecular packing at interface level therefore one could also improve the mobility since the charge carriers can only flow from first 5-10 layers from the interface. [14] Therefore our next chapter based on temperature induced recrystallization of HMW fraction as well as phase transition and systematic study of dielectric layers contribution after a stepwise long time heating.

6.8. References

- [1]. D. H. Kim, Y. Jang, Y. D. Park, K. Cho, *Macromolecules*, 39, 5843, 2006.
- [2]. Trznadel, M.; Pron, A.; Zagorska, M.; Chrzaszcz, R.; Pielichowski, J.; *Macromolecules*, 31, 5051-5058, 1998.
- [3]. Kline, R. J.; McGehee, M. D.; Kdnikova, E. N.; Liu, J.; Frechet, J. M. J. *Adv. Mater.*, 15, 1519, 2003.
- [4]. S. M. Sze, *Physics of Semiconductor Devices*, Wiley, New York, 1981.
- [5]. Sawyer, L. C.; Grubb, D. T. *Polymer Microscopy*; Cambridge University Press: Cambridge, Great Britain, 1994.
- [6]. Scherrer, P. *Nachr. Göttinger Gesell.*, 98, 1918.
- [7]. Prosa, T. J.; Moulton, J.; Heeger, A. J.; Winokur, M. J. *Macromolecules*, 32, 4000-4009, 1999.
- [8]. Zen, A.; Saphiannikova, M.; Neher, D.; Grenzer, J.; Grigorian, S.; Pietsch, U.; Asawapirom, U.; Janietz, S.; Scherf, U.; Lieberwirth, I., Wegner, G.; *Macromolecules*, 39, 2162-2171, 2006.
- [9]. Hugger, S., Thomann, R., Heinzl, T., Thrun-Albrecht, T., *Colloid Polym Sci* , 282, 932, 2004.
- [10] Malik, S.; Nandi, A. K. *J. Polym. Sci. Part B: Polym. Phys.* 40, 2073, 2002.
- [11]. U. Pietsch , V. Holy, T. Baumbach, *High-resolution X-ray diffraction from thin films and lateral nanostructures*, Springer, Berlin, 2005.
- [12]. Joshi, S.; Grigorian, S.; Pietsch, U.; *Physica Status Solidi (a)*, 205, 488-496, 2008.
- [13]. R. J. Kline, M. D. McGehee, M. F. Toney, *Nature Mat.* 5, 222, 2006.
- [14]. T. J. Prosa, , M. J. Winokur, J. Moulton, P. Smith, A. J. Heeger, *Macromolecules*, 25, 4364, 1992.
- [15]. A. Zen, J. Pflaum, S. Hirschmann, W. Zhuang, F. Jaiser, U. Asawapirom, J. P. Rabe, U. Scherf, D. Neher, *Adv. Funct. Mater.*, 14, 757, 2004.
- [16]. C. Tanase, E. J. Meijer, P. W. M. Blom, D. M. de Leeuw., *Org. Electron.* 4, 33, 2003.
- [17]. Zen., A.; PhD thesis, Potsdam, Germany, 2006.

Chapter 7

Temperature Dependent Structural and Crystallinity Studies of HMW Poly(3-hexylthiophene) by X-ray Diffraction Methods

We have reported about the temperature dependent crystalline structure of spin coated thin films of high molecular weight regioregular poly(3-hexylthiophene) (P3HT) ($M_n \sim 30000$ g/mol) and its correlation with charge carrier mobility. These investigations show a reversible change of the crystalline structure, where the interlayer lattice spacing (100) along the film normal continuously increases up to a temperature of about 180 °C, the in-plane π - π -distance becomes smaller compared to the values measured at room temperature. These changes in structure are reversible and can be repeated several times. Further, the temperature-induced structural properties are clearly more pronounced for thicker films, pointing to the role of surface in stabilizing the layer morphology.

Regarding the electrical properties we find a rather constant mobility up to a temperature of ca. 100-120 °C, followed by a continuous decrease. For thick layers this drop is significant and the transistor behaviour almost vanishes at high temperature. Upon cooling back to room temperature, the electrical properties almost recover completely. The drop of the charge carrier mobility at higher temperatures is in contrast to expectations from the structural studies when considering only the crystalline fraction of the polycrystalline layer. Our structural and electrical measurements indicate that the strong reduction of the macroscopic mobility must be caused by a pronounced decrease of the inter-grain transport. The thermally induced crystallization along (100) direction and the creation of numerous small crystallites at the film-substrate interface reduces the number of long polymer chains bridging crystalline domains which ultimately limits the macroscopic charge transport.

In this chapter, we report about unusual temperature behaviour in HMW films of P3HT which are again depth selective. For HMW films, the (100) inter-planar distances increase with increasing the temperature up to the typical melting temperature. At the same time the in-plane (020) reflection shows the decrease in lattice parameters. Surprisingly, this shortening in π - π distance does not result in an increasing mobility but in a complete collapse of field-effect mobility close to annealing temperature. Fortunately both properties, the change in structure and mobility are completely reversible and it can be repeated several times. We

will show this behaviour is the results of larger crystalline size at high temperature grown at the cost of the chain units in their vicinity interconnecting neighbouring crystallites.

Our studies are focussed on X-ray investigations of the structure ordering, the surface-interface dependent structural modifications and thermal behaviour of HMW P3HT films, especially the analysis of the structural properties made parallel and perpendicular to the film to substrate interface. We studied the polymer film structure as a function of film thickness with different dielectric treatments of the SiO₂ insulator. Finally, the structural parameters are related to electrical properties of thin film OFETs.

7.1. Sample Preparation

As stated in chapter 6, all the thin-film samples (HMW fractions) were prepared by spin coating technique, producing different thicknesses by varying the concentration of the solution, keeping the speed of spin-coater fixed at 4000 rpm for 30s.

7.2. X-ray Grazing Incidence Diffraction Studies

The X-ray diffraction measurements [3, 4] were carried out using different synchrotron radiation sources, all the details mentioned in section 6.6. All X-ray measurements were performed under vacuum conditions as stated in chapter 6. This was crucial in order to avoid substantial radiation damage at the polymer sample, also to reduce background and air scattering. Temperature resolved measurements were carried out as stated under section 5.1 (chapter 5). In few cases the second and third heating cooling cycle was performed.

7.3. Structure Investigation as a Function of Temperature

As RT based X-ray diffraction studies (GID and GOD) are already illustrated in chapter 6, therefore in the present chapter we will directly focus on the temperature dependent structural and mobility variation. All the samples parameters analyzed at room temperature are summarized in chapter 6, table 6.2.

The effect of annealing to P3HT thin films in OFET devices was reported for the first time by Abdou et al. [5], they found significant improvement in the OFET characteristics after annealing P3HT thin films at 180 °C under N₂-atmosphere. Zen et al. [6] annealed the P3HT thin films at 150 °C for 5 min and correspondingly found the increase of mobility by factor of two compared to as spun sample. Similar gain was reported by Grecu et al., for pure SiO₂ and

OTS coated SiO₂/Si substrates [7] explained by the improved film morphology due to reduction of trapped solvent within the volume. Bao et al., found that treating a film with ammonia or heating to 100 °C under N₂ can increase the on/off ratio without decreasing the mobility [8]. Only few papers were dealing with structure – property relation of P3HT films at temperatures higher than room temperature.

Werzer et al. [9], have done temperature dependent X-ray diffraction and reflectivity measurements for rr- P3HT of molecular weight (M_w) = 45,000 g/mol at various temperatures. They have observed increase of the (100) lattice spacing associated with an increase of total film thickness of 15%. The FWHM of the peak was decreasing and the intensity was increasing up to 150 °C, followed by decrease of intensity, and also a complete disappearance at 200 °C. Kim et al. [10] reported on a complete reorientation of molecules edge-on into flat-on orientation after annealing of HMW fraction films of having molecular weight M_n = 30,000, M_w/M_n = 1.8 at 240 °C of OTS coated SiO₂/Si substrate.

7.3.1. Grazing Incidence Out-of-Plane Diffraction

A. Annealing Effect

The typical line scan along h-direction (Q_{out}) for type B samples (thick) on HMDS coated SiO₂/Si substrate, before and after annealing is shown in Fig.7.1. It clearly shows that the (100) peak after the annealing step becomes narrower and higher in intensity compared to the as spun sample. The higher order reflections at higher Q values are less affected. This indicates that the improvement in out-of plane crystallinity and size of crystallites induced by the heating cycle. Fig. 7.2 focussed on the temperature dependence variation of (100) planes for the first heating cycle. Starting from room temperature (RT), the intensity increases continuously up to the temperature of about 220 °C followed by decrease of intensity up to melting temperature. We have observed the gain in intensity at high temperature by the factor between 2 and 10 for various samples.

This gain in intensity is accompanied by a decrease in peak position, i.e. increase in (100) spacing. It tells the expansion of unit cell along surface normal direction under the temperature influence. Cooling the sample back to RT the intensity goes back to a value slightly higher than found for the as prepared sample but much smaller than seen at high temperature (HT).

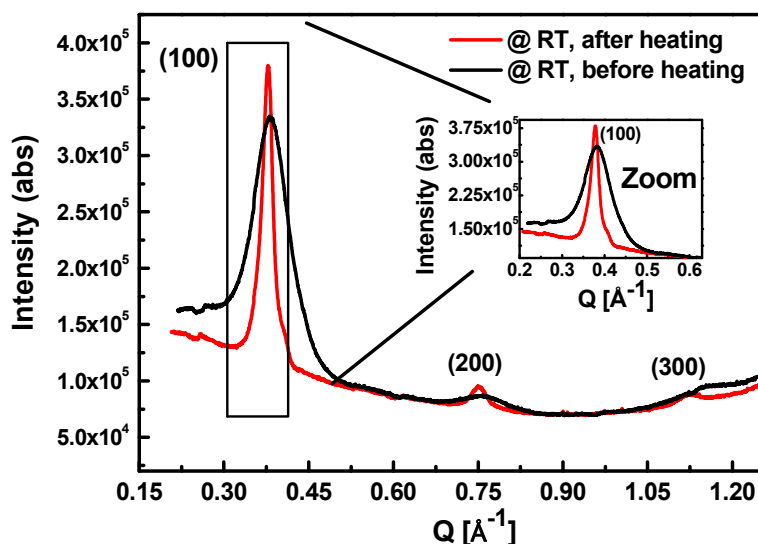


Fig. 7.1 Out of plane scan for 40 mg/ml P3HT on HMDS coated SiO_2/Si substrate for $\alpha_i = 0.15^\circ$.

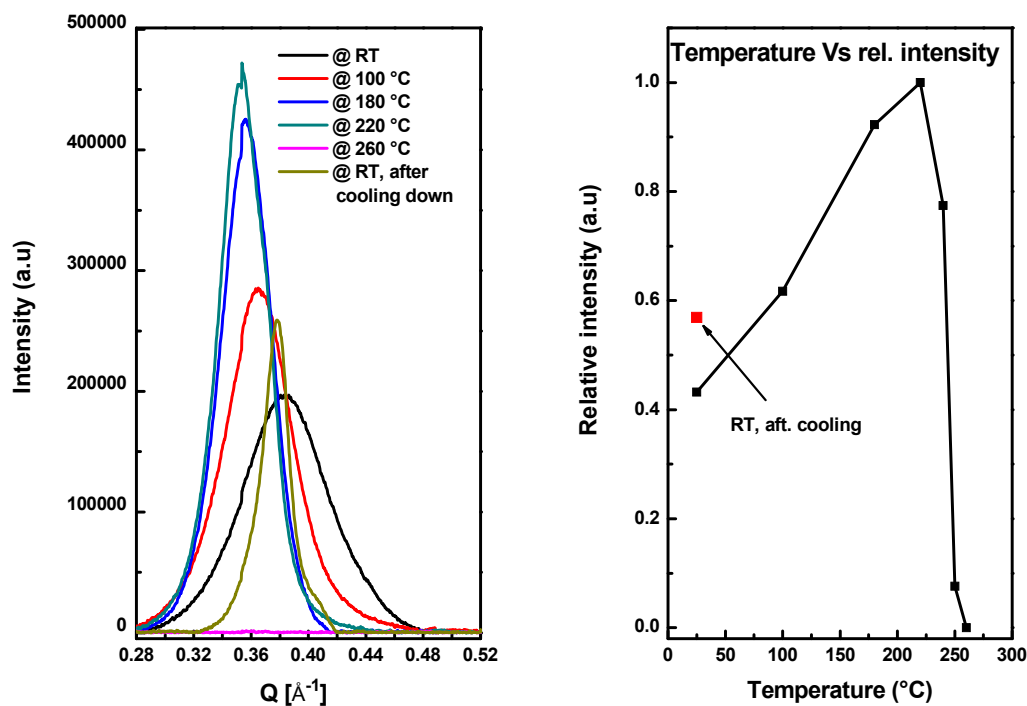


Figure 7.2 Temperature dependent variation of (100) peak for type B sample on HMDS modified substrate for $\alpha_i = 0.15^\circ$.

The increase of intensity after cooling indicates the improvement of the structure ordering. At same time the lattice spacing comes nearly back to the RT value. The similar, temperature scans have been repeated for thin samples (Type A). As shown in Fig.7.3, the (100) out-of plane peak appears only after first annealing. The rest peaks are almost uninfluenced by

the heat treatment. Comparing with sample B, sample A shows higher contribution of amorphous part centred at $Q = 1.5 \text{ \AA}^{-1}$ with dominating (310) peak.

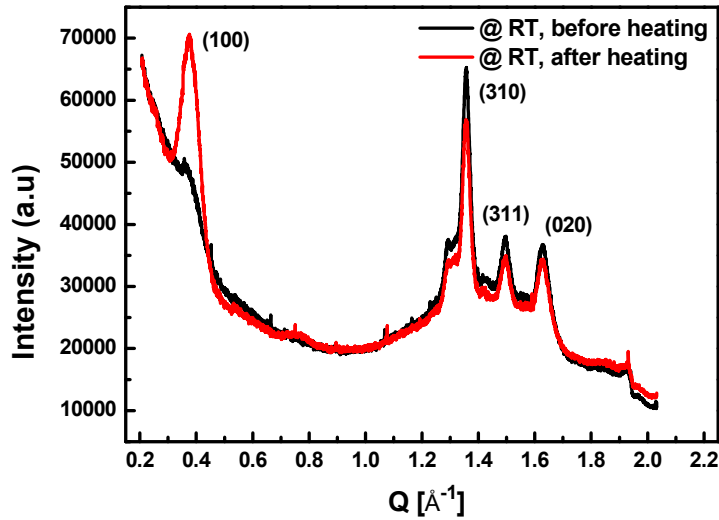


Figure 7.3 Out-of plane scan of a thin film of HMW P3HT film on HMDS coated SiO_2/Si substrate before and after first annealing step.

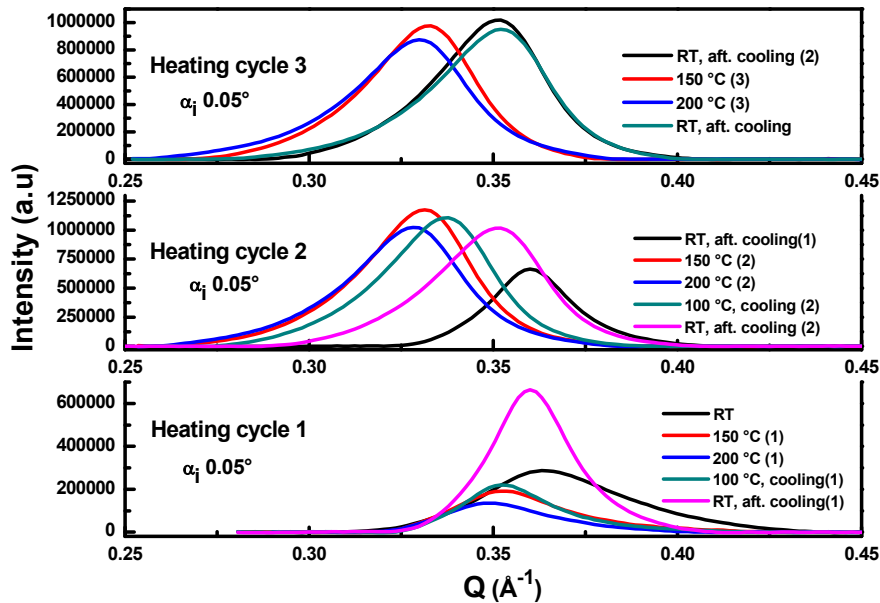


Figure 7.4a Temperature dependent cycles and (100) peak expansion along the normal direction for thick HMW P3HT on HMDS coated SiO_2/Si substrate for $\alpha_i = 0.05^\circ$.

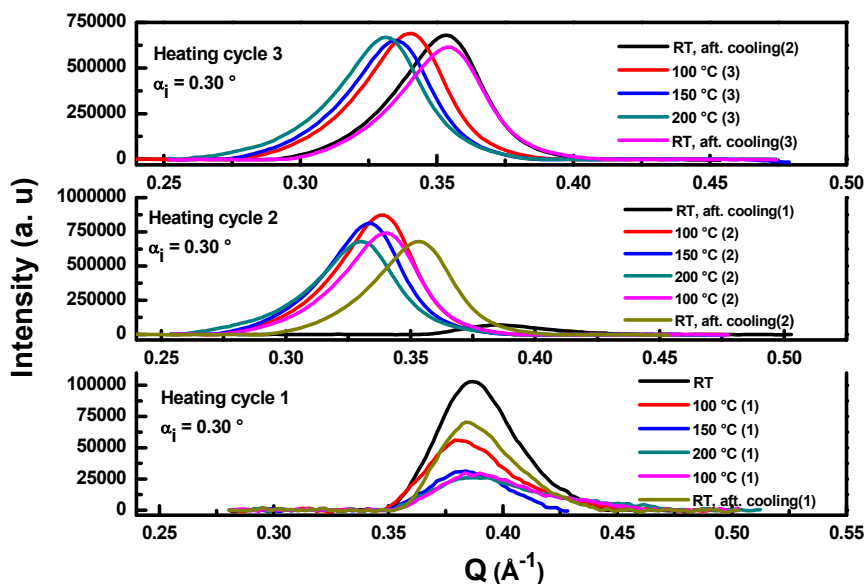


Figure 7.4b Temperature dependent cycles and (100) peak expansion along the normal direction for thick HMW P3HT on HMDS coated SiO_2/Si substrate for $\alpha_i = 0.30^\circ$.

B. Number of Heating Cycles Vs Structure Equilibrium

Fig.7.4 (a, b) shows the optimization of thermodynamical equilibrium state of the film morphology behaviour for two different angle of incidences, $\alpha_i = 0.05^\circ, 0.30^\circ$. One can clearly see that the as prepared samples are not thermodynamically optimised, and this behaviour is reversible for several heat cycles. The peak positions switches in between the values of HT and RT back and forth. After second cycle the peak intensities does not change anymore characterising the appearance of two equilibrium states. Where the phase appears at the elevated temperature can be corresponds to mesomorphic state of the material at elevated temperature [11-12].

C. Temperature Induced Physical Properties Variation

The increase of d-spacing and crystallite size in vertical direction as a function of temperature is shown in Fig. 7.5 for type B sample. The crystallite size was calculated from the FWHM of Bragg peak using Scherrer's equation [13]. We found the d-value increases nearly linear up to melting temperature. The thermal expansion coefficient of $\alpha_T = \Delta d / (d\Delta T) = 4.7 \times 10^{-4}$ is nearly independent from type of interface treatment. At the same time the crystalline size increasing from about 10 nm at RT by factor of 2-3 at HT, again independent from dielectric layers treatment. On the other hand after cooling back to RT the gain in integrated

intensity of (100) peak is highest for HMDS and lowest for OTS coated SiO₂/Si substrate as shown in (Fig. 7.6).

The similar temperature dependence of d-spacing and crystallite size for sample type A is shown in Fig.7.7. The d- spacing increasing with increasing temperature but it is not as high as compare to samples B. Here the type of surface treatment results in rather different d-values at RT which converge to almost the same value at HT. Similarly, compared to sample B, the increase in crystallite size also not as high as in sample B.

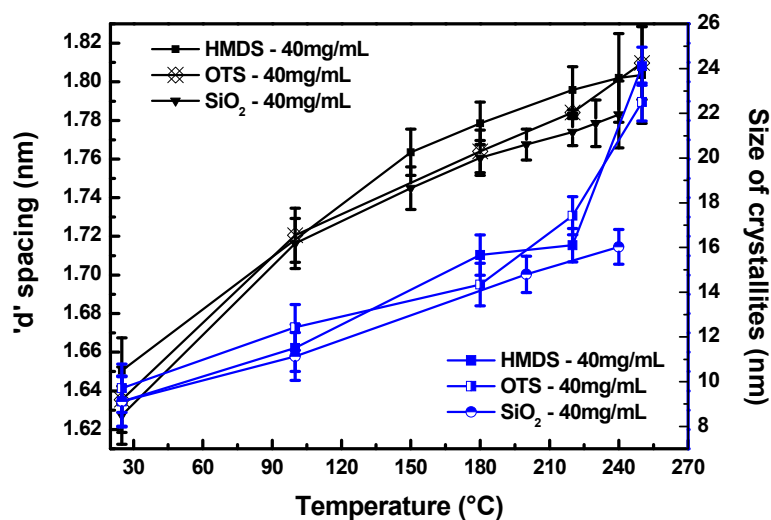


Figure 7.5 Temperature dependent inter-planar distances and crystallite size variation of thick films (type B) on three different substrates (HMDS, OTS, SiO₂).

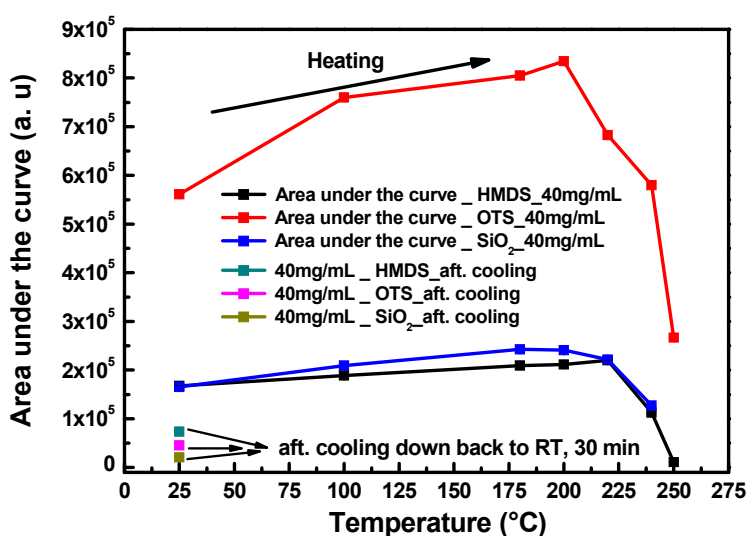


Figure 7.6 Volume (area under the curve) Vs temperature for three different substrates based on their corresponding OOP scans.

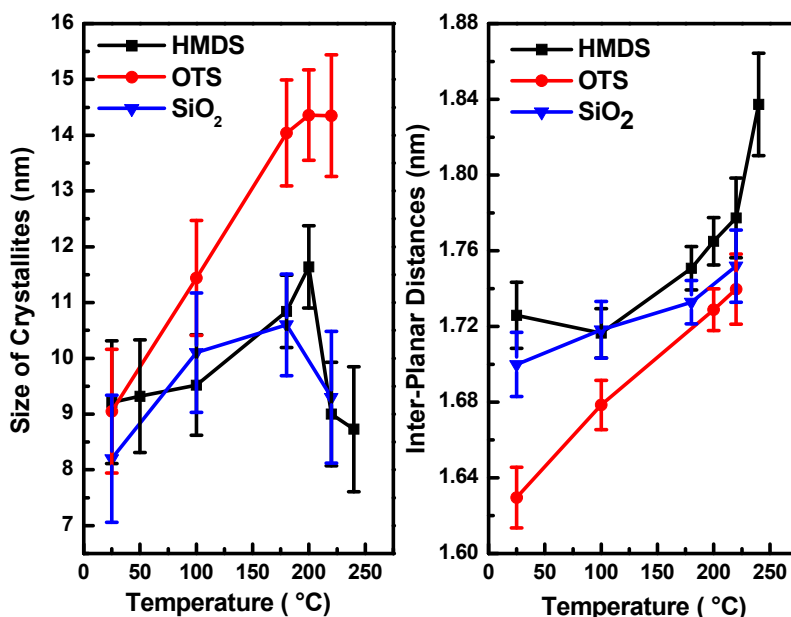


Figure 7.7 Temperature dependent out-of plane inter-planar distances and size of crystallites variation for thin films of HMW P3HT on three different dielectric layers coated on SiO₂/Si substrates.

7.3.2. Grazing Incidence Diffraction (GID)

Fig. 7.8 shows in-plane scans of B type samples on HMDS coated SiO₂/Si substrate, before and after annealing. The main improvement of this treatment, increase of Bragg peak intensities, including the appearance of in-plane (100) and (020) peaks.

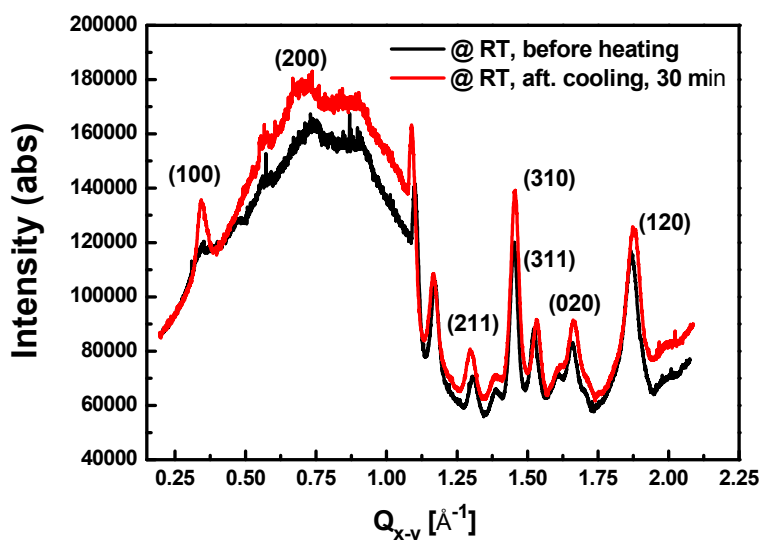


Figure 7.8 In-plane measurement for HMW P3HT thick film on top of HMDS coated SiO₂/Si substrate, after and before first annealing, $\alpha_i = 0.15^\circ$.

The increase in intensity of (100) peak after cooling it back to RT, indicates the increase of alkyl isolating chains along the inplane direction, which will ultimately hinders the charge transport for the bulk films.

Selected from Figure 7.8, the (020) reflection which is a characteristic of π - π distance between neighbored thiophene rings shows a bimodal behaviour as a function of temperature, see Figure 7.9. The peak switches between low intense position centred at 1.66 \AA^{-1} at RT and a higher intense centred at 1.71 \AA^{-1} at HT indicating shrinkage of π - π distance by 3%. The (020) peak width is larger at HT compared to RT indicating rather reduced in-plane crystallite size. After cooling back to RT, the (020) peak moves back to almost the same position as before heating for as spun sample, indicates the process is reversible.

The similar, bimodal behaviour of inplane (020) peak for type B samples also found for type A samples (Fig. 7.10). The (020) peak is shifted to exact same value at HT as found for type B samples and the peak width is enlarged without significant variation in intensity. This shows that the behaviour of (020) peak is mainly due to the film - substrate interaction.

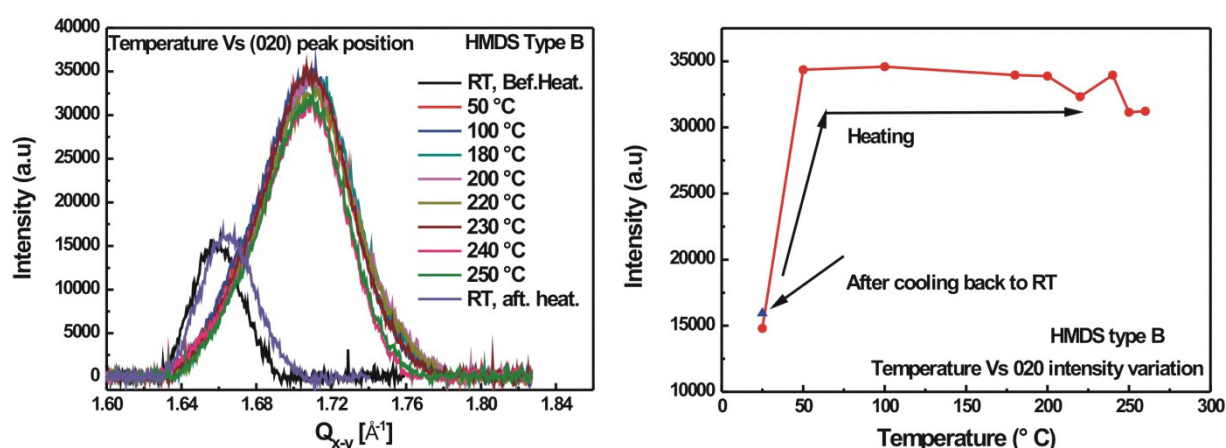


Figure 7.9 Temperature dependent in-plane measurements for (020) peak for thick P3HT film on HMDS modified substrate.

7.4. Depth Dependence Morphological Changes and Ordering

This statement can be proved by exploiting the depth dependence of scattering while tuning the angle of incidence in order to access the particular length scale of film thickness. Here, diffracted intensity compared with the diffraction curves taken at $\alpha_i \geq \alpha_{cf}$ with those measured at $\alpha_i \geq \alpha_{cs}$. Under the first condition, the information stems from the first 10 nm below the surface of the thick film, whereas under the second case the whole film is probed including the buried film- substrate interface. Fig. 7.11 shows the variation of (100) peak in-

tensity as a function of temperature. The bulk surface curve ($\alpha_i = 0.30^\circ$) shows an increase in intensity between RT and 100 °C followed by decrease at higher temperatures.

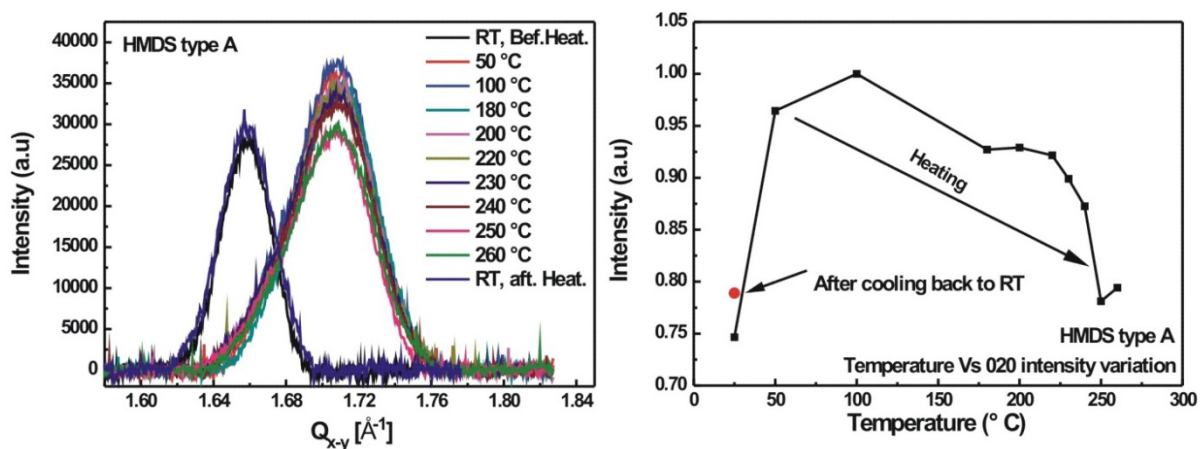


Figure 7.10 Temperature dependent (020) peak variation for thin film of HMW P3HT sample on three different substrate, for $\alpha_i = 0.15^\circ$.

The other curves ($\alpha_i < 0.30^\circ$) show the continuous decrease in intensity with increasing temperature as found for thin films. The continuous decrease in intensity with increasing temperature for smaller α_i^s compared to the bulk film shows that the temperature induced morphological disordering could start from the air-film interface, whereas the interface gets more ordered up to particular temperature ($\sim 100^\circ\text{C}$) and followed by decrease of intensity shows the appearance of disordering at the interface level.

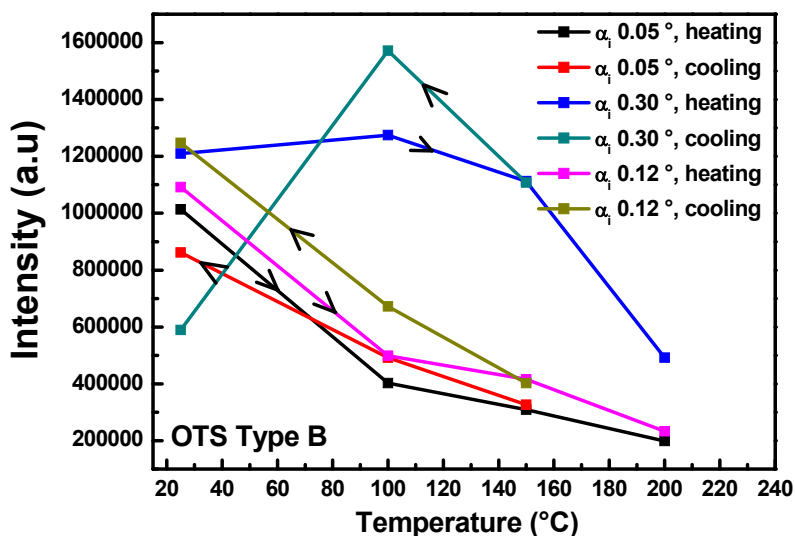


Figure 7.11 Temperature dependent out-of plane 100 peak intensity variation for different angle of incidence α_i^s for a thick film on OTS coated SiO_2/Si substrate.

While after cooling, for the curves, except of $\alpha_i = 0.12^\circ$, there is a drop in intensity, while for $\alpha_i = 12^\circ$ it increases. Due to half decrease in intensity for $\alpha_i = 0.30^\circ$ for OTS substrate after cooling, it appears that there is reorganization of molecular packing after heating at the interface level, which induced more disordering for OTS coated SiO_2/Si substrate and ultimately gives hint that OTS coated SiO_2/Si substrate could be good substrate for as spun samples. This point can also be confirmed from next coming point 7.5 (Fig. 7.13).

7.5. Depth Dependence Lamella Ordering for Thick and Thin Films

As we know, P3HT molecules on solid substrate can organise themselves, mainly in two ways as shown in Fig. 6.12, the edge-on orientation and flat-on orientation, among these two orientations, edge-on orientation is more favourable as it provide 2D charge transport having the isolating alkyl chains along the normal to substrate direction, while for flat-on orientation these isolating chains fall along in-plane direction and isolate the 2D charge flow. At the same time we have seen already from previous chapters that spin coated films of P3HT on solid substrate has shown the mixed type of orientation, where still edge-on orientation dominates on flat-on orientation. Now Fig. 7.12 shows the depth dependence of FWHM variation for the (100) peak along parallel to surface direction for thick and thin films (all the line scans are cut it along parallel to the substrate direction from the CCD images). We have exploited the depth resolution of X-ray beam tailored by choosing α_i larger or smaller α_{cf} . $\alpha_i = 0.05^\circ$ corresponds to the measurements ~ 10 nm below the surface whereas the total film was measured for $\alpha_i = 0.30^\circ$.

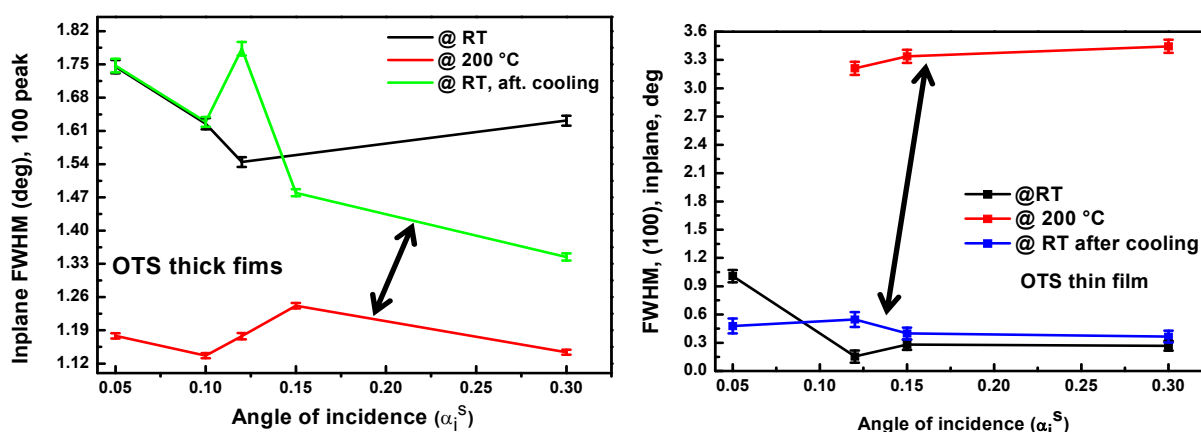


Figure 7.12 Depth dependence variation in FWHM for (100) peak along parallel to surface direction for type B and type A samples on OTS coated SiO_2/Si substrate.

Now if we comparing the thick and thin films one can notice the major differences as for the thick films the in-plane FWHM of (100) peak is smaller at high temperature within the whole film. The RT values (before and after heating) are same at the surface and decrease towards the bulk. For large penetration depth the FWHM is sharp decreased after annealing the samples.

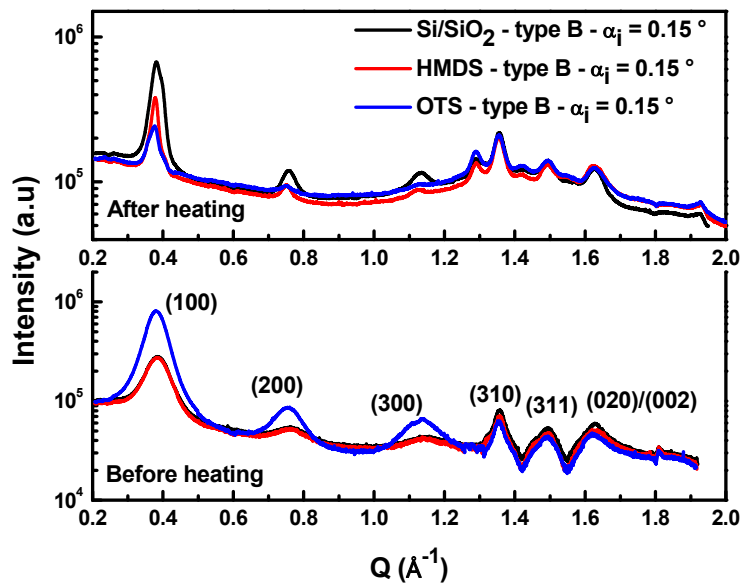


Figure 7.13 Out-of plane scans for three different dielectric layers coated on SiO₂/Si substrates for before heating (bottom) and after heating (upper) for $\alpha_i = 0.15$.

This behaviour is opposite for thin films. Here we are no more depth selective and find the FWHM factor 4 larger at HT compared to RT values before and after annealing. It gives the direct indication that higher surface-interface induced ordering has found for thick films while there is no significant change at the interface level found for thin films. The Fig. 7.13 summarizes the effect of annealing for samples B grown on three different dielectric layers (HMDS, OTS, bare SiO₂) coated SiO₂/Si substrate. Comparing the scan at bottom (before heating) with scan at top (after heating), one can conclude that samples on top of HMDS or SiO₂ coated substrate show best performance after annealing whereas OTS coated SiO₂/Si substrate is good for as prepared sample.

7.6. Mobility Measurements

OFET mobilities of Type B and A films were measured in-situ as a function of temperature (Figs. 7.14 and 7.15). In thick films the mobility remains rather constant within a

temperature range from room temperature of about 100 °C (Fig. 14) followed by a sharp drop above 100 °C, independent from the kind of surface treatments. In case of the non-treated and the HMDS coated SiO₂/Si substrates, the OFET devices even lose their transistor behaviour around this temperature, while in case of OTS-treated interface, the device remains operable until 186 °C. Apart from this particular result, HMDS and OTS treatments yield the same results in terms of the absolute value and the temperature dependence of field-effect mobility for thick and also for thin films (Figs. 7.14 and 7.15). Note, that in thick films the final mobilities of the silanized samples recover almost to the value of the initial mobility, while the mobility in non-silanized OFETs develops into a significantly lower value after the measurement procedure.

Surprisingly, the thin OFET devices appear to be significantly more temperature stable as compared to their thick counterparts (Fig. 7.15). The field-effect mobility remains roughly constant until 150 °C in the case of silanized samples. At higher temperatures mobility drops by ca. 1 order of magnitude, but the silanized devices are still operable even at the maximum temperature of 186 °C. For the devices with a non-treated SiO₂ interface, the mobility decreases continuously starting from room temperature. Above 150 °C no reasonable transistor behaviour can be observed. After cooling back to RT, the mobilities are ca. half of the initial mobility for both silanized and non-silanized devices.

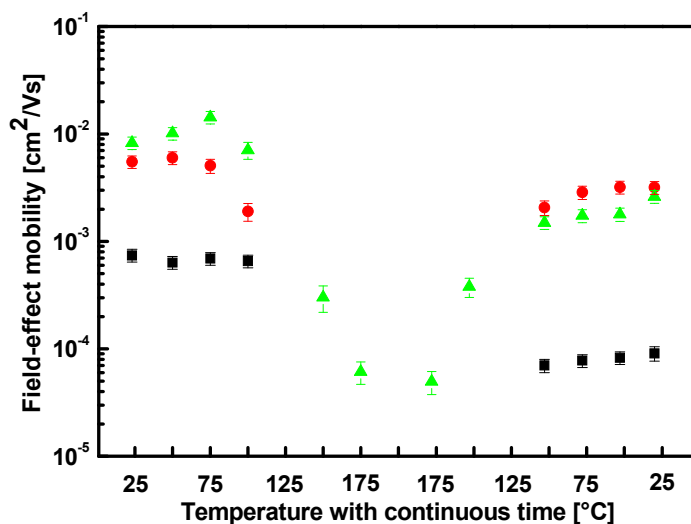


Figure 7.14 Temperature-dependent hole mobility in thick P3HT field-effect devices (type B), measured in-situ in a cyclic procedure of heating from room temperature to 150°C (186°C for OTS treatment), followed by cooling back. Different treatment of the insulator-semiconductor interface using untreated SiO₂ (black symbols), silanized SiO₂ by 26 h in a HMDS atmosphere (red symbols), and silanized SiO₂ by 10 min immersing into OTS (green symbols).

The slight reduction of the field-effect mobility after passing the temperature protocol as compared with its initial values is not necessarily only due to morphological changes within the P3HT layer. Because of the top-contact geometry of the OFET devices, it is possible that the gold atoms, of which source and drain consist, diffuse into the polymer layer at elevated temperatures. This could be due to the enhanced diffusive motion of the gold atoms, of which source and drain consist, diffuse into the polymer layer at elevated temperatures, possibly assisted by the electric field during the measurements, with the result of a poorer electrical contact of source and drain electrodes with the organic layer as well as morphological changes in the polymer layer in the proximity of the contact.

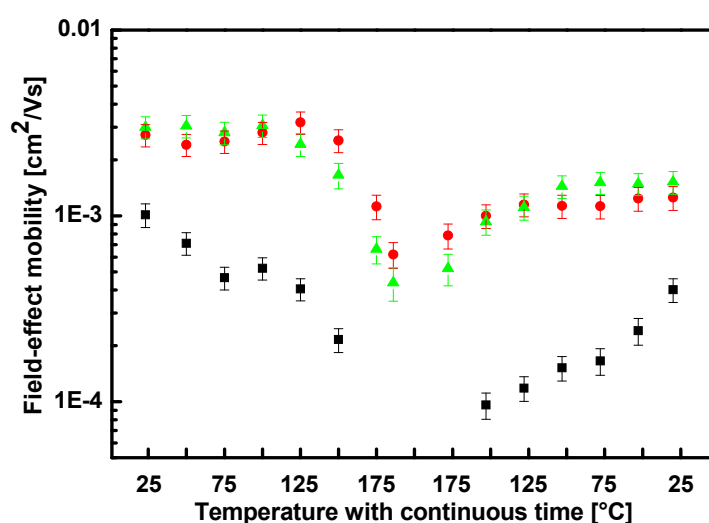


Figure 7.15 Temperature-dependent hole mobility in thin P3HT field-effect devices (1mg/ml), measured in-situ in a cyclic procedure of heating from room temperature to 186°C (175°C for bare SiO₂), followed by cooling back. Different dielectric treatment of the insulator-semiconductor interface using bare SiO₂ (black symbols), silanized SiO₂ by 26 h in a HMDS atmosphere (red symbols), and silanized SiO₂ by 10 min immersing into OTS (green symbols).

On the other hand, the drop in mobility at elevated temperatures must indeed be related to thermally induced and reversible morphological changes, the mobility recovers almost completely upon cooling back to room temperature.

7.7. Discussion

For the first time we have performed systematic structure and mobility investigations as a function of temperature. We have found the clear correlation between structure and mobility changes as function of temperature. From literature it is well known that electrical properties become improved after the annealing step [4, 5, 7-9]. This is understandable because

the annealing helps to transform the non-equilibrium state after the spin coating process into an equilibrium state of the film morphology. While annealing, the remaining solvent can evaporate and the thermal energy of chains allows for better packing. From structural point of view these effects are verified by sharper rocking curves and higher Bragg peak intensities compared to as-spun sample as shown in Fig.7.2. Not so much is known so far about structure changes at higher temperatures. Our experiments give evidence that the structural ordering can be much better at the temperature higher than RT. For technologically relevant films of HMW P3HT with thickness larger than 100 nm both structural parameters are best at the temperature close to ~ 200 °C which is about 40 °C below T_m . Moreover, we can characterize this HT structure as a thermotropic phase appearing in addition to the phase found at RT. Once one has transformed the system into equilibrium by a first heating cycle one can switch between both phases for several times.

However, for OOP scans at the HT phase the FWHM is smaller but peak intensity is higher compared to RT phase. Comparing both quantities in terms of integrated intensities (area under the curve) the increase between RT and HT is not too much (Fig.7.6); the number of crystallites contribution to the peak is roughly same. Considering the change of in-plane Bragg peak as (020) in addition one can find the crystallite size in-plane becomes smaller at HT compared to RT but the numbers of crystallites are increased. Both cases can be explained by a model where crystals existing at RT grown in height at the cost of their lateral width and by collecting chains out of the close vicinity to the crystals accompanied by nucleation of new small crystallites at the film-substrate interface. This scenario is supported by our results obtained for thin films. Here the vertical size of crystallites can grow up to a size not larger than the total film thickness. However, the in-plane behaviour is same as for thick films; the number of in-plane crystals at HT is larger than at RT. The later one is a hint for strong influence of the interface on structural order as suggested by our measurements for LMW P3HT material [14]. A second finding concerns the changes in lattice parameters. For thick films we have found an expansion of out-of plane spacing at HT accompanied by compression of in-plane lattice parameter. These changes can be associated with a stretching of alkyl chains but a smaller π - π distance of thiophene rings. Same changes in π - π distance are observed for thin films. While the out-of plane d-spacing does not expand much compared to thick films and the decrease of size of crystallites might be explained by the assumption that this spacing can only expand for crystals not pinned at the film-substrate interface. The later can happen in thick films only, which is supported by Fig. 7.11. Our measurements (Fig. 7.12), suggests that due to less material, the free volume present in thin films should be lesser than thick films.

Thin films are better ordered compared to thick films (powder rings). We have not observed any temperature induced improvement of (100) plane tilting i.e. in thin films along OOP direction (100) planes are not exclusively parallel to the substrate, which is one of the requirements of high mobility.

It also indicates that for thin films there is no interface region and films are behaving as a whole – while oppositely, thick films have shown the sharp improvement of (100) planes after annealing. Now, (100) planes are much better parallel compared to as spun sample, this effect is more pronounced at the interface region - this might be one of the reason for high mobility in thick films due to presence of interface region –where the big crystallites have grown after annealing and (100) planes become parallel to substrate providing 2d network for charge transport. This is absent in ultrathin films.

Finally, we like to discuss the temperature dependence of the mobility in relation to the changes to relevant structural parameters. This correlation might also help to understand which process ultimately limits the charge transport in P3HT based transistors. Generally, we find a drop in charge carrier mobility for temperatures above ca. 120° C. Depending on the kind of silanization, the OFET behaviour can even disappear completely at elevated temperatures. At first glance, this seems to be contradictory to the expectations from the structural studies. Here, the in-plane measurements clearly show the decrease in π - π stacking distance, which shall assist the charge transport within the crystalline regions. Also, the growing number of crystallites in the in-plane direction, i.e. in the direction of charge transport in an OFET, should improve the mobility in the transistor. For clarification of this apparent conflict, we like to point out, that the solid layer formed from long crystallisable polymer chains exhibits– in equilibrium and non-equilibrium – always a multiphase morphology with crystalline domains separated by amorphous regions. Especially in high molecular weight compounds, the domain boundaries are hard to distinguish. There is abundant evidence that the crystalline regions in P3HT layers constitute only a fraction of the whole samples volume [4, 6, 15].

Formerly, we found by DSC analysis that films of HMW fraction of P3HT, comparable to the presently investigated substance, have a crystallinity of only 18 vol. % [8]. Despite this, the room temperature mobility in layers of P3HT with high molecular weight and regio-regularity is quite considerable. It has, therefore, been proposed that long polymer chains bridge the amorphous regions, allowing the charges to move efficiently between the crystalline domains. Our structural and electrical measurements indicate that the strong reduction of the macroscopic mobility comprising the charge transport over numerous of domains above a

certain temperature cannot be explained by thermally induced morphological changes within the well-ordered crystalline domains but that this effect must be due to the pronounced decrease in the inter-grain transport. Our studies provide strong evidence that the crystallite size along the (020) direction becomes smaller, due to shrinkage of π - π stacking. With the whole channel area being constant, this process will diminish the amount of crystalline material accessible for the carriers during in-plane transport in the OFET. In accordance with this interpretation the effect of temperature on the OFET mobility is far more pronounced in thick layers. Here, the size of the crystallites was shown to increase substantially in the vertical (100)-direction, probably at expense of their lateral width.

This confirms that the macroscopic charge transport, as it is present in OFETs, is crucially determined by the presence and especially by the extent of amorphous domains within the path of the carriers. It is, therefore, not surprising that the temperature dependence of charge carrier mobility, it is only indiscernible related to thermally induced changes in the structure of crystallites. The coincidental improvements in crystalline quality and the general increase of ordering within a polymer film is the key to have a high mobility and good device performance.

Compared with LMW P3HT the mobility in HMW P3HT is high because the main chain is of the order of average distance between crystallites. This interconnection becomes disturbed increasing the temperature, ones due to the increased chain mobility and second due to the collection of chains by the growing crystals. Assuming the crystals in a polymer are growing by chain folding it becomes understandable that the regions close to the crystals becomes cleared by stretched chains arranged parallel to the film-substrate interface. Ones this “collection” effect is larger for thick films it becomes understandable why thin films show the smaller drop in HT mobility compared to the thicker one.

7.8. References

- [1]. D. H. Kim, Y. Jang, Y. D. Park, K. Cho, *Macromolecules*, 39, 5843, 2006.
- [2]. Kline, R. J.; McGehee, M. D.; Toney, M. F.; *Nature Mat.*, 5, 222-228, 2006.
- [3]. U. Pietsch, V. Holy, and T. Baumbach, *High Resolution X-ray Scattering from Thin Films and Multilayers*, Springer Tracts in Modern Physics, Vol. 149, Springer-Verlag, Berlin, 1999.
- [4]. Joshi, S.; Grigorian, S.; Pietsch, U.; *Physica status solidi (a)*, 205, 488-496, 2008.
- [5]. M.S.A Abdou, X. Lu, Z. W. Xie, F. Orfino, M. J. Deen, S. Holdcroft. *Chem. Mater.* 7, 631, 1995.
- [6]. Zen, A.; Pflaum, J.; Hirschmann, S.; Zhuang, W.; Jaiser, F.; Asawapirom, U.; Rabe, J. P.; Scherf, U.; Neher, D.; *Adv. Funct. Mater.*, 14, 757-764, 2004.
- [7]. S. Grecu, M. Roggenbuck, A. Opitz, W. Brütting, *Org. Electron.* 7, 276-286, 2006.
- [8]. Bao, Z.; Dodabalapur, A.; Lovinger, A. J.; *Appl. Phys. Lett.*, 69, 4108-4110, 1996.
- [9]. Werzer, O., Matoy, K., Strohhriegl, P., Resel, R. *Thin Solid Films*, 515, 5601-5605, 2007.
- [10]. D. H. Kim, Y. Jang, Y. D. Park, K. Cho, *Macromolecules*, 39, 5843, 2006.
- [11]. Gennes, P. G.; Prost, J.; *The physics of liquid crystals*, 2nd ed.; Birman, S.; Edwards, S. F.; Llewellyn, C. H.; Rees, S. M.; Oxford University press: New York, 1993; Vol. 10, p 507.
- [12]. P. G. de Gennes. *Scaling Concepts in Polymer Physics*. Cornell University Press, Ithaca and London, 1979.
- [13]. Yang, C.; Orfino, F. P.; Holdcroft, S. *Macromolecules*, 29, 6510–6517, 1996.
- [14]. Joshi, S.; Grigorian, S.; Pietsch, U.; Pingel, P.; Zen, A.; Neher, D.; Scherf, U.; *Macromolecules*, 41, 6800-6808, 2008.
- [15]. Dean M. DeLongchamp, R. Joseph Kline, Y. J., E. K. Lin, D. A. Fischer, D. J. Gundlach, S. K. Cotts, A. J. Moad, L. J. Richter, M. F. Toney, M. Heeney, I. McCulloch, *Macromolecules*, 41, 5709-5715, 2008.

Summary and Outlook

Organic electronic materials and devices constitute of novel and exciting field and it can show a great potential for commercial applications in the near future. Understanding the physics of the formation of complex structures and ultimately its correlation with charge-carrier mobility in such polymer based devices is just as rewarding as developing new materials and device designs.

Important aspects in this performance are the thin films of conjugated (semiconducting) organic molecules can be applied in organic electronic devices, such as organic light-emitting diodes, organic field-effect transistors and solar cells. To optimise the performance of such organic electronic devices, fundamental knowledge about the metal-organic interfaces and control of the structure (morphology, molecular orientation) of the organic films is necessary. In this thesis a study has presented about the interaction at the interfaces between conjugated organic molecules and different dielectric layers, and the impact of such an interface on the structure of the organic film. In fact, this understanding is essential for the progress of the field and also the application in devices. We have investigated a series of problems related to charge transport and morphology correlation in OFET devices. This is relatively new area and more work needs to be done in the way of understanding the nature of film morphology and surface –interface interaction contribution towards charge transport in these devices.

S.1. Summary

The primary goal of this thesis has been precisely to contribute and enhance our understanding of the nature of complex structure formation and its characterization of such thin semi-crystalline films. Beyond the formation of different morphology as a bulk and also as thin films with increasing molecular weight and surface-interface interaction variation with molecular weight, temperature dependent recrystallization behavior of such semicrystalline thin and thick films. Parallel to it, variation of this surface-interface potential by varying the dielectric layers and its effect on interface morphology and consecutively correlation with charge carrier mobility were our primarily aim. The results of our experiments have given a in-depth structural information of such materials utilizing the present X-ray scattering techniques with the help of AFM, TEM placed us among important contributors to this field and this work will continue along new directions in the future.

Chapter 4 and chapter 5 showed a strong dependence of both the charge carrier mobility and morphology on the LMW fraction. Both chapters outlined model to describe the mobility dependence primarily through surface and interface morphology effects due to the differences in packing resulting from the chain length. LMW films spin coated on various dielectrics (HMDS, OTS) modified substrates formed highly ordered rod like crystals. The rod like crystals are embedded in amorphous matrix and loosely connected with their neighbour crystallites that limit inter-rod charge transport. Considerable changes in both morphology and charge transport were observed for the LMW compared to HMW fraction films. The X-ray analysis reveals that the films are mainly amorphous and containing randomly oriented nanocrystallites with the best match for a monoclinic unit cell. Additionally, polymorphism was found for ~ 200 nm thick films of LMW fraction. Interestingly, the film morphology varies as a function of the film thickness. Under the influence of pinning effect, for LMW material the random orientation of nanocrystallites change to preferential orientation of lamellae along the surface normal when the size of crystallites become of the order of film thickness, i.e. below 20 nm.

The time of recrystallization after annealing is crucial for the size of crystallites improvement along surface normal direction, this could be a decisive factor which can improve the crystalline to amorphous ratio and ultimately the increase of ordered region especially at the interface region should improve the charge carrier mobility. GID measurements also showed an increase in the amount of in-plane π - π stacking can be associated with the increase in mobility. Despite the improvement of in-plane π - π stacking for LMW fraction compared to HMW fraction under our GID and GOD scans, their charge carrier mobility still quiet lower than HMW films. These results strongly supported that presence of crystalline domains are vital but still the disorder parts or amorphous part controls the mobility of such films as it tries to hinders the connection between nearest neighboring crystallites. Therefore by controlling this amorphous region one can control the mobility. The recrystallization phenomenon therefore is the primary way of controlling the disordered region and can convert it any thin film to more crystalline film. Therefore, we have studies this recrystallization phenomenon by step up temperature heating for low as well as for HMW fractions by means of GID and GOD X-ray scattering technique. We have also demonstrated the preferential alignment of nanocrystallites at the film-substrate interface by means of three different X-ray scattering techniques,

1) α_i resolved measurements we have shown that the crystal peak intensities and the scattering from the interface increases with penetration depth of probing X-ray with the sam-

ple independent from whether the film was prepared either on HMDS or OTS coated SiO₂/Si substrates.

2) In addition we have shown that the melting behaviour of the films changes qualitatively by decreasing the film thickness.

3) We found direct pictures of the changing orientation distribution by imaging of 2D scattering. Moreover, using highly intense synchrotron radiation of ESRF we could determine the orientation of the pinned nanocrystals.

Regarding the comparison of electronic and structural properties, we have found that the mobility remains constant over a wide range of thicknesses, despite of significant increase in in-plane ordering when decreasing the layer thickness, as revealed by our X-ray measurements. Based on our structural and electrical properties we presume the existence of an interface-near ultrathin crystalline layer, stabilized by the strong interaction between the polymer chains and the gate insulator, with the main chains oriented almost exclusively parallel to the substrate. This interface region is present in all samples but dominates for samples with thickness below about 25 nm, and it is responsible for charge transport in the OFET measurements. The existence of amorphous regions in between highly-crystalline lamellae (or nanofibrils) in short chain P3HT samples, even in films grown by epitaxial solidification controls the charge carrier mobility of such semicrystalline system.

We have also observed a complete change of crystal unit cell with increasing temperature. Moreover, the phase transition between solid to melt states of polymer changes as a function of thickness. It is found to be continuous drop of intensity for thick films, but sharp drop for thinner films. Where the crystals kept pinned at the film-substrate interface up to the melting temperature.

Whereas, chapter 6 and chapter 7, focused on HMW fraction films study and showed that HMW films formed a less-ordered isotropic nodule structure, having the long chains that could interconnect the ordered domains and easy transport between domains. These films had chains that are longer than the domain size and linked the neighboring domains and reduced the number of grain boundaries. HMW molecules were shown to be kinetically prevented from forming optimal packing structures and thus the ultimate attainable mobility was limited.

Our DSC measurements for HMW fraction point out that the large melting enthalpy as well as the large intensity of powder X-ray diffraction peaks indicate that a large fraction of the chains are within ordered domains, rather large FWHM width of diffraction peaks and almost complete absence of higher order diffraction signals indicates that the order of the

chains in these domains are not very good. We put forward that our HMW samples consist of crystalline, partially-ordered and disordered phases. Where still disordered phase is dominating, where all the crystallites fall inside the disordered region and forming separately their crystalline domains having lack of contacts from their surrounding individual crystalline domains. Further, the temperature dependence of mobility measured with OFET show a moderate increase in mobility with temperature as far as the temperature is well below the melting transition. This is attributed to the hopping transport within the crystalline domains.

Correlation between the structural, thermal properties with the OFET performance gives strong evidence that the transport properties of layers prepared from both fractions of poly(3-hexylthiophene) is largely determined by the crystallinity of the samples. We presume that this correlation is rather universal and, in part, responsible for the strong dependence of the OFET mobilities for polymer OFETs on the preparation conditions.

Our experiments give evidence that for HMW the structural ordering can be much better at the temperature higher than RT. HMW P3HT with thickness larger than 200 nm both structural parameters are best at a temperature close to ~ 200 °C which is about 50 °C below T_m . Moreover, we can characterize this HT structure as a thermotropic phase appearing in addition to the phase found at RT. Once, one has transformed the system into equilibrium by a first heating cycle one can switch between both phases at any times. Our temperature dependent GID and GOD scans suggest a model where crystals existing at RT grown in height at the cost of their lateral width and by collecting chains out of the close vicinity to the crystals accompanied by nucleation of new small crystallites at the film-substrate interface. This development is supported by our results obtained from thin films. Here the vertical size of crystallites can grow up to a size not larger than the total film thickness. However, the in-plane behaviour is same as for thick films; the number of in-plane crystals at HT is larger but smaller in size than at RT. The later one is a hint for strong influence of the interface on structural order as suggested by our measurements at low molecular weight P3HT material.

For thick films we have found an expansion of out-of plane spacing at HT accompanied by compression of in-plane lattice parameter. These changes can be associated with a stretching of alkyl chains but a smaller π - π distance of thiophene rings. Same changes in π - π distance are observed for thin films also. While the out-of plane d-spacing does not expand much compared to thick films and the decrease of size of crystallites might be explained by the assumption that this spacing can only expand for crystals not pinned at the film-substrate interface.

For HMW fraction we have noticed that for thin films there is no interface region and films are behaving as a whole – while oppositely, thick films have shown the sharp interface after annealing and due to this reason big crystallites have grown at the interface level after the annealing (100) planes become exclusively parallel to substrate providing 2d network for charge transport. This is absent in ultrathin films.

In general, we have found the drop in mobility for temperatures above 120 °C and after this temperature; it depends on kinds of silanization the OFET behaviour can disappear completely. Moreover, the drop in mobility in HMW P3HT at HT is opposite to the expectation considering the decrease in π - π distance and improved structure ordering along surface normal direction mentioned above. Therefore the drop in mobility cannot be associated with the smaller in-plane spacing and the improved crystallinity of such HMW films. The only explanation of our finding is that the limiting factor for the OFET mobility is through the amorphous parts of the film, the hole transport along the chains interconnecting the crystals pinned at the film-substrate interface. Compared with LMW P3HT the mobility in HMW P3HT is high because the main chain in the order of average distance between crystallites as well as the length of the chain is higher than the size of crystallites. This interconnection becomes disturbed with increasing the temperature, due to the increased of chain mobility and second due to the collection of chains by the growing crystals. Assuming that the growth of crystals in polymer by chain folding it becomes understandable that the regions close to a crystal becomes cleared by stretched chains arranged parallel to the film-substrate interface. This “collection” effect found larger for thick films and gave hint about why thin films show a smaller drop in HT mobility compared to thicker one.

S.2. Future Work

Under the above framework we have studied the structural properties of π -conjugated polymers i.e. HMW and LMW fractions of P3HT by means of X-ray scattering techniques. As well as the charge carrier mobility and its correlation with the structure ordering at surface-interface level having different morphology at buried interface and at the air/film interface. Considering all the work done as a basic model for understanding and correlating the structural properties with charge carrier mobility of semicrystalline polymeric system, as well as considering the technological importance of HMW P3HT fraction compared to LMW fraction due to higher mobility, further work should be devoted to the detailed study of the P3HT HMW fraction in order to complete our understanding about the structural based charge trans-

port mechanism in HMW fraction of P3HT. Further, studies on the structure and morphologies of P3HT on different polymeric dielectric layers will also be important to carry out, as the performance of OFET is mainly determined at this interface. Factors limiting the performance of OFET due to non-optimized morphology at P3HT/modified SiO₂ interface than can be overcome.

Air stable organic semiconductor with high field-effect mobility and low intrinsic conductivity is needed for further development of OFET-based applications. The poor stability of such thiophene based materials at ambient atmosphere is also one of the concerning factors limiting the OFET applications. Our detailed structural study of P3HT can help chemists to develop such strong crystalline phase material, where the crystalline to amorphous ratio must be higher compared to as present. Our results will also put a light on the way to improve the mobility of such system by improving the buried interface structure, where the charge transport will be possible through mainly ordered crystalline regions. For that one has to modify the dielectric layer or perhaps come up with a better device model solution.

Determining the source of these charge traps at the buried interface level would be very valuable for designing new polymers with a low trap density and thus a higher mobility. The possible solution could be by reducing the imperfections present in the ordered regions, chemical defects in the molecules, impurities in the film, and the amorphous regions of the film. Our work gives a direct hint for how to improve such defects stated above; especially recrystallization mechanism and development of a suitable polymer dielectric will be a key factor to grow the molecules under control mechanism. Considering our work the analysis of next generation polymers with crystalline to amorphous ratio will be relatively straightforward from now onwards. At the same time key findings from the measured relationship between morphology and charge transport for these new polymers will be an aid for designing of even better polymers in the upcoming future.

Appendix

A. OFET Preparation

OFETs were prepared in bottom-gate top-contacts geometry (Fig. 1) on top of the n-doped Si substrate [1, 2]. Where the thermally-grown 300 nm thick SiO_2 serves as gate insulator. Before starting of sample preparation, the substrate surface was thoroughly cleaned involving numerous common organic solvents. The SiO_2 surface was then treated by one of the following three ways to allow for the investigation of the interface treatment effect. The sample 1) was used as it was (bare SiO_2 surface), or was passivated by a combined oxygen plasma treatment (at a power of 200 W for 5 minutes) and silanization by 2) spin-coating octadecyltrichlorosilane (OTS) at a speed of 2000 rpm from a 10^{-6} M solution in chloroform, 3) storing it in a saturated atmosphere of HMDS for 26 hours at 60 °C. Finally, a 100 nm thick interdigitating gold structure was evaporated, acting as a source and drain electrodes with a channel length of 0.1 mm and channel width of 148.5 μm .

OFET devices were prepared from organic semiconductors using spin casting technique to coat organic thin film layers with an average thickness of 10-200 nm. The organic semiconductors were dissolved in organic solvents and spun onto either the treated or untreated Si/ SiO_2 substrates. Then a 100 nm thick interdigitating Au structure, which serves as a source and drain electrodes, was evaporated on top of the polymer layer (Au purity is 99.99%, Umicore Co., Balzers, Liechtenstein). The channel length and total channel width were 100 μm and 14.85 μm , respectively.

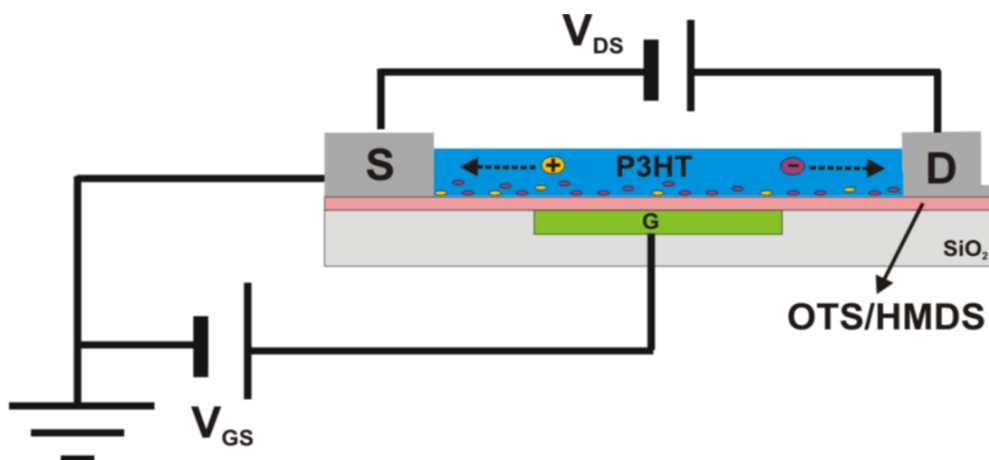


Figure 1 Scheme of electrical characterization setup bottom gate –top contact geometry.

B. Experimental Methods

B.1. Differential Scanning Calorimetry

Differential scanning calorimetry (DSC) measures the heating effects associated with phase transitions and chemical reactions as a function of temperature for organic materials upon thermal treatment (heating and cooling). In DSC measurements (Fig. 2) the difference in heat flow to the sample and a reference at the same temperature, is recorded as a function of temperature. The reference is an inert material such as Alumina, or just an empty Aluminium pan. The temperature of both the sample and reference are increased at a constant rate. Since the DSC is at constant pressure, heat flow is equivalent to enthalpy changes.

DSC measurements considering organic materials can provide the vital information about their phase transition for the melting of semicrystalline phase as well as glass transition temperature of an amorphous polymeric material.

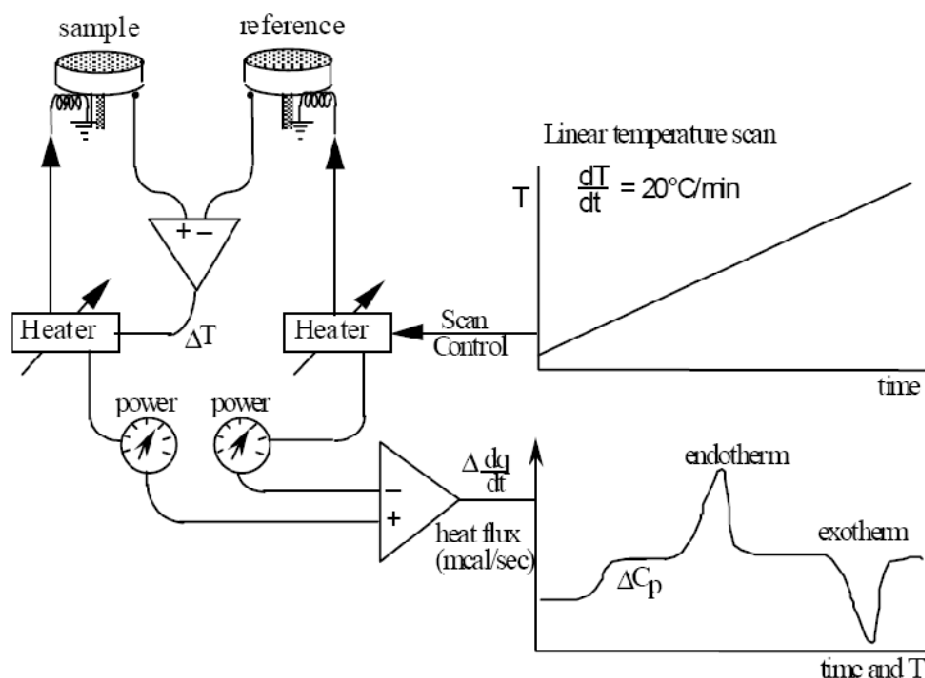


Figure 2 Schematic of a DSC. One should choose the linear temperature scan rate. The triangles are amplifiers that determine the difference in the two input signals. The sample heater power is adjusted to keep the sample and reference at the same temperature during the scan.

$$\left(\frac{dq}{dt}\right)_p = \frac{dH}{dt} \quad (\text{A})$$

Here $\frac{dH}{dt}$ is the heat flow measured in mcal sec^{-1} . The heat flow difference between the sample

and the reference is

$$\Delta \frac{dH}{dt} = \left(\frac{dH}{dt} \right)_{\text{sample}} - \left(\frac{dH}{dt} \right)_{\text{reference}} \quad (\text{B})$$

It can be either positive or negative. In an endothermic process, such as most phase transitions, heat is absorbed and, therefore, heat flow to the sample is higher than that of the reference. Hence $\Delta dH/dt$ is positive. In an exothermic process, such as crystallization, some cross-linking processes, oxidation reactions, and some decomposition reactions, the opposite is true and $\Delta dH/dt$ is negative. During the heating of a sample, for example, from room temperature to its decomposition temperature, peaks with positive or negative $\Delta dH/dt$ may be recorded for each peak corresponds to a heat effect associated with a specific process, such as crystallization or melting (Fig. 3).

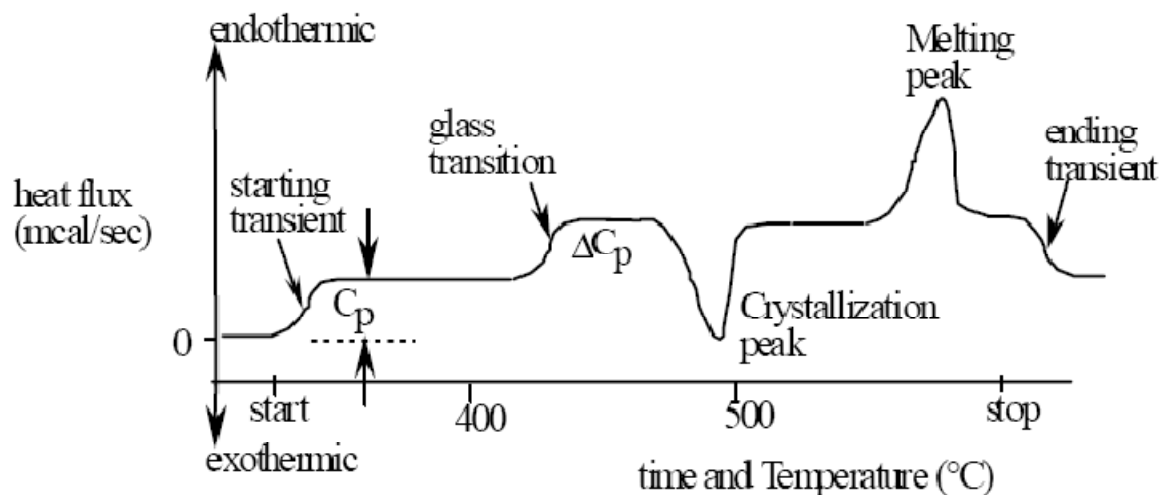


Figure 3 Typical DSC scan. The heat capacity of the sample is calculated from the shift in the baseline at the starting transient. Glass transitions cause a baseline shift. Crystallization is a typical exothermic process and melting is a typical endothermic process, $\Delta_{tr}H$ is calculated from the area under the peaks. Not all samples show all the features shown in this thermogram.

The question arises as to what kind of information is obtainable from a DSC curve. The first and most direct information is the temperature at which a certain process occurs, for example, the melting point of a polymer. The temperature at which a reaction, such as decomposition, may start is another important parameter. The peak temperature is associated with the temperature at which maximum reaction rate occurs. One of the main advantages for organic materials is that one can calculate the degree of crystallinity [2, 4].

The temperature at which the phase transformation occurs is of great importance in polymers, known as glass transition temperature, T_g . This is the temperature, at which amor-

phous (noncrystalline) polymers are converted from a brittle, glasslike form to a rubbery, flexible form. This is not a true phase transition but one that involves a change in the local degrees of freedom. Above the glass transition temperature certain segmental motions of the polymer are comparatively unhindered by the interaction with neighbouring chains. Below the glass transition temperature, such motions are hindered greatly, and the relaxation times associated with such hindered motions are usually long compared to the duration of the experiment. The operative definition of glass transition temperature is that, at this temperature, or within a few degrees, the specific heat, the coefficient of thermal expansion, the free volume, and the dielectric constant (in the case of a polar polymer) all change rapidly. Since the mechanical behaviour of polymers changes markedly at the glass transition temperature, it is an important characteristic of every polymer. In the DSC experiment, T_g is manifested by the drastic change in the base line, indicating a change in the heat capacity of the polymer (Fig. 4). No enthalpy is associated with such transition (for which reason it is also called a second order transition); therefore, the effect in a DSC curve is slight and is observable only if the instrument is sensitive enough. Direct information obtainable from DSC curves is the enthalpy associated with certain processes.

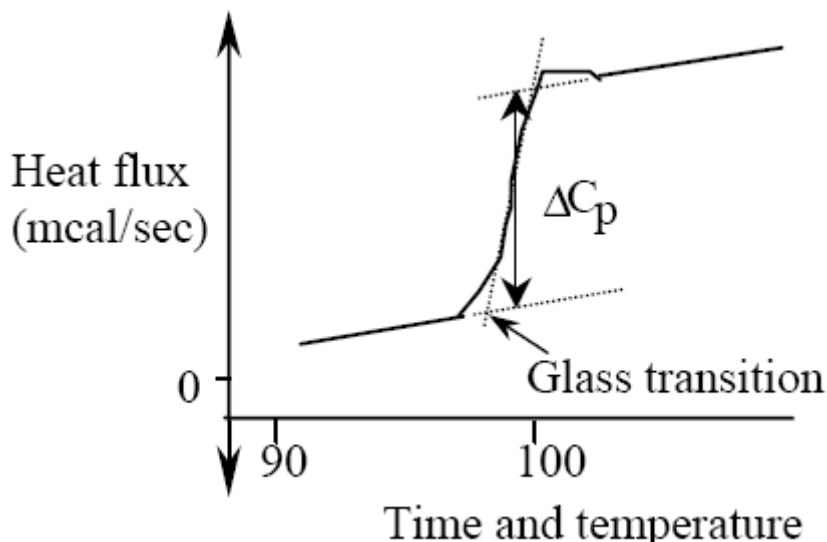


Figure 4 Glass transition. If there are sloping baselines before and after the glass transition, extrapolate the baselines forwards and backwards (as shown by dotted lines) and take the baseline shift when the transition is about 63% complete (as shown by arrows).

B.2. Atomic Force Microscopy (AFM)

The Atomic Force Microscope was developed [5] to overcome the basic drawback with STM - that it can only image conducting or semiconducting surfaces. The AFM, how-

ever, has the advantage of imaging almost any type of surface, including polymers, ceramics, composites, glass, and biological samples.

Binnig, Quate, and Gerber invented [5] the Atomic Force Microscope in 1985. Their original AFM consisted of a diamond shard attached to a strip of gold foil. The diamond tip contacted the surface directly, with the interatomic van der Waals forces providing the interaction mechanism. Detection of the cantilever's vertical movement was done with a second tip - an STM placed above the cantilever.

Contact Mode

The first and foremost mode of operation, contact mode is widely in use. As the tip is raster-scanned across the surface, it is deflected as it moves over the surface corrugation. In constant force mode, the tip is constantly adjusted to maintain a constant deflection, therefore constant height above the surface. It is this adjustment that is displayed as data. However, the ability to track the surface in this manner is limited by the feedback circuit.

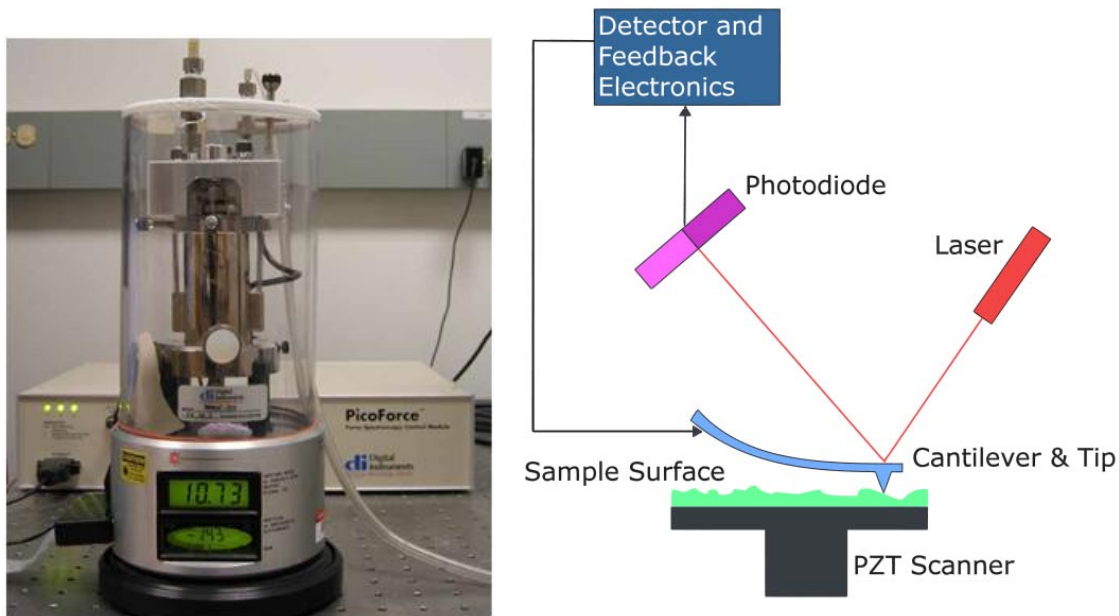


Figure 5 Modern atomic force microscope (AFM) (left) and the schematic working principle of the AFM (right).

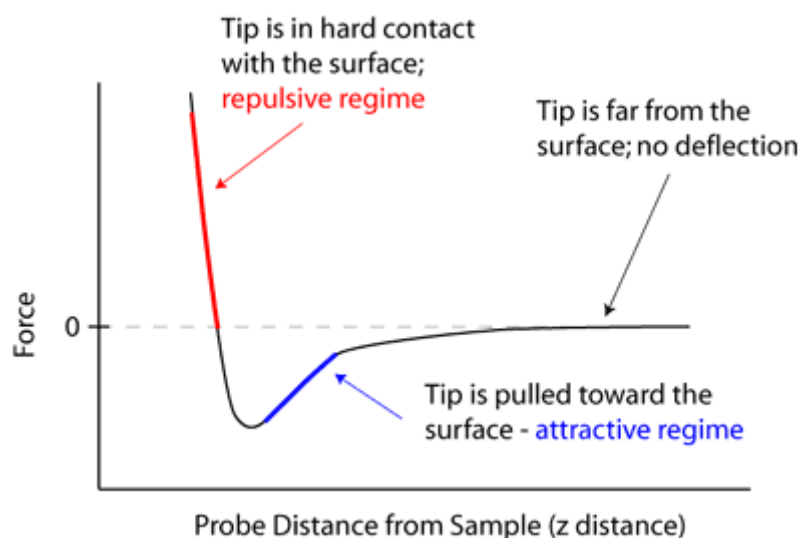


Figure 6 Intermolecular force curve that describes the interaction between two uncharged molecules or atoms.

Sometimes the tip is allowed to scan without this adjustment, and one can measure only the deflection. This is useful for small, high-speed atomic resolution scans, and is known as variable-deflection mode. Because the tip is in hard contact with the surface, the stiffness of the lever needs to be less so that the effective spring constant holding atoms together, which is on the order of 1 - 10 nN/nm. Most contact mode levers have a spring constant of < 1N/m.

Noncontact Mode

Noncontact mode belongs to a family of AC modes, which refers to the use of an oscillating cantilever. A stiff cantilever is oscillated in the attractive regime, meaning that the tip is quite close to the sample, but not touching it (hence, “noncontact”). The forces between the tip and sample are quite low, of the order of pN (10^{-12} N). The detection scheme is based on measuring changes to the resonant frequency or amplitude of the cantilever.

Tapping Mode AFM

Commonly referred to as “tapping mode”, it is also referred to as intermittent-contact or the more general term Dynamic Force Mode (DFM). A stiff cantilever is oscillated closer to the sample than in noncontact mode. Part of the oscillation extends into the repulsive regime, so the tip intermittently touches or “taps” the surface. Very stiff cantilevers are typically used, as tips can get “stuck” in the water contamination layer. The advantage of tapping mode is that the surface is improved lateral resolution on soft samples. Lateral forces, such as drag,

common in contact mode, are virtually eliminated. For poorly adsorbed specimens on a substrate surface the advantage is clearly seen.

B.3. Transmission Electron Microscopy

The Transmission Electron Microscope (TEM) gives the chance to users to resolve the internal structure of materials, independent of their physical origin (biological/ non-biological).

Sample preparation for TEM measurements is crucial and all the samples must be prepared in a form which allows the electrons to transmit through the sample, similar to conventional optical microscopy. Since the wavelength of electrons is much shorter than that of light, the resolution attainable in TEM is many orders of magnitude greater than that from a light microscope. As an outcome, TEMs can reveal the finest details of internal structure - in some cases as small as individual atoms.

Under the TEM measurements, we recorded the Bright field (BF), this is an imaging mode where the direct unscattered beam is allowed to reach the image plane. Whereas the Dark field (DF), this is the opposite imaging mode, where only scattered radiation is allowed to form the image. Dark field images normally have much higher contrast than bright field images, but are much weaker in intensity. Scattered electrons may be collected for the DF image by displacing the objective aperture, but usually it is better to tilt the incident beam.

The diffraction pattern is displayed on the fluorescent screen. Dark field imaging is tricky because the low intensity needs long exposures and low magnifications. Dark field images from disordered or amorphous materials are particularly low in intensity due to their random orientations the electrons are scattered in all directions and only few of them collected by the objective aperture. DF in the TEM is very important for study of crystalline materials. Then the image can be formed from one spot in the diffraction pattern. Bright regions in the image show only the ordered areas with the correct orientation so crystallite dimensions can be measured and their orientation determined.

Organic materials, generally have low atomic number (z) due to the mainly presence of carbon, hydrogen, nitrogen, all these are weak scatterer and giving poor contrast in the TEM. They are also highly beam-sensitive; radiation damage causes destruction of crystallites ordering, chain scission or cross-linking, mass loss and dimensional changes. Increasing the accelerating voltage and cooling the sample can help the situations, to increase the contrast.

C. References

- [1] Zen, A.; Pflaum, J.; Hirschmann, S.; Zhuang, W.; Jaiser, F.; Asawapirom, U.; Rabe, J. P.; Scherf, U.; Neher, D.; *Adv. Funct. Mater.*, 14, 757-764, 2004.
- [2] Zen, A.; Saphiannikova, M.; Neher, D.; Grenzer, J.; Grigorian, S.; Pietsch, U.; Asawapirom, U.; Janietz, S.; Scherf, U.; Lieberwirth, I., Wegner, G.; *Macromolecules*, 39, 2162-2171, 2006.
- [3] Zen, Achmad, Phd thesis, University Potsdam, Potsdam, germany, 2006.
- [4] Malik, S.; Nandi, A. K. *J. Polym. Sci. Part B: Polym. Phys.*, 40, 2073, 2002.

Acknowledgement

I have had the good fortune to be able to work with and participate in experiments at different synchrotron facilities around the Europe. The initiation of this X-ray source has had a tremendous impact on many aspects of the natural sciences and has been important to the collection of many of the data, which are presented in this thesis. Diffraction experiments especially on polymer surfaces and interfaces, where scattering cross section is so weak, measurements of the critical scattering which is a precursor to many phase transitions are types of experiments where the use of a synchrotron X-ray source is truly favourable.

I would like to express my appreciation and gratitude to all the people who have helped me during my doctorate studies in the University Siegen, Siegen, Germany. First and foremost I would like to thank Prof. Dr. Ullrich Pietsch for his constant support, tireless and continuous guidance, ideas and his patience, throughout the whole course of this project, since without his invaluable direction and support, this work would not have finished in time. At the same time I also express my sincere appreciation and thank to Dr. Souren Grigorian for his help and support during the whole course.

At the same time i would like to thank our collaborator and the suppliers for not only providing the raw excellent Poly(3-hexylthiophene) organic semiconductors as well as the thin P3HT films to kick-off the task at the early stage of this project. Ex-members and current-members from the group of Prof. Dieter Neher at the University Potsdam, Potsdam, Germany in particular: Dr. Achmad Zen and Patrick Pingel. Prof. Ullrich Scherf at the University of Wuppertal and in particular: Dr. Michael Förster.

I would also like to thank to all ex-member and current-members of Solid State Physics group for great scientific team spirit and personal friendship, in particular Dr. Tobias Panzner, Tushar Sant for the fruitful discussions and Dr. Özgül Kurtulus for her support during the long exhausting beamtime at various synchrotron sources. For the thesis proofing, I am thankful to T. S. Shabi.

For the financial support, I gratefully acknowledge the German Science Foundation (Deutsche Forschungsgemeinschaft) under program of emphasis 1121: Organic Field-Effect Transistors. In addition, I would also acknowledge BASF- the chemical company for their financial support during the last stage of the studies.

I would also like to thank Delta (Dortmund, Germany), ESRF (Grenoble, France), and Hasylab (Hamburg, Germany) synchrotron source beamlines for providing the beamtime and the respective staff scientists for the experimental support.

Acknowledgement

Last but not least, I would like to express my gratitude to all of my family and friends in India for all the support and encouragement I've received over the last 3 years. I give my warmest thanks to my sister and her family and my loving brothers, who always supported me during this period of time. Finally, I devote this thesis to my late beloved parents (Late Shri B. P. Joshi and Late Smt. Leela Joshi). Their constant encouragement, support and blessings always accomplish me.

Siddharth Joshi
Siegen, Germany
December, 2008.

Curriculum Vitae



Siddharth Joshi was born on 2nd July 1976 in Lucknow, Uttar Pradesh, India. He had received the National Talent search scholarship from Central Government of India and went to Vidya Bhawan Senior Higher Secondary School, Udaipur, Rajasthan and completed junior- and senior- high schools from it.

He started studying Physics at the Bachelor level at Lucknow University, Lucknow, India and completed his Bachelor of Science in 1998.

His interest in Physics earliest motivated him towards teaching the high school and Intermediate student around 2 years. Later for his further higher studies he went to Singapore after receiving the research scholarship from National University of Singapore, Singapore from July 2002. During his master work he worked under mentorship of Prof. Wolfgang Knoll, Prof. Karou Tamada and Prof. Andrew Wee. Where, he investigated the nano-pattern formation of di-block copolymers thin films induced by hydrophilic surfaces and their characterization by means of modern surface science tools as XPS, AFM as well as with SPR.

From April 2005, he started his PhD studies under the supervision of Prof. Dr. Ullrich Pietsch at the University of Potsdam, Potsdam, Germany. Where, later he moved to University Siegen, Siegen, Germany along with Prof. Pietsch. Here, he investigated the structure characterization and surface-interface modification of Poly(3-hexylthiophene). The recrystallization mechanism to improve the better surface and buried interface properties and their correlation with corresponding charge carrier mobility. The results are presented on this Ph.D. thesis and number of international publications as well as number of international conferences.

Talks, List of Publications, Conferences

Talks –

1. **S. Joshi**, S. Grigorian, U. Pietsch, P. Pingel, A. Zen, D. Neher: Structure and crystallinity study in thin films of poly(3-hexylthiophene) OFET layers, Abschlusskolloquium zum DFG Schwerpunktprogramm ‘‘Organische Feldeffekttransistoren’’, Physikzentrum Bad Honnef, Bad Honnef, June 2007.

2. **S. Joshi**, S. Grigorian, U. Pietsch, P. Pingel, A. Zen, D. Neher: Temperature dependent structure and crystallinity study in thin films of poly(3-hexylthiophene) OFET layers, “7th Autumn school on X-ray scattering from surfaces and thin layers”, Smolenice, Slovakia, October 2007.
3. **S. Joshi**, S. Grigorian, U. Pietsch, P. Pingel, A. Zen, D. Neher: Temperature dependent structure and crystallinity studies of high molecular weight P3HTs. Wuppertal colloquium, Wuppertal, Germany, 29th November, 2007.
4. **S. Joshi**, S. Grigorian, U. Pietsch, P. Pingel, A. Zen, D. Neher, M. Forster, U. Scherf: Temperature dependent X-ray diffraction studies of low and high molecular weight P3HTs, DPG Conference, Berlin, Germany, Feb 2008.
5. **S. Joshi**, S. Grigorian, T. Panzner, U. Pietsch, P. Pingel, D. Neher, M. Forster, U. Scherf: Temperature dependent X-ray diffraction studies of high molecular weight Poly(3-hexylthiophene) P3HTs fraction, 11th European Conference on Organised Films, Potsdam, Germany, July 2008.

Posters –

1. **S. Joshi**, S. Grigorian, U. Pietsch, A. Zen, D. Neher: “X-ray studies of structure and crystallinity of poly(3-hexylthiophene)”, DPG conference, Regensburg, Germany, 26th-30st March 2007.
2. **S. Joshi**, S. Grigorian, U. Pietsch, P. Pingel, A. Zen, D. Neher: X-ray studies of low and high molecular weight poly(3-hexylthiophene) thin films, ‘Charge Transport in Organic Materials: From Single Molecules to Devices’, DPG Physics school, Physikzentrum Bad Honnef, Bad Honnef, 23rd September – 28 September 2007.

Publications –

1. **S. Joshi**, S. Grigorian, U. Pietsch, X-ray Structural and Crystallinity studies of low and high molecular weight Poly(3-hexylthiophene), *Physica status solidi (a)* 205, 488-496, **2008**.

2. **S. Joshi**, S. Grigorian, U. Pietsch, P. Pingel, A. Zen, D. Neher, Thickness dependence of the crystalline structure and electron mobility in thin films of low molecular weight Poly(3-hexylthiophene), *Macromolecules*, 41, 6800-6808, 2008.
3. **S. Joshi**, S. Grigorian, U. Pietsch, P. Pingel, A. Zen, D. Neher, Michael Forster, Ulrich Scherf, Bi-modal temperature behaviour of structure and mobility at High molecular weight P3HT thin films, Manuscript in Preparation, 2008.

Book Chapter

1. **S. Joshi**, S. Grigorian, U. Pietsch, “Physical and Chemical Aspects of Organic electronics – From fundamentals to functioning devices”, Feb 2009, Wiley-VCH, Berlin.

Eidesstattliche Erklärung

Ich versichere hiermit an Eides statt, dass ich die vorliegende Arbeit ohne fremde Hilfe und ohne Benutzung anderer als der angegebenen Hilfsmittel angefertigt habe. Alle Ausführungen, die wortlich oder singemäß aus fremden Quellen übernommen wurden sind als solche gekennzeichnet. Die Arbeit wurde bisher in gleicher oder ähnlicher Form noch keiner anderen Jury vorgelegt und wird noch nicht kommerziell genutzt.

Ich bin bewusst dass eine falsche Erklärung den Ausschluss aus dem verfahren zur Folge haben wird.

Siegen, 12.11.2008

Ort / Datum

Unterschrift